Title (160 characters including spaces): Lymphatic muscle cells are the innate pacemaker cells regulating mouse lymphatic collecting vessel contractions

Authors: S.D. Zawieja[1], G.A. Pea[1], S.E. Broyhill[1], K.H. Bromert, C. E. Norton[1], H. J. Kim[1], M. Li[1], J.A. Castorena-Gonzalez [2], B.T. Drumm[3], and M.J. Davis[1]

[1]Dept. of Medical Pharmacology & Physiology, University of Missouri, Columbia, Missouri;
[2]Dept. of Pharmacology, Tulane University, New Orleans, Louisiana
[3]Smooth Muscle Research Centre, Dundalk Institute of Technology, Dundalk, Co. Louth, A91 K584, Ireland.

Correspondence:
Michael J. Davis, PhD
Department of Medical Pharmacology and Physiology
One Hospital Drive
MA415 Medical Sciences Building
University of Missouri
Columbia, MO 65212
Tel: 573-884-5181
Fax: 573-884-4276
davismj@health.missouri.edu

Co-Correspondence:
Scott Zawieja PhD
Department of Medical Pharmacology and Physiology
One Hospital Drive
MA415 Medical Sciences Building
University of Missouri
Columbia, MO 65212
Tel: 573-882-8069
Fax: 573-884-4276
zawiejas@health.missouri.edu

Running title: Lymphatic Muscle as Innate Pacemaker Cells

Impact: The presence and functionality of proposed pacemaker cells in collecting lymphatic vessels was tested with various mouse Cre models to drive expression of a recombination reporter ROSA26mT/mG, a genetically encoded Ca^{2+} sensor GCaMP6f, or the optogenetic tool channel-rhodopsin2. Lymphatic $CD34^{+}$ adventitial cells co-express $PDGFRA^{+}$ while $cKit^{+}$ cells are mast cells; and neither cell type demonstrated pacemaking functionality. *Myh11CreER^{T2}*

identified lymphatic muscle cells which exhibited pacemaker behaviors such as pressure-dependent calcium events during diastole and propagated contraction induced by optical stimulation of channel-rhodopsin2.

Abbreviations: Ano1, Anoctamin 1; ChR2, channel rhodopsin; cLV, collecting lymphatic vessel; IALV, Inguinal Axillary Lymphatic Collecting Vessel; ICC, Interstitial Cell of Cajal; ICLC, Interstitial Cell of Cajal Like Cell; LEC, Lymphatic Endothelial Cell; LMC, Lymphatic Muscle Cell; STDs, Spontaneous transient depolarizations; STMs, Spatio-Temporal Maps

Keywords: Lymphatic collecting vessel, lymphatic muscle cell, pacemaking, interstitial cells of Cajal like cells, mesenchymal stem cells

Abstract

Collecting lymphatic vessels (cLVs) exhibit spontaneous contractions with a pressure-dependent frequency, but the identity of the lymphatic pacemaker cell is still debated. By analogy to pacemakers in the GI and lower urinary tracts, proposed cLV pacemaker cells include interstitial cells of Cajal like cells (ICLC), pericytes, as well as the lymphatic muscle (LMCs) cells themselves. Here we tested the extent to which these cell types are invested into the mouse cLV wall and if any cell type exhibited morphological and functional processes characteristic of pacemaker cells: a contiguous network; spontaneous Ca^{2+} transients; and depolarization-induced propagated contractions. We employed inducible Cre (iCre) mouse models routinely used to target these specific cell populations including: c-kitCreER^{T2} to target ICLC; *PdgfrβCreER*^{T2} to target pericytes; *PdgfrαCreER*^{TM} to target CD34^{+} adventitial fibroblast-like cells or ICLC; and *Myh11CreER*^{T2} to target LMCs. These specific inducible Cre lines were crossed to the fluorescent reporter ROSA26mT/mG, the genetically encoded Ca^{2+} sensor GCaMP6f, and the light-activated cation channel rhodopsin2 (ChR2). c-KitCreER^{T2} labeled both a sparse population of LECs and round adventitial cells that responded to the mast cell activator compound 48-80. *PdgfrβCreER*^{T2} drove recombination in both adventitial cells and LMCs, limiting its power to discriminate a pericyte specific population. *PdgfrαCreER*^{TM} labeled a large population of interconnected, oak leaf-shaped cells primarily along the adventitial surface of the vessel. Titrated induction of the smooth muscle-specific *Myh11CreER*^{T2} revealed a LMC population with heterogeneous morphology. Only LMCs consistently, but heterogeneously, displayed spontaneous Ca^{2+} events during the diastolic period of the contraction cycle, and whose frequency was modulated in a pressure-dependent manner. Optogenetic depolarization through the expression of ChR2 by *Myh11CreER*^{T2}, but not *PdgfrαCreER*^{TM} or c-KitCreER^{T2}, resulted in a propagated contraction. These findings support the conclusion that LMCs, or a subset of LMCs, are responsible for mouse cLV pacemaking.

Introduction

The spontaneous contractions of collecting lymphatic vessels (cLV) are an integral component to fluid and macromolecule homeostasis as they provide the force to transport fluid from the interstitium back to the blood circulation (Scallan et al., 2016). In humans, spontaneous contractile activity is estimated to account for 2/3 of lymph transport (Engeset et

89 al., 1977) and this function is significantly compromised in patients suffering from lymphedema,
90 whose cLVs typically display weak and irregular or entirely absent contractile activity
91 (Olszewski, 2002). *Ex vivo* studies, in which the intraluminal pressure can be precisely
92 controlled, have refined our understanding of the pressure-dependent regulation of
93 contraction frequency (Benoit et al., 1989; Gashev et al., 2004), with some mouse cLVs
94 displaying a 10-fold increase in contraction frequency over a 10 cmH_2O pressure gradient
95 (Scallan and Davis, 2013; Zawieja et al., 2018). The observation that cLVs, often cannulated at
96 various lengths for *ex vivo* preparations, retain a consistently tunable contraction frequency
97 points to the presence of a pacemaker cell(s) innate to the structure of the cLV wall and with a
98 seemingly ubiquitous presence along the length of the vessel (Zawieja et al., 1993; Castorena-
99 Gonzalez et al., 2018b).
100 Investigations into the cLV pacemaker identity have focused largely on cells termed
101 interstitial cells of Cajal like cells (ICLC; or telocytes) (McCloskey et al., 2002; Briggs Boedtkjer et
102 al., 2013), as they display some morphological and cell marker expression profiles similar to the
103 interstitial cells of Cajal (ICC), which are bona fide pacemakers in the gastrointestinal (GI) tract.
104 ICC are classically identified by either methylene blue staining and expression of cKit, and
105 coordinate GI smooth muscle contraction (Maeda et al., 1992; Ward et al., 1994; Ordog et al.,
106 1999). ICC also express the canonical Ca^{2+} activated chloride channel Anoctamin 1 (Ano1)
107 (Gomez-Pinilla et al., 2009), which is required for the electrical slow wave initiation and
108 formation that subsequently activates an action potential in GI smooth muscle (Hwang et al.,
109 2009; Zhu et al., 2009; Singh et al., 2014). Previous reports in sheep mesenteric lymphatic
110 vessels identified a population of $cKit^+$, $vimentin^+$, ICLC in the vessel wall between the
111 endothelial and LMC layer and running along the axis of the vessel (McCloskey et al., 2002).
112 Investigations in the human thoracic duct also identified a significant population of ICLC in close
113 proximity to the lymphatic muscle cells (LMCs) evident by methylene blue staining,
114 immunostaining for CD34, vimentin, and cKit, as well as the gold standard of electron
115 microscopy (Briggs Boedtkjer et al., 2013). However, neither study could determine if these
116 cells had functional electrical communication with the LMCs or demonstrate either a
117 membrane electrical clock or internal Ca^{2+} clock to drive the rhythmic lymphatic vessel
118 contractions observed *ex vivo*. LMCs share a functional similarity to ICC in that they also display
119 a Ca^{2+} activated chloride current (Van Helden, 1993; Toland et al., 2000; Mohanakumar et al.,
120 2018), mediated by Ano1 (Zawieja et al., 2019), that regulates pacemaking by modulating the
121 slope of diastolic depolarization. Spontaneous transient depolarizations, presumably Ano1
122 dependent, were recorded in mesenteric cLVs from guinea pigs (Van Helden, 1993; von der
123 Weid et al., 2008) providing a mechanism for membrane potential instability. Furthermore,
124 computational models have proposed LMC sarcoplasmic reticulum (SR) Ca^{2+} release as the
125 oscillator mechanism driving pacemaking (Imtiaz et al., 2007). SR Ca^{2+} release has also been
126 implicated in pericyte regulation of arterioles (Hashitani et al., 2015; van Helden and Imtiaz,
127 2019), in microvascular vasomotion (Boedtkjer et al., 2008; Aalkjaer et al., 2011; van Helden
128 and Imtiaz, 2019), and in the contraction waves of atypical muscle cells of the lower urinary
129 tract (Grainger et al., 2022).
130
131 Presently, no investigations have clearly identified the cellular identity of possible
132 pacemaker cells within the cLVs of the mouse. Murine cLVs exhibit contractile parameters and

133 conduction speed similar to those of human vessels (Castorena-Gonzalez et al., 2018b) and
134 their simplified architecture, compared to larger mammals, in combination with the genetic
135 tools developed for the mouse model, allowed us to test for a fundamental pacemaker cell in
136 the cLV. In this study we utilized multiple genetic mouse models, immunofluorescence imaging,
137 Ca^{2+} imaging, and optogenetic light-activated depolarization to both visualize and test the
138 functional aspects of putative pacemaker cells. We did not observe a significant or contiguous
139 $cKit^{+}$ cell population along the vessels. *PdgfrαCreER*^{TM} was able to consistently delineate a
140 significant population of interconnected adventitial cells that were also $CD34^{+}$. However, an
141 absence of Ca^{2+} events in phase with the contractile activity and an inability to consistently
142 elicit a contraction upon photo-stimulated depolarization provides functional evidence against
143 a role for either $PDGFR\alpha^{+}$ or $cKit^{+}$ adventitial cells as the pacemaker cell. In contrast, $MYH11^{+}$
144 LMCs exhibited diastolic Ca^{2+} events that, while asynchronous, were dynamically modulated by
145 pressure and could elicit a propagated contraction after optogenetic stimulation of LMCs
146 expressing ChR2.
147
148 **Results**
149 **Methylene Blue Staining Reveals adventitial Cells in Murine cLVs**
150 Methylene blue staining was used to identify an ICLC population in the human lymphatic
151 thoracic duct (Briggs Boedtkjer et al., 2013). In our isolated and cleaned IALVs ,methylene blue
152 stained a significant number of cells along the length of the vessel. The methylene $blue^{+}$ cells
153 had variable density along the length of the vessel and stained cells exhibited different patterns
154 of morphology and location (Figure 1A-C). A significant portion of the stained cells resembled
155 lymphatic vessel-associated macrophages with an elongated spindle shape, while other cells
156 were smaller and circular (Figure 1D-F). Methylene blue also appeared to stain mast cells as
157 there were large ovoid cells on the adventitia of the vessel with intracellular granules. In
158 addition, methylene blue stained a minor population of cells that exhibited long and thin axon-
159 like extensions which appeared to have a slight helical orientation, with a small central body
160 and nucleus (Figure 1C). None of these cell populations were aligned with the longitudinal axis
161 of the vessel that would permit efficient coupling or regulation across the circumferential LMCs
162 required for coordinated propagation along the length of the vessel.
163
164 **Immunofluorescence Imaging of IALVs stained for ICLC, LEC, and LMC Markers**
165 We first stained IALVs for the putative telocyte/ICLC markers cKit, CD34, and the intermediate
166 filament vimentin, which have been previously described in human and sheep lymphatic tissues
167 (McCloskey et al., 2002; Briggs Boedtkjer et al., 2013). Lymphatic muscle cells also express the
168 intermediate filament desmin (McCloskey et al., 2002). IALVs stained for cKit (Figure 2B) had
169 robust signal in large ovoid cells characteristic of mast cells, confirmed to contain a nucleus via
170 DAPI staining (Figure 2A), that were located in the outer part of the adventitia. Similarly, cKit
171 stained populations of elongated cells as well as circular cells with variable density throughout
172 the IALV wall, similar to methylene $blue^{+}$ cell populations (Figure 2B, J). Staining for CD34
173 revealed a striking population of cells that were seemingly contiguous along the length of the
174 vessel. These $CD34^{+}$ cells generally had multiple lobular processes and a "oak leaf" like
175 appearance, characteristic of fibroblasts, while some contained short, thin dendrite-like
176 extensions (Figure 2C, G, K). $CD34^{+}$ cells were negative for desmin (Figure 2H), which stained

177 the circumferential LMCs (Figure 2F; note that the largely non-circumferential cell organization
178 in this region is typical for a lymphatic endothelial valve site). Furthermore, the CD34$^+$ cells and
179 cKit$^+$ stained separate populations (Figure 2D, L). Vimentin stained lymphatic endothelial cells
180 (LECs) which exhibited a horizontal cobblestone morphology in parallel with the vessel axis
181 (Figure 2E, I), while also co-labeling the majority of the CD34$^+$ cells (Figure 2H) and cKit$^+$ cells
182 (Figure 2L). Videos of the half vessel z-stacks are provided (Supplemental Movies 1-3 for Figure
183 2D, H, and L respectively).
184 Of the cells stained in Figure 2, the CD34$^+$ population was intriguing due to its high
185 density and seemingly consistent presence through the length of the IALV, which potentially
186 would be conducive to effective regulation of LMC excitability. In addition to CD34 and
187 vimentin, PDGFRα expression is also commonly ascribed to both telocytes (Vannucchi et al.,
188 2013; Xiao et al., 2013; Zhou et al., 2015) as well as fibroblasts (Kimura et al., 2021; Clayton et
189 al., 2022). We performed immunofluorescence imaging for PGDFRα counterstained with CD34
190 and markers for LMCs, LECs, or myeloid-derived cells. As noted with desmin staining in Figure 2,
191 CD34$^+$ cells (Figure 3A) did not co-label LMCs (Figure 3D) that were smooth muscle actin$^+$
192 (Figure 3B) and calponin$^+$ (Figure 3C). However, nearly all CD34$^+$ (Figure 3E) cells were also
193 PDGFRα$^+$ (Figure 3G, H) but not SMA+ (Figure 3G, H). Staining to outline LECs with CD31
194 (PECAM, Figure 3I) revealed the expected rectangular cobblestone morphology that was
195 distinct from the PDGFRα labeled cells (Figure 3J, L). Calponin specifically stained LMCs (Figure
196 3K) but not PDGFRα+ cells (Figure 3L). To determine if the CD34$^+$PDGFRα$^+$ cells had
197 hematopoietic or mononuclear phagocytic origin, we stained IALVs from Macgreen mice (Csfr1-
198 EGFP) with CD45 and PDGFRα. Anti-GFP (Figure 3M) labeled the cLV myeloid cells (Macgreen),
199 which consists of predominantly macrophages and dendritic cells, that were co-stained by
200 CD45$^+$ (Figure 3O, P). CD45$^+$ but GFP- negative circular cells were also observed and are likely T-
201 Cells, B-cells, or mast cells. As expected, the PDGFRα$^+$ cell population (Figure 3N) was not CD45$^+$
202 (Figure 3P). Lastly, we stained for PDGFRα, CD34, and PDGFRβ, a commonly used pericyte
203 marker (Figure 3 Q-T). As above, CD34 and PDGFRα were highly colocalized (Figure 3Q, R, T),
204 and many of the CD34$^+$ and PDGFRα$^+$ cells were also PDGFRβ$^+$ (Figure 3T). PDGFRβ also stained
205 some circumferential LMCs, albeit with a weaker signal than the adventitial cells (Figure 3U).
206 During the imaging of mouse IALVs for these markers, we also observed that the lymphatic
207 secondary endothelial valves were populated by elongated cells that stretched the length of the
208 valve leaflet and were positive for CD34, PDGFRα, and PDGFRβ, with varying intensities, and
209 found within both leaflets of the valve (Figure 3V,W) as determined from max projections of a
210 z-stack encompassing only the "z slices" within the lumen of the IALV. These cells had long, thin
211 extensions that were branched along with apparent dendrite extensions with a morphology
212 that closely resembled those described of pericytes or telocytes (Popescu and Faussone-
213 Pellegrini, 2010) (Figure 3V,W). PDGFRα$^+$ or CD34$^+$ cells with this morphology were only
214 observed in the valve leaflets and thus seemed insufficient to regulate pacemaking as normal
215 contractions are observed in cLVs without secondary valves (not shown). The z-stacks
216 demonstrating these valve-located "telocyte" shaped cells (Figure 3V,W) are provided as
217 Supplemental Movies 4 and 5.
218 The vast majority of the PDGFRα$^+$ cells were located in the adventitial layer Figure 4A-D,
219 which varied between 2-3 PDGFRα$^+$ cells thick (Figure 4E) for this particular mouse lymphatic
220 collecting vessel. Under this layer, we observed only a single layer of largely circumferential

221 LMCs stained by MYH11 (Figure 4B) sitting atop a single layer of CD31$^+$ LECs (Figure 4A). We
222 also observed occasional PDGFRα$^+$ cells or their extensions located in the sub-endothelial space
223 (Figure 4 E', E") positioned between the LECs and the LMCs.
224 We next determined the degree of colocalization between the CD34 and PDGFRα signal
225 given the significant overlap. Colocalization analysis of PDGFRα (Figure 5A) and CD34 (Figure
226 5B) and their colocalization (Figure 5C) was determined with the FIJI BIOP-JACoP tool. The
227 Pearson's coefficient was 0.83 (Figure 5 D) and Mander's coefficient of overlap 0.80 was for the
228 PDGFRα$^+$ signal and 0.87 for the CD34 signal (Figure 5E). This high degree of colocalization CD34
229 and PDGFRα signal informed our use of the commercially available *PdgfrαCreER^{TM}* mouse model
230 to target these cells.
231
232 **Use of iCre-Mediated Recombination of Rosa26mT/mG to delineate and characterize specific**
233 **IALV cell types**
234 After confirming the presence of Vimentin$^+$, cKit$^+$, and CD34$^+$ PDGFRα$^+$ positive cells within the
235 mouse IALV, we sought to further investigate these cell populations by using constitutive and
236 inducible Cre recombinase expressing mouse lines. IALVs from the constitutively active
237 *PdgfrαCre*-ROSA26mTmG and *Ng2Cre*-ROSA26mTmG mice had GFP fluorescence in the
238 majority of LMCs as well as in the fibroblast-shaped cells found within the IALV wall (Figure 6
239 A,B). While informative of expression of the LMC progenitor cells, neither constitutive Cre
240 would be useful in delineating cell types. In contrast to the constitutively active *PdgfrαCre*, the
241 tamoxifen inducible *PdgfrαCre^{TM}* line drove significant recombination in only the fibroblast-
242 shaped cells previously stained with CD34 and PDGFRα but not LMCs or LECs (Figure 6C).
243 *PdgfrβCreER^{T2}*, commonly used to label pericytes, drove recombination in both a minor
244 population of the LMCs and the fibroblast-shaped cells. *cKitCreER^{T2}*, which capably drives
245 recombination in the ICC of the GI (Baker et al., 2016), drove recombination only in a small
246 population of irregularly-spaced large ovoid cells on the surface of the IALV (Figure 6E), largely
247 corresponding with mast cell labeling, although recombination in 1 or 2 LECs could occasionally
248 be detected (not shown). Finally, *Myh11CreER^{T2}* drove recombination in nearly all LMCs which
249 were largely circumferentially oriented with dendrite-like, cell-cell contacts visible between
250 them and without significant GFP fluorescence in either LECs or the fibroblast-shaped CD34$^+$
251 PDGFRα$^+$ cell population (Figure 6F). Additionally, some LMCs maintained the bipolar shape but
252 had multiple extensions forming a "Y" shape in which an adjacent LMC typically filled the inner
253 void. A very minor population of recombined cells in the *Myh11CreER^{T2}*-ROSA26mTmG IALVs
254 were smaller and irregularly patterned with multiple fine axon-like projections or highly-
255 dendritic ruffled edges (Figure 6F).
256 To complement the morphological and cell density findings obtained with confocal
257 microscopy, we digested IALVs from the iCre-ROSA26mTmG lines, and the *Prox1-eGFP* line as a
258 control, into single cell suspensions and sorted the respective GFP$^+$ populations (Figure 6G-J) for
259 RT-PCR profiling (Figure 6K). We first focused on determining the molecular fidelity of the
260 sorted cells based on the gene promoters used to drive each "iCre" model to discern cellular
261 overlap. In agreement with the confocal images, sorted GFP$^+$ cells from *PdgfrβCreER^{T2}*-
262 ROSA26mT/mG IALVs expressed PDGFRβ but also MYH11 and PDGFRα. In contrast, GFP-sorted
263 cells from *PdgfrαCreER^{TM}* IALVs expressed PDGFRα and PDGFRβ, but with no detectable
264 expression of MYH11. Conversely, GFP$^+$ cells from sorted *Myh11CreER^{T2}*-ROSA26mTmG IALVs

265 had high expression for MYH11, as well as PDGFRβ, but did not express PDGFRα. IALVs from
266 *cKitCreER*^{T2}-ROSA26mTmG mice were not pursued for FACS due to the exceptionally sparse
267 recombination along the IALV.
268 We further profiled each population of sorted cells with RT-PCR for other common
269 markers for endothelial cells, muscle cells, and pericytes. Similar to the Prox1 results (Figure
270 6K), endothelial nitric oxide synthase (eNOS) expression was observed only in the *Prox1-eGFP*
271 sorted cells, which also expressed vimentin and MCAM and had weak but detectable signal for
272 CD34 (Figure 7A). *Myh11CreER*^{T2} sorted cells showed expression of smooth muscle actin
273 (Acta2), the alpha subunit of the L-type voltage gated Ca^{2+} channel Cav1.2, desmin, MCAM, and
274 vimentin (Figure 7B). In addition to the genes expressed under *Myh11CreER*^{T2} recombination,
275 Cdh5, CD34, and Cspg4 (Ng2) were detected in cells sorted in *PdgfrβCreER*^{T2} IALVs (Figure 7C).
276 As expected, the GFP^{+} cells sorted from *PdgfrαCreER*^{TM} IALVs expressed mRNA for CD34, Cspg4,
277 and vimentin, but not desmin, smooth muscle actin, nor the pericyte marker MCAM (Figure
278 7D). The alpha subunit of the voltage gated Ca^{2+} channel was positive in cells sorted from both
279 PDGFRα, PDGFRβ,and *Myh11CreER*^{T2} IALVs, but was also observed in the *PdgfrαCreER*^{TM} IALVs
280 without any evidence that MYH11 expressing muscle cells contaminated the latter. These
281 findings confirmed the separate cell populations achieved with *PdgfrαCre*^{TM} and *Myh11CreER*^{T2}
282 mediated recombination, at least as it pertains to ROSA26mTmG. We followed up the
283 identification of Cav1.2 expression in the *PdgfrαCreER*^{TM} sorted cell population by assessing the
284 expression of other genes involved in either pacemaking (Ano1) or electrical conduction (Cx45)
285 of IALVs (Figure 7E). Intriguingly, expression of both Ano1 and Cx45 was observed in the
286 *PdgfrαCreER*^{TM} sorted cells, which were further confirmed to lack either endothelial or
287 hematopoietic contamination as we did not detect expression of the endothelial marker CD31
288 or the hematopoietic marker CD45.
289
290 **Inducible Deletion of Either Cav1.2, Ano1, and Cx45 with *PdgfrαCreER*^{TM} Did Not Affect cLV**
291 **Pacemaking**
292 The expression of the genes critically involved in cLV function—Cav1.2, Ano1, and
293 Cx45—n the *PdgfrαCreER*^{TM}-ROSA26mTmG purified cells prompted us to generate
294 *PdgfrαCreER*^{TM}-Ano1fl/fl, *PdgfrαCreER*^{TM}-Cx45fl/fl, and *PdgfrαCreER*^{TM}-Cav1.2fl/fl mice for
295 functional testing. We isolated popliteal cLVs and tested their pacemaker and contractile
296 activity in response to physiological pressures over the range 0.5-10 cmH_2O, under normal
297 conditions. However, we did not detect any significant difference in pacemaking nor contractile
298 function of popliteal cLVs studied from *PdgfrαCreER*^{TM}-Ano1fl/fl (Figure 8A-F) or
299 *PdgfrαCreER*^{TM}-Cx45fl/fl (Figure9A-F), compared to their respective Ano1fl/f and Cx45fl/fl
300 controls. *PdgfrαCreER*^{TM}-Cav1.2fl/fl mice had no statistically significant differences in
301 normalized contraction amplitude (Figure 10A), contraction frequency (Figure 10C), fractional
302 pump flow (Figure 10D), end diastolic diameter (Figure 10E). However, we noted a mild but
303 statistically significant increase in ejection fraction at the lowest pressure, 0.5 cmH_2O. Vessels
304 isolated from *PdgfrαCreER*^{TM}-Cav1.2fl/fl mice also had a statistically significant increase in
305 vessel tone (Figure 10F) noted at the 2-way ANOVA level although we did not resolve
306 significance at any specific pressure with this sample size. Nonetheless, despite the presence of
307 transcript for these critical genes, *PdgfrαCreER*^{TM} mediated deletion failed to recapitulate

308 previous reports of contractile defects using the *Myh11CreER*^{T2} line (Castorena-Gonzalez et al.,
309 2018b; Zawieja et al., 2019; To et al., 2020; Davis et al., 2022).
310
311 **Potential Role for PDGFRα^{+} Adventitial Fibroblasts As Pool of Progenitor Cells**
312 Despite the lack of cLV pacemaking deficits in the *PdgfrαCreER*^{TM} genetic knockout lines, we
313 were curious to discern further insight into the role or function of the PDGFRα^{+} CD34^{+} cells
314 which comprise a significant portion of the lymphatic cLV wall. The *PdgfrαCreER*^{TM} recombined
315 cells exhibited expression of Krüppel-like factor 4 (Klf4), stem cell antigen 1 (Sca1, also referred
316 to as Ly6a), Gli1, CD29, CD105, and CD44 (Figure 11A, B). To again validate that this signature
317 was unique to the *PdgfrαCreER*^{TM} recombined cells, we performed RT-PCR on FACS from Prox1-
318 eGFP, *Myh11CreER*^{T2}-ROSA26mTmG, and *PdgfrαCreER*^{TM}-ROSA26mTmG IALVs. Recombined
319 (GFP^{+}) cells from *Myh11CreER*^{T2}-ROSA26mTmG had weak expression of Klf4 and Gli1 and were
320 negative for Sca1, CD34, and PDGFRα (Figure 11C). Similarly, LECs sorted from *Prox1-eGFP* IALVs
321 were positive for Klf4, weak for Sca1, and positive for CD34 but negative for GLi1 and PDGFRα
322 Gli1. In contrast, *PdgfrαCreER*^{TM}- ROSA26mTmG recombined cells were positive for all markers
323 as were the unrecombined population (tdTomato^{+}) cells in the *Myh11CreER*^{T2}- ROSA26mTmG
324 IALVs (Figure 11D). We performed immunofluorescence staining for one of these multipotent
325 markers, Sca1 (Figure 11E, I) while counter staining for LMCs, with SMA or MYH11 (Figure 11F,
326 J), and the adventitial cells with PDGFRα (Figure 11G, K). The morphology and staining pattern
327 of Sca1 overlapped significantly with PDGFRα staining and not the LMC staining (Figure 11H, L,
328 Supplemental Movie 6).
329
330 **Optogenetic Stimulation of iCre-driven Channel Rhodopsin 2 to Induce Test Light-Stimulated**
331 **Depolarization Induced Lymphatic Contraction**
332 We next used optogenetic methods to test whether the cell populations recombined by either
333 *cKitCreER*^{T2}, *PdgfrαCreER*^{TM}, or *Myh11CreER*^{T2} could elicit a coordinated contraction. The ChR2-
334 tdTomato construct appeared more sensitive to recombination than ROSA26mTmG, in some
335 cases resulting in LMC expression of ChR2-tdTomato in *PdgfrαCreER*^{TM} and *CKitCreER*^{T2} vessels.
336 Care was taken to image the vessel for tdTomato (Figure 12A,C,E) prior to stimulation at their
337 respective sites under brightfield conditions for diameter tracking (Figure 12B,D,F) to ensure
338 fidelity of the cell types and morphologies observed in Figure 3. As with ROSA26mTmG,
339 *CKitCreER*^{T2} drove the ChR2-tdTomato expression primarily in large ovoid cells found on the
340 adventitia of the vessel. Photo-stimulation of these cells did not initiate coordinated
341 contractions (Figure 12G-J,S). Similarly, photo-stimulation of ChR2-tdTomato expressing cells
342 driven by *PdgfrαCreER*^{TM} failed to initiate a coordinated contraction (Figure 12K-N, T). In
343 contrast, photo-stimulation of LMCs, using *Myh11CreER*T2 to express Chr2-tdTomato, resulted
344 in a propagated contraction in the popliteal vessel (Figure 12O-R, U). In total, only 3.25% of
345 photo-stimulations of *cKitCreER*^{T2}-ChR2-TdTomato and 3.03% of photo-stimulations of
346 *PdgfrαCreER*^{TM}-ChR2-tdTomato were associated with a contraction, while 88.5% of photo-
347 stimulations of *Myh11CreER*^{T2}-ChR2-tdTomato photo-stimulations induced contractions (Figure
348 12V). The low percentages of optogenetic firing of contractions observed in *PdgfrαCreER*^{TM}-
349 ChR2-tdTomato and *cKitCreER*^{T2}-ChR2-TdTomato vessels are likely due to the happenstance of
350 spontaneous contractions occurring during the time and proximity of optogenetic stimulation.
351 As mast cells are not ascribed any tissue specific pacemaking behavior, the similar percentages

352 observed between these two groups is suggestive of coincidence. Brightfield videos of the
353 photo-stimulation and representative traces for *cKitCreER*^{T2}-ChR2-TdTomato, *PdgfrαCreER*^{TM}-
354 ChR2-tdTomato, *Myh11CreER*^{T2}-ChR2-tdTomato are provided in Supplemental Movies 7-9.
355
356 **Confocal Ca^{2+} Imaging of GCaMP6f Expression Driven by *cKitCreER*^{T2}, *PdgfrαCreER*^{TM}, and**
357 ***Myh11CreER*^{T2} Over the Lymphatic Contraction Cycle**
358 We imaged IALVs from *cKitCreER*^{T2}-GCaMp6f mice, which primarily resulted in expression of
359 GCaMp6f in the large ovoid cells in the adventitia (Figure 13A), although we occasionally
360 observed GCaMP6f expression in both LEC and LMCs (Figure 13A) as depicted in the maximum
361 projection of the acquisition period (Supplemental Movie 10) and the spatio-temporal maps
362 (STMS). The aberrant expressions of GCaMP6f in cells that demonstrated the typical
363 cobblestone morphology of LECs or the circumferential LMCs that exhibited Ca^{2+} flashes and
364 diastolic Ca^{2+} transients (Figure 13D,E green arrows) prior to contraction (Figure 13D,E) were
365 not included in the *cKitCreER*^{T2}-GCaMp6f analysis. Of the 39 *cKitCreER*^{T2}-GCaMp6f cells
366 analyzed, only 1 *cKitCreER*^{T2}-GCaMP6f cell exhibited a spontaneous Ca^{2+} transient during the
367 recording period (Figure 13B,C Cell 7). However, the Ca^{2+} transient in that cell did not align
368 temporally with the "Ca^{2+} flash" of the LMC with incidental GCaMp6f expression (Figure
369 13C,D). Despite the lack of Ca^{2+} transients under the baseline conditions throughout the IALV
370 contraction cycle, many *cKitCreER*^{T2}-GCaMP6f cells exhibited a robust and prolonged Ca^{2+} event
371 in response to stimulation with the mast cell activator compound 48-80 (Figure 13F, G, H).
372 Notably, the Ca^{2+} events in the ovoid cells elicited by administration of compound 48-80 did not
373 acutely alter the LMC Ca^{2+} activity (Figure 13I,J). Similar to *cKitCreER*^{T2}-GCaMp6f, the majority of
374 PDFRαCreER^{TM}-GCaMP6f expressing cells also largely lacked Ca^{2+} transients and also resulted in
375 incidental LMC GCaMP6f expression (Figure 14B, Supplemental Movie 11). Some cells exhibited
376 high basal Ca^{2+} (Figure 14A,D) sustained throughout the recording, but oscillations were not
377 observed (Figure 14B,C). In contrast, spurious GCaMP6f expression in a circumferentially
378 oriented LMC displayed Ca^{2+} flashes associated with contraction (Figure 14B,C). Of the 21
379 PDGFRα-GCaMP6f cells assessed, only 3 exhibited Ca^{2+} transients which were singular events
380 with limited spatial spread within the 20 sec imaging period (Figure 14E,F). The lack of either
381 global or consistent Ca^{2+} transients within either *cKitCreER*^{T2}-GCaMP6f or *PdgfrαCreER*^{TM}-
382 GCaMP6f IALVs was in stark contrast to Ca^{2+} imaging of *Myh11CreER*^{T2}-GCaMP6f IALVs.
383 *Myh11CreER*^{T2} drove GCaMp6f expression in the circumferential LMCs (Figure 15A), which had
384 global and nearly synchronous Ca^{2+} flashes in 100% of the analyzed cells (Figure 15B, C).
385 Additionally, non-synchronous stochastic and localized Ca^{2+} transients during diastole were
386 commonly observed in the LMCs (Figure 15D, E, Supplemental Movie 12). Many LMCs exhibited
387 Ca^{2+} transients during each diastolic period while other LMCs displayed few Ca^{2+} transients or
388 lacked diastolic Ca^{2+} transients during the recording periods (Figure 15B). In aggregate, of the
389 39 *cKitCreER*^{T2}-GCAMP6f cells only 1 displayed a Ca^{2+} transient during recording, 3 of the 21
390 *PdgfrαCreER*^{TM}-GCaMP6f cells, while 20 of 43 LMCs displayed at least one diastolic transient
391 apart from 43 of 43 LMCs with global flashes.
392
393 **Pressure Dependency of Subcellular Ca^{2+} Transients in LMCs**
394 We next sought to test whether diastolic Ca^{2+} transients were pressure-dependent, given that
395 cLVs exhibit pressure dependent chronotropy (Zawieja et al., 2019). GCaMP6f expressing LMCs

396 were studied in the presence of nifedipine, which blocks the calcium flashes but not local
397 calcium transients at intraluminal pressures of 0.5 -5 cmH_2O (Figure 16A). As intra-luminal
398 pressure was increased, there was a marked increase in the occurrence of Ca^{2+} transients
399 (Figure 16B, Supplemental Movies 13-15). By converting raw Ca^{2+} transients for particle
400 analysis (PTCLs), we generated activity maps of Ca^{2+} PTCL activity (Figure 16C) and determined
401 PTCL area (Figure 16D) and frequency at each pressure (Figure 16E). The maps show that as
402 pressure increased, the activity of PTCLs across the vessel also increased (as evident by the
403 increase in PTCL area activation). Across 11 experiments, the area of the field of view activated
404 by PTCLs/frame increased from 73.2 ± 17.7 mm^2/frame at 0.5 cmH_20 to 108.6 ± 20.5
405 mm^2/frame at 2 cm H_20 and further enhanced to 139.2 ± 26.9 mm^2/frame at 5 cm H_2O (Figure
406 16F). The number of PTCLs per frame also increased with pressure, from 2.9 ± 0.4 at 0.5 cmH_20
407 to 4.1 ± 0.5 and 5.2 ± 0.6 PTCL/frame at 2 and 5 cmH_20 respectively (Figure 16E).
408
409 **Discussion**
410 The identification of the cellular origin and signaling mechanisms underlying cLV pacemaking
411 will open up novel targets for pharmacological intervention in treating lymphedema and the
412 associated lymphatic contractile dysfunction. In this study we tested proposed pacemaker cell
413 types based on 3 parameters: 1) that the pacemaker cells are located along the entire length of
414 the cLV, to accommodate spontaneous contractions and coordinated electrical conduction
415 despite progressive shortening of cLVs; 2) that depolarization of the pacemaker cell can drive a
416 coordinated and propagated contraction of the vessel; and 3) that the presence of Ca^{2+}
417 transients precedes contraction, as commonly observed in other pacemaker cell types. We used
418 confocal microscopy and a combination of immunofluorescence and fluorescent reporters
419 under the control of various inducible Cres to identify various non-muscle cells that express the
420 markers CD34 and PDGFRα. From our initial fluorescence imaging studies, a role for intrinsic
421 pacemaking by LMCs (Van Helden, 1993; von der Weid et al., 2008), or by a novel population of
422 lymphatic ICLC (McCloskey et al., 2002; Briggs Boedtkjer et al., 2013), also referred to as
423 telocytes, were further examined. However, the PDGFRα cell population had minimal Ca^{2+}
424 activity and optogenetic depolarization of these cells failed to drive a spontaneous contraction.
425 In contrast, photo-stimulation of LMCs expressing ChR2 elicited robust propagating
426 contractions similar to spontaneous activity. Furthermore, Ca^{2+} imaging in LMCs revealed
427 diastolic Ca^{2+} transients in diastole that increased in frequency and spatial spread as pressure
428 was elevated. Our results, in addition to the recent findings using targeted deletion of Ano1
429 (Zawieja et al., 2019), Cx45 (Castorena-Gonzalez et al., 2018b), or Cav1.2 (To et al., 2020; Davis
430 et al., 2022) in lymphatic muscle support the model of LMCs as the intrinsic pacemaker as has
431 been previously proposed (Van Helden, 1993; Van Helden et al., 1996; Van Helden and Zhao,
432 2000).
433
434 **Pacemaking in Smooth Muscle**
435 In many smooth muscle organs, regulation of a coordinated contraction is a complex and
436 multicellular phenomenon. Multiple cell types integrate physical and biological information into
437 electrical activity to be transmitted to the force-producing smooth muscle cells, sometimes
438 across great distances relative to cell size, to regulate calcium influx by voltage dependent
439 calcium channels required for contraction. The intestine is one such documented tissue in

440 which cKit$^+$ ICCs and interstitial PDGFRα$^+$ cells form an electrical syncytium to regulate intestinal
441 motility (Sanders et al., 1999; Sanders et al., 2014). The pacemaking function of intestinal ICCs
442 relies heavily on Ano1, a calcium activated chloride channel, which is required for slow wave
443 activity in the ICCs. Both cKit and Ano1 can be used as a marker for ICCs in the intestine (Hwang
444 et al., 2009; Cobine et al., 2017; Malysz et al., 2017), cKit$^+$ and vimentin$^+$ ICLCs have been
445 observed in sheep lymphatic vessels (McCloskey et al., 2002), yet these cell populations do not
446 form gap junctions with the smooth muscle to form electrical connections (Briggs Boedtkjer et
447 al., 2013) as occurs in the intestinal ICCs. Our cKit staining of mouse IALVs revealed a sparse
448 population of large ovoid cells previously classified as mast cells (Chatterjee and Gashev, 2012;
449 Zawieja et al., 2019). Their identity as mast cells was further supported by the sustained global
450 Ca^{2+} event after stimulation with the mast cell degranulating agent compound 48-80. However,
451 both vimentin and CD34 showed robust staining throughout the mouse lymphatic vessel wall.
452 Vimentin stained LECs, as well as non-muscle stellate shaped cells, with many co-expressing
453 CD34, and other smaller circular cells some of which were cKit$^+$ as well and some whose
454 morphology was similar to that of the macrophage staining profile of the GFP$^+$ cells in IALVs
455 from MacGreen mice , as well as previous reports of macrophage staining in cLVs (Bridenbaugh
456 et al., 2013; Chakraborty et al., 2015; Zawieja et al., 2016). While vimentin$^+$ cells had a nuclear
457 and perinuclear staining profile, CD34 demarcated the cell membrane and was useful for
458 assessing the morphology of these cells. Of particular interest, the vimentin$^+$CD34$^+$ cells densely
459 populated the length of the mouse IALV, with a majority displaying a flattened stellate
460 morphology characterized by the classic rounded oak leaf appearance, although some displayed
461 fine dendrite extensions. Contrasting with the previous findings in the human thoracic duct
462 (Briggs Boedtkjer et al., 2013), we did not observe a significant population of CD34$^+$ cells with a
463 bipolar morphology oriented axially along the vessel. However, z-stack reconstructions of
464 sections of the mouse IALV that included the secondary valves revealed interstitial
465 CD34$^+$PDGFRα$^+$ cells that resembled the bipolar cells with multiple axon-like extensions
466 throughout the endothelial leaflets similar to the interstitial cells that were reported in the
467 lymphovenous valves (Geng et al., 2016). While these cells have not been frequently described
468 in the peripheral cLV valves, we observed these cells in each of the valve regions we imaged in
469 addition to labeling them with other Cre drivers, including NG2-Cre;ROSA26mTmG and
470 *Pdgfrβ*CreER*T2 ROSA26mTmG (data not shown). Whether these cells play a role in the
471 extracellular matrix deposition or lymphatic valve integrity is unknown, but their role as a
472 critical pacemaker can be excluded as vessel segments without valves display normal
473 contractile behavior. Instead, the majority of the CD34$^+$PDGFRα$^+$ cells were found in the
474 adventitia with 2-3 layers overtop the LMCs and were consistently observed in high density
475 along the IALV. Some CD34$^+$PDGFRα$^+$ cells or their extensions were present between the
476 lymphatic endothelial and muscle layers as had been previously reported with electron
477 microscopy of human lymphatic vessels (Briggs Boedtkjer et al., 2013).
478
479 **PDGFRα$^+$CD34$^+$ Cells are Not Involved in cLV Pacemaking Under Physiological Conditions**
480 CD34 and PDGFRα are described as telocyte markers, although PDGFRα routinely labels
481 fibroblasts and specific interstitial cells in the GI tract involved in purinergic neurotransmission
482 (Kurahashi et al., 2011; Kurahashi et al., 2013; Clayton et al., 2022), and CD34 expression has
483 been observed in multipotent cell populations of various origins (Sidney et al., 2014). Of course,

484 neither telocytes, hematopoietic or mesenchymal stem cells, nor fibroblasts, are monolithic in
485 their expression patterns within and much less across tissues, and single cell RNA sequencing
486 has provided immense detail about the sub clusters and spectrums within which these cells
487 exist as well as their plasticity. Nonetheless, we attempted to gain further insight into the
488 characteristics of CD34$^+$PDGFRα$^+$ cells. CD34$^+$PDGFRα$^+$ cells were consistently negative for the
489 majority of smooth muscle markers such as desmin, calponin, smooth muscle actin, smooth
490 muscle myosin heavy chain, and the pericyte marker MCAM. However, PDGFRβ expression was
491 noted in sorted *PdgfrαCreER*$^{TM-}$ROSA26mTmG cells, in addition to the staining of LMCs, and
492 PDGFRβ protein expression was confirmed with variable immunofluorescence staining amongst
493 the PDGFRα stained cells as well as LMCs. The *PdgfrβCreER*T2-ROSA26mTmG mice had only
494 modest recombination in both the LMC and PDGFRα$^+$ cell population, but potentially
495 highlighted a myofibroblast-like cell subpopulation, cells that might lie on the spectrum of
496 differentiation from lymphatic muscle and PDGFRα$^+$ cells, or perhaps a cell with pacemaker
497 activity as PDGFRβ is widely used as a pericyte marker and some pericytes display pacemaker
498 activity (Hashitani et al., 2015). Adding to this intrigue, the *PdgfrαCreER*^{TM} sorted cells
499 expressed transcripts for Cav1.2, the voltage-gated L-type Ca^{2+} channel critical for lymphatic
500 contractions (Zawieja et al., 2018; To et al., 2020); Ano1, the ion channel underlying pressure
501 dependent chronotropy (Mohanakumar et al., 2018; Zawieja et al., 2019); and Cx45, the
502 primary connexin mediating electrical conduction in mouse lymphatic collecting vessels
503 (Castorena-Gonzalez et al., 2018b; Hald et al., 2018). The presence of those gene transcripts
504 does not appear to be due to muscle cell contamination or incidental recombination in LMCs as
505 we did not detect LMC markers in the RT-PCR profiling of the sorted PDGFRα$^+$ cells nor were
506 GFP-expressing cells with an LMC morphology observed in imaging of *PdgfrαCreER*^{TM}-
507 ROSA26mTmG vessels. Critically, however, deletion of Cav1.2, Cx45, or Ano1 through
508 *PdgfrαCreER*^{TM} mediated recombination neither recapitulated the previous phenotypes
509 achieved with *Myh11CreER*^{T2} (Castorena-Gonzalez et al., 2018b; Zawieja et al., 2019; To et al.,
510 2020; Davis et al., 2022) nor significantly affected pacemaking in mouse popliteal cLVs. This is in
511 stark contrast to the complete lack of contractions observed in *Myh11CreER*T2-Cav1.2 vessels
512 (To et al., 2020) or the vessels from vascular muscle specific Itga8CreERT2-Cav1.2fl/fl mice
513 (Davis et al., 2022; Warthi et al., 2022),and the significant loss in pressure-induced chronotropic
514 modulation of pacemaker function in IALVs with *Myh11CreER*^{T2}-mediated deletion of Ano1 that
515 we have previously reported (Zawieja et al., 2019) . While a sub-population of CD34$^+$PDGFRα$^+$
516 cells may share expression of critical pacemaker genes identified in the LMCs, they do not
517 appear to be involved in cLV pacemaking or contractile function under physiological states.
518 Instead, CD34$^+$PDGFRα$^+$ cells co-stained significantly with Sca1$^+$, suggesting they may be primed
519 to act as resident multipotent cells (Song et al., 2020; Kimura et al., 2021). To this point, the
520 *PdgfrαCreER*^{TM} FACS purified cells also expressed markers associated with "stemness" such as
521 CD34, Klf4, Gli1, CD29, CD105, CD44, and vimentin, in addition to Sca1, and it is likely that the
522 *PdgfrαCreER*^{TM} population includes various distinct subpopulations (Jolly et al., 2022) expressing
523 these markers. These cells may play a role in rebuilding the lymphatic collecting vessel
524 vasculature following lymph node resection and further studies are required to assess their
525 functional multipotency.
526
527 **SR Ca^{2+} Cycling in Pacemaking**

528 The use of the mouse model, in addition to the simplicity of the vessel architecture, provided
529 the use of genetic tools that previously had been instrumental in identifying the cKit^{+} ICC as the
530 pacemaker cells of the GI tract (Ward et al., 1994; Huizinga et al., 1995; Torihashi et al., 1995).
531 Through the use of the respective *PdgfrαCreER^{TM}* and *Myh11CreER^{T2}* models, were able to
532 specifically image Ca^{2+} in each cell type in pressurized, contracting vessels. Pacemaking
533 initiating cells have an inherently unstable membrane potential, oftentimes utilizing the
534 oscillatory nature of Ca^{2+} release from the sarcoendoplasmic reticulum coupled to Ca^{2+} sensitive
535 electrogenic exchangers and ion channels to drive depolarization (Van Helden, 1993; Hashitani
536 et al., 2015; Baker et al., 2021b; Sanders et al., 2022). One such example is the pacemaker ICC
537 in the gastric corpus which exhibit abundant Ca^{2+} transients that couple to Ano1-mediated
538 chloride currents in both the intervening period between slow waves as well as the plateau
539 phase of the slow wave (Baker et al., 2021a), although such activity is not characteristic of all
540 pacemaker ICC types. The identification of a Ca^{2+} activated chloride current in LMCs (Van
541 Helden, 1993; Toland et al., 2000) and its correspondence with subcellular Ca^{2+} transients (Van
542 Helden, 1993; Ferrusi et al., 2004; von der Weid et al., 2008) led Van Helden to postulate that
543 LMCs had an intrinsic pacemaking capability (Van Helden, 1993; Van Helden et al., 1996). We
544 have previously reported that mouse LMCs in pressurized vessels routinely display subcellular
545 Ca^{2+} release events that reflect the kinetics and characteristics of Ca^{2+} puffs and waves in
546 addition to the coordinated global Ca^{2+} flash associated with influx during an action potential
547 (Castorena-Gonzalez et al., 2018b; Zawieja et al., 2018; Zawieja et al., 2019). Here we confirmed
548 the consistent presence of subcellular Ca^{2+} transients only in LMCs with GCaMP6f driven by
549 *Myh11CreER^{T2}* but not in the cells with GCaMP6f driven by *PdgfrαCreER^{TM}*. Critically, we also
550 demonstrated that the Ca^{2+} transients increased in both frequency and spatial spread as
551 pressure was elevated in the vessel, as would be expected to account for the pressure
552 dependent chronotropy observed in lymphatic collecting vessels. This underscores the recent
553 finding that the genetic deletion of Ano1 in the LMCs dramatically reduced contraction
554 frequency and abolished pressure-dependent chronotropy in those vessels (Zawieja et al.,
555 2019). This phenotype was largely replicated with a similar reduction in frequency and loss of
556 pressure dependent chronotropy in our recent study utilizing *Myh11CreER^{T2}* to drive deletion of
557 IP3R1 from LMCs (In revision, JGP 2023) and fits with the central role of IP3R and subcellular
558 Ca^{2+} release as critical components of intrinsic LMC pacemaking (Van Helden et al., 1996; von
559 der Weid et al., 2008). The lack of Ca^{2+} transients in PDGFRα^{+} cells across any stage of the
560 lymphatic contraction cycle diminishes any expected role for this cell type to perform as the
561 pacemaker for the mouse IALV. The contribution of specific LMC SR Ca^{2+} signals to lymphatic
562 pacemaking remains to be fully addressed.
563
564 A pacemaker cell would be expected to be electrically coupled to the LMC layer to permit the
565 nearly synchronous conduction velocity of the contraction wave (Zawieja et al., 1993;
566 Castorena-Gonzalez et al., 2018b; Hald et al., 2018) and to transmit their own depolarization
567 into their coupled LMCs to activate the voltage dependent Ca^{2+} channels that are responsible
568 for lymphatic muscle action potentials. Connexins are the molecular constituents of gap
569 junctions and, as stated above, we detected Cx45 expression in the *PdgfrαCreER^{TM}* sorted cells.
570 However, we did not detect any impairment in pacemaking, nor were contraction conduction
571 speed deficits or multiple pacemakers noted in the *PdgfrαCreER^{TM}* -Cx45fl/fl popliteal cLVs, in

572 contrast to the development of multiple pacemaker sites and the lack of entrainment that were
573 reported previously in *Myh11CreER*^{T2}-Cx45fl/fl cLVs (Castorena-Gonzalez et al., 2018b).
574 Admittedly, we did not perform an exhaustive assessment of the connexin expression profile of
575 the CD34$^+$PDGFRα$^+$ cells, and Cx45 may not be the dominant connexin expressed in the
576 CD34$^+$PDGFRα$^+$ cells, or heterotypic connexons could exist (Koval et al., 2014). However,
577 electron microscopy studies of the putative ICLC in the human thoracic duct did not detect any
578 gap junctions, although peg-and-socket connections were observed (Briggs Boedtkjer et al.,
579 2013). We utilized optogenetics to enforce channel rhodopsin expression in both the
580 *PdgfrαCreER*^{TM} and *Myh11CreER*^{T2} mouse models to directly depolarize the specific cell
581 populations in an attempt to drive a contraction. Local photo-stimulation of the PDGFRα cells
582 failed to initiate contraction while the stimulation of *Myh11CreER*^{T2} recombined cells resulted
583 in contractions that were indistinguishable from the spontaneously occurring contractions.
584 These results give functional credence to the lack of hetero-cellular coupling that was
585 previously reported . Just as critically, they also highlight the regenerative nature of the
586 lymphatic muscle action potential as local depolarization was sufficient to drive a coordinated
587 contraction along the vessel and that a single or few LMCs reaching threshold for AP initiation
588 are sufficient to drive the conducted activity observed at the tissue level.
589
590 **Conclusions**
591 Our present findings lend further support to the hypothesis that the LMCs are intrinsic
592 pacemakers (van Helden et al., 2006; Mitsui and Hashitani, 2020) and do not require an ICC-like
593 network to drive propagated contractions. These findings also underscore the significance of
594 lymphatic muscle Ca^{2+} handling as the driver of lymphatic pacemaking, which can be
595 compromised in disease states leading to impaired lymphatic contractile activity (Stolarz et al.,
596 2019; Lee et al., 2020; Van et al., 2021). Further studies delineating the specific SR Ca^{2+} release
597 and influx pathways, and the contributions of Ca^{2+} sensitive ion channels need to be identified
598 to develop sophisticated in silico models and identify potential therapeutic targets to rescue
599 lymphatic pacemaking in lymphedema patients (Olszewski, 2002, 2008).
600
601 **Limitations**
602 One assumption underlying our conclusions is that there is a conserved fundamental
603 pacemaking pathway in lymphatic muscle pacemaking across species, specifically pertaining to
604 the capability of lymphatic muscle to maintain pacemaking and coordination despite changes in
605 tissue complexity. Lymphatic collecting vessels in mice have similar pressure-dependent
606 chronotropy and contraction conduction velocity as recorded in human vessels (Castorena-
607 Gonzalez et al., 2018b). These similarities exist despite the fact that mouse lymphatic collecting
608 vessels are encircled by a single layer of lymphatic muscle while larger species have multiple
609 layers of LMCs in the wall. It is possible that vessels with multiple layers of LMCs need a
610 network of ICLC to coordinate their activity. The simplicity in the makeup of the mouse cLV and
611 the use of cell targeting Cre models provide great control over our experimental variables, but
612 other cell types may provide coordination of LMC pacemaking in other species where the
613 lymphatic cLV walls are larger with multiple muscle layers.
614

615 Our data demonstrates that limited staining of a few cell markers alone is insufficient to identify
616 discrete cell populations in the murine cLVs. Additionally, mRNA expression does not equal
617 protein translation nor guarantee specific function as we did not detect endothelial CD34 with
618 immunofluorescence despite detecting transcript; additionally, *PdgfrαCreER*^{TM} mediated
619 deletion of Ano1, Cx45, or Cav1.2 had no effect on cLV pacemaking. Hence, further
620 experimentation is also required to fully characterize expression of multipotent cell markers
621 and function of CD34^{+}PDGFRα^{+}Sca1^{+} cells invested within the murine cLVs, although this was
622 beyond the scope of this study assessing pacemaker identity. Tangentially, another limitation of
623 our approach pertains to the specificity and recombination efficiency of inducible Cre
624 recombinase models, which can be a notable confounding variable (Chakraborty et al., 2019).
625 We observed that our inducible Cre models led to a degree of nonspecific recombination within
626 the murine cLV, with the GCaMP6f and ChR2 particularly susceptible to recombination
627 compared to the ROSA26mT/mG reporter. Recombination in multiple cell types was expected
628 with the constitutive Cre models we employed (*Ng2Cre* and *PdgfrαCre*), as vascular and
629 lymphatic muscle precursor cells can transiently express nestin, PDGFRα, and NG2 (Hill et al.,
630 2015; Castorena-Gonzalez et al., 2018b; Kenney et al., 2020). We also observed that
631 *PdgfrβCreER*^{T2} drove recombination in a sub population of LMCs and PDGFRα^{+} cells. Whether
632 these are two distinct populations that only share expression for PDGFRβ or whether they
633 demonstrate a continuum of precursor LMCs and newly-formed LMCs are both plausible
634 explanations. PDGFB-PDGFRβ signaling is critical for normal mural cell recruitment to both the
635 blood and lymphatic vasculature (Gaengel et al., 2009; Wang et al., 2017) and proliferating
636 vascular smooth muscle cells and pericytes have both been documented to express PDGFRβ
637 (Andrae et al., 2008; Pitulescu and Adams, 2014). We have recently performed single cell
638 RNAseq on isolated IALVs and, while these this dataset is still being analyzed, sub-populations
639 of LMCs, LECs, and CD34^{+} and PDGFRα^{+} were readily identified (data not shown) highlighting
640 the difficulty in ascertaining functionality on the basis of expression of a few cell markers.
641 Ideally, novel Cre or combinatorial Cre models may be developed to further tease out the
642 functional role of these expected sub populations.
643
644 **Materials and Methods**
645 **Mice** Wild-type (WT) male mice (25-35 g) on the C57BL/6J background , ROSA26mT/mG reporter
646 (Muzumdar et al., 2007) (Strain#007676), transgenic *PdgfrαCre* (Strain#013148), CSFR1-EGFP
647 (MacGreen) (Sasmono et al., 2003) (Strain#018549), genetically encoded Ca^{2+} sensor GCaMP6f
648 (Chen et al., 2013) (Strain#028865), transgenic *PdgfrαCreER*^{TM} (Kang et al., 2010)
649 (Strain#018280), NG2-Cre (Strain #:008533) (Zhu et al., 2008), and ChR2 /tdTomato fusion mice
650 (Madisen et al., 2012) (Strain#012567) were purchased from The Jackson Laboratory (Bar Harbor,
651 MA, USA). *PdgfrβCreER*^{T2} (Gerl et al., 2015) mice were a gift from Ralf Adams (Mac Planck
652 Institute) and kindly provided by Lorin Olson (Oklahoma Medical Research Foundation), and are
653 currently available at Jax (Strain#029684). The *Myh11CreER*^{T2} mice (Wirth et al., 2008) were a gift
654 from Stefan Offermanns, Max-Planck-Intstitut fur Herz-und Lungendforschung, Bad Nauheim,
655 Germany, and are currently available at Jax (Strain #019079, Y-Linked). c-KitCreER^{T2} mice (Heger
656 et al., 2014) were a gift from Dieter Saur (Technical University of Munich). Prox1-eGFP mice (Choi
657 et al., 2011) were a gift from Young-Kwon Hong (University of Southern California. For
658 genotyping, we isolated genomic DNA from mouse tail clips using the HotSHOT method (Truett

659 et al., 2000). Specific mouse genotypes were confirmed via PCR using 2x PCR Super Master
660 Polymerase Mix (Catalog # B46019, Bimake, Houston, TX) performed as specified by the provider.
661 Mice were over 3-8 months of age during this study. All animal protocols were approved by the
662 University of Missouri Animal Care and Use Committee and conformed to the US Public Health
663 Service policy for the humane care and use of laboratory animals (PHS Policy, 1996).
664
665 **iCre Tamoxifen Induction**- Mice harboring *PdgfrαCreER*^{TM}, *PdgfrβCreER*^{T2}, *Myh11CreER*^{T2}, and
666 *cKitCreER*^{T2} were crossed with ROSA26mT/mG mice to generate *PdgfrαCreER*^{TM}-ROSA26mT/mG,
667 *PdgfrβCreER*^{T2}-ROSA26mT/mG, *Myh11CreER*^{T2}-ROSA26mT/mG, and *cKitCreER*^{T2}-ROSA26mT/mG
668 mice, respectively. The resulting iCre-ROSA26mT/mG mice were induced with tamoxifen 2-4
669 weeks after weaning. Tamoxifen induction was performed via consecutive 100 µL i.p. injections
670 of tamoxifen ranging from 1 to 5 days at concentration ranging from 0.2 -10 mg/mL in safflower
671 oil, using a titrated induction protocol to determine the extent of recombination in specific cell
672 populations. We used our maximal induction protocol, 100 µL of tamoxifen at 10 mg/mL over 5
673 consecutive days, for *cKitCreER*^{T2}-GCaMP6f, *Myh11CreER*^{T2}-GCaMP6f, and *PdgfrαCreER*^{TM} -
674 GCaMP6f mice. Due to the paucity of recombined cells in the *cKitCreER*^{T2}-ROSA26mT/mG
675 reporter mice, we used our maximal tamoxifen induction protocol for *cKitCreER*^{T2}-ChR2 mice as
676 this still resulted in the ability to excite single recombined cells. *Myh11CreER*^{T2}-ChR2/tdTomato
677 mice were induced with one 100 µL i.p. injection of tamoxifen at 0.2 mg/mL while *PdgfrαCreER*^{TM}-
678 ChR2/tdTomato were induced with 1 injection at 0.4 mg/mL tamoxifen to get mosaic induction
679 sufficient for single cell stimulation. All mice, regardless of duration, were given 2 weeks to
680 recover following tamoxifen injection.
681
682 **Lymphatic Vessel Isolation**- We utilized both popliteal and inguinal-axillary lymphatic collecting
683 vessels (IALVs) in this study, which were isolated as described previously (Zawieja et al., 2018). In
684 brief, mice were anaesthetized with a cocktail of 100/10 mg/mL) ketamine/xylazine mg/mL and
685 shaved along the flank or the legs for IALVs and popliteal cLVs respectively. The IALV (also
686 referred to as the flank cLV) is located adjacent to the thoracoepigastric vein and connects the
687 inguinal and axillary lymph node. A cut was made along the dorsal midline and the skin retracted
688 and pinned out to reveal the thoracoepigastric vascular bed. The thoracoepigastric vascular bed
689 and connected perivascular adipose containing the IALVs vessel was dissected out and pinned
690 onto a Sylgard coated dish in Krebs buffer. Popliteal lymphatic vessels were exposed through a
691 superficial incision in the leg, removed and transferred to the Krebs-albumin filled dissection
692 chamber. After removal, the vessel was carefully cleaned of adipocytes and excess matrix using
693 fine forceps and scissors through micro-dissection. For immunofluorescence, sections containing
694 2-3 valves were isolated, while smaller IALV sections consisting of 1-2 valves were isolated for
695 GCaMP6f Ca^{2+} imaging. Similarly, popliteal cLVs were isolated (Castorena-Gonzalez et al., 2018a)
696 following an incision along the skin overlying the saphenous vein for contractile function analysis
697 and for ChR2 optogenetic depolarization experiments.

698 **Lymphatic Vessel Isobaric Function**- *PdgfrαCreER*^{TM} mice were crossed with Ano1fl/fl, Cx45fl/fl,
699 and Cav1.2fl/fl and to achieve *PdgfrαCreER*^{TM}-Ano1fl/fl, *PdgfrαCreER*^{TM}-Cx45fl/fl, and
700 *PdgfrαCreER*^{TM}-Cav1.2fl/fl mice. Theses mice and their respective fl/fl controls were injected
701 with tamoxifen as described above for 5 days and given two weeks to recover. The popliteal

702 vessels were isolated, cleaned, and prepared for isobaric contractile tests as previously
703 reported (Davis et al., 2023). Once equilibrated, inner diameter was tracked over a physiological
704 pressure range (stepped from 3 to 2, 1, 0.5, 3, 5, 8, and 10 cmH_2O) with 2min of recording at
705 each pressure. Following the pressure step protocol the vessels were equilibrated in with Ca^{2+}-
706 free Krebs buffer (3mM EGTA) and diameter at each pressure recorded under passive
707 conditions. The contractile parameters end diastolic diameter (EDD), end systolic diameter
708 (ESD), and contraction frequency (FREQ) were recorded with a custom LabVIEW program and
709 the following contractile parameters assessed:

710 1) Contraction Amplitude (AMP) = EDD−ESD

711 2) Normalized Contraction Amplitude = ((EDD−ESD)/DMAX) × 100

712 3) Ejection Fraction (EF) = $(EDD^2 - ESD^2)/EDD^2$

713 4) Fractional Pump Flow (FPF) = EF × FREQ

714 5) Tone = ((DMAX−EDD)/DMAX) × 100

715

716 **Methylene Blue-** Isolated IALVs sections were transferred into a Krebs-BSA buffer filled 3-mL
717 observation chamber, with a cover slip bottom, and cannulated onto two glass micropipettes (30-
718 80 µm, outer diameter) held in place by pipette holders on a Burg-style V-track mounting system.
719 The pipette holders were attached to a 3-way valve stop cock with polyethylene tubing filled with
720 Krebs-BSA buffer. Vessels were pressurized to approximately 5 cmH_2O by raising the 3-way valve
721 and the vessels were stretched to remove any slack. For methylene blue staining, IALVs from wild
722 type C57Bl6 mice were stained with 50 µM methylene blue in Krebs-BSA buffer for two hours at
723 room temperature and covered in foil to limit light induced phototoxicity. After the staining
724 period, the vessel chambers were washed three times with Ca^{2+} free PSS to remove methylene
725 blue. Brightfield images and manual Z-stack videos were collected on an inverted Leica DMi1 4X
726 or 20X air objective, or a Leica DMi8 with a 25X water objective or an inverted DMi8 using a Leica
727 Flexacam C1 color camera for image acquisition. Some Methylene blue images were also
728 collected using a color Nikon DS-Fi3 camera. The collected z-stacks were analyzed using Image J
729 and the "Stack Focuser" plugin (https://imagej.nih.gov/ij/plugins/stack-focuser.html). To
730 accentuate the methylene blue stained cells, the color image stack was split into red, green, and
731 blue channel stacks. The blue channel stack was then divided by the green channel stack using
732 the "Image Calculator" function. The resulting 32-bit image was then converted into 16-bit image
733 to permit the use of the Stack Focuser plugin with the 'n kernel value' set to 11.
734

735 **Fluorescence Confocal Imaging-** IALVs vessels from each respective iCre-ROSA26mT/mG mouse
736 were prepared in a similar manner (excluding the addition of methylene blue). We performed
737 confocal imaging to acquire z-stacks of 7-10 overlapping regions of interests to allow for manual
738 stitching, with 1 µM z-steps (20X) or 0.5 µM steps at 40X. We imaged through to the midpoint of
739 the vessel except when imaging the valve interstitial cells, in which case the entire vessel was

740 imaged. Max projections were made using FIJI. Following live imaging, the vessels were
741 pressurized to 5 cmH_2O and fixed with 4% paraformaldehyde for 30 min at room temperature.
742 IALVs were then washed with PBS containing 0.1% Triton X-100 (PBST) 3 times and blocked for a
743 minimum of 2 hr with Blockaid® (B-10710, ThermoFisher Scientific). IALVs were then stained with
744 the corresponding primary antibodies in BlockAid® Solution: anti-smooth muscle actin (SMA)
745 1:500 (Sigma, A2547), anti-GFP 1:200 (ThermoFisher, A11122), anti-cKit 1:100 (Cell Signaling,
746 3074), anti-Vimentin 1:100 (Thermofisher , OMA1-06001), anti-desmin 1:200 (Invitrogen, PA5-
747 16705), anti-GFP 1:200 (Abcam, ab13970, anti-CD34 1:200 (Invitrogen, 14-0341-82), anti-
748 PDGFRA 1:200 (R&DSystems, AF1062), anti-PDGFRβ 1:200 (eBiosciences, 14-1402-82), anti-
749 calponin 1:500 (Abcam, AB46794), anti-MYH11 1:500 (Abcam, AB124679), anti-Sca1 1:200
750 (Biolegend, 108101). IALVs were then washed in PBS and incubated overnight with the
751 corresponding donkey secondary antibodies (ThermoFisher®) at 1:200. After a final wash, IALVs
752 were re-cannulated and pressurized for imaging using the aforementioned spinning disk confocal
753 and Hamamatsu Orca Flash4 camera using a 20X air objective (Olympus UplanApo, 0.75) or 40X
754 (Olympus UApo A340, 1.15) water objective. Images were taken as described above, and the
755 resulting stacks were turned into a max projection using FIJI. Colocalization analysis of the max
756 projections of CD34 and PDGFRα was performed using the BIOP JACoP colocalization plugin
757 (Bolte and Cordelieres, 2006) with both Pearson's and Mander's coefficients reported.
758
759 **LMC Dissociation and FACS Collection-** IALVs vessels *PdgfrαCreER^{TM}*-ROSA26mT/mG,
760 *PdgfrβCreER^{T2}*-ROSA26mT/mG, *Myh11CreER^{T2}*-ROSA26mT/mG, Macgreen, and *Prox1-eGFP* mice
761 were dissected and cleaned of excess adventitia and adipose tissue in Krebs buffer. Isolated
762 vessels were then transferred into a low Ca^{2+} PSS solution supplemented with 0.1 mg/mL bovine
763 serum albumin (BSA, Amersham Life Science, Arlington Heights, IL). Primary LMCs were collected
764 by enzymatic dissociation of IALVs. The dissected vessels were cleaned in room temperature
765 Krebs-BSA buffer and then transferred into a 1-mL tube of low-Ca^{2+} PSS on ice, washed, and
766 equilibrated for 10 min. Vessels were then digested in low-Ca^{2+} PSS with 26 U/mL papain (Sigma,
767 St. Louis, MO) and 1 mg/mL dithioerythritol for 30 min at 37°C and were gently agitated every
768 few minutes. This solution was then decanted and replaced with low-Ca^{2+} PSS with containing
769 1.95 collagenase H (U/mL, Sigma), 1.8 mg/mL collagenase F (Sigma), and 1mg/mL elastase
770 (Worthington LS00635) and incubated for 3 - 5 min at 37° C. The mixture was then spun down at
771 1000 rpm for 4 min, the digestion buffer removed, and replaced with low-Ca^{2+} PS. This process
772 was repeated twice to remove residual digestion buffer. The vessel was then triturated with a
773 fire-polished Pasteur pipette to dissociate the cells into a single cell suspension, passed through
774 a Falcon cap strainer (35 μm), and resuspended in ice-cold low-Ca^{2+} PSS for sorting. For iCre-
775 ROSA26mT/mG mice, GFP^+RFP^- cells or GFP^+ cells from Macgreen and *Prox1-eGFP* mice were then
776 FACS purified straight into RNA isolation buffer for RT-PCR analysis. FACs was performed with a
777 Beckamn-Coulter MoFlo XDP instrument using an excitation laser (488 m) and emission filter
778 (530/40 m). Sorting was performed using 70-µm nozzle at a sheath pressure of 45 p.s.i. and sort
779 rate of 100 events/s and with an efficiency of >90%. To maximize cell yield, we isolated both the
780 left and right full-length IALVs vessels from 2 mice for digestions and subsequent FACS collection.
781 For *Myh11CreER^{T2}*-ROSA26mT/mG and *PdgfraCreER^{TM}*-ROSA26mT/mG, the yield averaged 1000-
782 2000 cells per mouse. For *Prox1-eGFP* mice, LEC yield was typically 1500-2000 cells per mouse.
783

784 **RT-PCR Profiling of FACS Purified Cells**- Total RNA was extracted from FACS purified GFP^+ cells
785 from the isolated IALVs vessels using the Arcturus PicoPure RNA isolation kit (ThermoFisher
786 Scientific, Waltham, MA) per the listed instructions. Prior to elution in 20 μl of water, on-column
787 DNAse digestion (Qiagen, Valencia, CA) was performed to ensure removal of genomic DNA
788 contaminants. RNA was converted into cDNA using SuperScript III First-Strand Synthesis System
789 (Thermo Fisher Scientific, Waltham, MA) using oligo (dT) and random hexamer priming following
790 the manufacturer's protocol. Each RT reaction used approximately 50-100 cells worth of RNA
791 based on the sorted cells count number. Our PCR reaction mixture contained first-strand cDNA
792 as the template, 2 mM $MgCl_2$, 0.25 μM primers, 0.2 mM deoxynucleotide triphosphates; and
793 GoTaq® Flexi DNA polymerase (Promega, Madison, WI). The PCR program comprised an initial
794 denaturation step at 95°C for four min; followed by 35 repetitions of the following cycle:
795 denaturation (94° C, 30 s), annealing (58° C, 30 s), and extension (72° C, 30 s). This was followed
796 by a final elongation step for 5 min at 72° C. PCR amplification products were separated on a 2%
797 agarose gel by electrophoresis, stained with SYBR-Safe (Thermo Fisher Scientific, Waltham, MA),
798 and visualized by UV trans-illumination. All primers were designed to amplify an intron-spanning
799 region. Endpoint RT-PCR Primer sequences, amplicon size, accession numbers, and source are
800 listed in Table 1.
801
802 ***Ex vivo* Ca^{2+} imaging with the genetically encoded GCaMP6f Indicator**- *cKitCreER^{T2}*,
803 *Myh11CreER^{T2}*, and *PdgfrαCreER^{TM}* mice were crossed with GCaMP6f mice in a similar manner as
804 described for ROSA26mT/mG. *cKitCreER^{T2}*-GCaMP6f, *PdgfrαCreER^{TM}*-GCaMP6f, and
805 *Myh11CreER^{T2}*-GCaMP6f were induced with tamoxifen (10 mg/mL) for 5 consecutive days by i.p.
806 injection. IALVs isolated from *cKitCreER^{T2}*-GCaMP6f, *PdgfrαCreER^{TM}*-GCaMP6f, and
807 *Myh11CreER^{T2}*-GCaMP6f were cannulated as described above. The cannulated vessel, with
808 micropipette holders, observation chamber and V-track mounting system, was transferred to the
809 stage of the spinning disk confocal with a Prime95B scMOS camera (Photometrics), a Cascade II
810 EMCCD (Photometrics), or an Ixon888 EMCCD camera (Andor) for Ca^{2+} imaging (Castorena-
811 Gonzalez et al., 2018b). Pressures for the input and output cannula were connected to a T-
812 junction which was set briefly to 8 cmH_2O and the vessel lengthened to remove axial slack. A
813 peristaltic pump maintained constant perfusion of the observation chamber with Krebs buffer at
814 a rate of 0.5 mL/min while the vessel equilibrated at 37°C for 30-60 min with pressures set to 3
815 cmH_2O. Spontaneous contractions were allowed to stabilize over a period of 30 min and then
816 were blunted with 2 μM wortmannin to limit movement associated with contractions during Ca^{2+}
817 imaging. A Windows-based computer was used to digitize the pressure transducer signals and
818 video image of the vessel from a firewire camera at 30-40 Hz (Davis et al., 2012). A custom-
819 written LabVIEW program (National Instruments; Austin, TX) detected the inner diameter of the
820 vessel from the video (Davis et al., 2011). Once contractions were <5 μm in amplitude, Ca^{2+}
821 recordings were made at 20FPS for 20-40 s.
822
823 **Ca^{2+} Imaging and Analysis in IALVs Over the Contraction Cycle-** Background noise was
824 determined by using the histogram feature of FIJI in a rectangle in a region of the field of view
825 without sample. This value was subtracted from the entire field of view. In some cases, the vessel
826 movement due to contraction was offset with video stabilization with the FIJI plugin Image
827 Stabilizer. A max projection was used to create non-overlapping ROIs of $GCaMP6f^+$ cells for each

828 iCre-GCaMp6f IALV. From these cell ROIs, the "reslice z" function was used to create a pseudo-
829 linescan STMs which were divided by their baseline values to obtain F/F_0 values for each
830 individual cell. At least 3 cells, except in the case of 1 *cKitCreER*^{T2}-GCaMp6f IALV, in which only
831 two cells were observed, were analyzed in this manner for each vessel segment. Max projections
832 of the image stack were then used to create non-overlapping cell masks of 3-5 muscle cells per
833 field of view of one vessel. Ca^{2+} traces for those cells contained 5-10 contraction cycles and Ca^{2+}
834 transients and were characterized for peak intensity (expressed as a baseline-referenced ratio,
835 F/F_0), frequency, and duration in seconds.
836
837 **Analysis of Subcellular Ca^{2+} Transients in *Myh11CreER*^{T2}-GCaMP6f IALVs** For *Myh11CreER*^{T2}-We
838 performed Ca^{2+} imaging as above in the presence of 1 µM nifedipine to stop the "Ca^{2+} flashes"
839 associated with action potentials (Zawieja et al., 2018) and focus on the subcellular activity at 3
840 different experimental pressures of 0.5, 2, and 5 cmH_2O. For this protocol, we used a particle
841 analysis approach to analyze all Ca^{2+} transients in the field of view. Ca^{2+} transients in intact vessels
842 were quantified by particle analysis as previously described (Drumm et al., 2017; Drumm et al.,
843 2019). Movies of Ca^{2+} transients in intact vessels were imported into custom built Volumetry
844 software (version G8d) and background subtracted. Movies were smoothed using a Gaussian
845 filter: 1.5 x 1.5 mM, StdDev 1.0). Raw Ca^{2+} transients were converted to Ca^{2+} particles (PTCLs)
846 using a flood-fill algorithm as previously described (Drumm et al., 2017; Drumm et al., 2019).
847 PTCLs <10 mm^2 were rejected to facilitate the removal of noise and then the total PTCL area and
848 PTCL count could be tabulated for each recording.
849
850 **Light Activation of ChR2 to stimulate Popliteal Collecting Lymphatic Vessel Contractions.**
851 As the IALV has a nearly continuous contractile cycle, we utilized the popliteal vessel for its much
852 slower contraction frequency in the experiments testing our ability to trigger a propagated
853 contraction upon stimulation of the enforced expression of ChR2. Popliteal vessels were isolated
854 from *cKitCreER*^{T2}-ChR2/tdTomato, *PdgfrαCreER*^{TM} -ChR2/tdTomato, or *Myh11CreER*^{T2}-
855 ChR2/tdTomato mice as previously described (Scallan and Davis, 2013), although we intentionally
856 retained some connective tissue and adipose tissue to ensure we had a sufficient population of
857 recombined cells to test in the adventitia layer of the vessel. Contractions were allowed to
858 stabilize over a 30-min equilibration period with pressure set to 3 cmH_2O. If basal contraction
859 frequency was too high, we applied pinacidil to the bath in 100 nM increments, without
860 exceeding 600 nM, to further slow contraction frequency to around 6 contractions per minute.
861 Pinacidil at sub 1 µM doses can slow contraction frequency without causing overt
862 hyperpolarization of membrane potential (Davis et al., 2020). Supplemental 100 nM doses of
863 pinacidil were applied throughout the experiment to maintain a spontaneous contraction
864 frequency below 6 per minute to allow ample diastolic time for ChR2 stimulation. Throughout
865 this protocol the popliteal was allowed to contract spontaneously to ensure we had not overly
866 inhibited action potentials by the pacemaking cells with pinacidil. Occasionally spontaneous
867 contractions occurred just prior to contractions and could result in a potential false positive so
868 we performed multiple stimulations over a period of 5 - 10 min, typically waiting at least 3 s after
869 any spontaneous contraction before stimulating. Care was made to align the light fiber in such a
870 way that only part of the vessel would be directly illuminated and so target cells of interest would
871 be directly activated by 473 nm light using a Laser diode (Doric LD Fiber Light Source, Quebec,

872 Canada), through an optical probe with a 10-µm tip (Doric, OPT_200_0.22.010). To further limit
873 the excitation field, the optical probe was coated with black acrylic paint using an eyelash brush
874 so that the uncoated opening was ~2-3 µm. With the probe positioned within 5 µm of one side
875 of the vessel wall, the spread of light covered an area ~10-100 µm wide on the back side of the
876 vessel (depending on the diode amplitude setting). Light pulses, 200 ms in length, were triggered
877 by a Grass S9 stimulator (Harvard Apparatus, Holliston, MA) connected to the external TTL input
878 of the laser diode. Pulse amplitude was adjusted between 40-90 mA using the Laser Diode
879 Module Driver (Doric). A contraction was considered to be triggered if it occurred within 50ms of
880 stimulation. We performed photo-stimulation from 2-4 sites within each vessel, with 6-14
881 stimulations per site. If a photo-stimulation was triggered incidentally after the initiation of a
882 "spontaneous contraction" it was discarded from the analysis. For *Myh11CreER*^{T2}-ChR2-
883 tdTomato 6 vessels from 3 separate mice were tested. For *PdgfrαCreER*^{TM}-ChR2-tdTomato 6
884 vessels from 4 separate mice were tested with a max of two vessels per mouse. For *cKitCreER*^{T2}-
885 ChR2-tdTomato 7 vessels from 3 separate mice were assessed. Diameter was recorded to align
886 photo-activation with the contraction cycle in a custom Labview program.
887
888 **Solutions and Chemicals**. Krebs buffer was composed of (in mM): 146.9 NaCl, 4.7 KCl, 2 $CaCl_2$,
889 1.2 $MgSO_4$, 1.2 $NaH_2PO_4 \bullet H_2O$, 3 $NaHCO_3$, 1.5 NaHEPES, and 5 d-glucose (pH = 7.4 at 37°C). Krebs-
890 BSA buffer was prepared with the addition of 0.5% (w/v) bovine serum albumin (BSA) while Krebs
891 Ca^{2+}-free replaced $CaCl_2$ with 3mM EGTA. Tamoxifen was dissolved to 10mg/ml in a Safflower Oil-
892 Ethanol (95%-5% v/v) solution with rocking agitation, separated into aliquots, and stored at -20
893 °C. Wortmannin was dissolved in DMSO to a stock solution of 1 mM. Pinacidil was dissolved in
894 DMSO to a stock concentration of 1 µM. Nifedipine was dissolved in DMSO to a stock
895 concentration of 1 mM. All chemicals were obtained from Sigma (St. Louis, MO), with the
896 exception of BSA (US Biochemicals; Cleveland, OH), $MgSO_4$ and NaHEPES (Fisher Scientific;
897 Pittsburgh, PA).
898

899 **Statistical Tests** Statistical differences in the isobaric contractile tests for popliteal cLVs isolated
900 from *PdgfrαCreER*^{TM}-Ano1fl/fl, *PdgfrαCreER*^{TM}-Cx45fl/fl, and *PdgfrαCreER*^{TM}-Cav1.2fl/fl mice
901 over the various contractile parameters were assessed via 1) two-way ANOVAs with Tukey's
902 multiple comparison tests data performed using Prism9 (Graphpad). Data are plotted as mean ±
903 SEM and significance determined at $p < 0.05$. We used a categorical Chi-squared statistical test
904 for the experiments assessing our ability to trigger a contraction with activation of ChR2 cells.
905 Ca^{2+} PTCL area and frequency was compared using 1-way ANOVA with Tukey's post-hoc test.
906 Significance was determined at a p value of < 0.05.

907
908 **Acknowledgements**
909 We would like to thank Stefan Offermanns for donation of the *Myh11CreER*^{T2} mice, Klaus
910 Willecke for his donation of Cx45$^{f/f}$ mice, Dieter Sauer for his donation of *cKitCreER*^{T2} mice,
911 Ralph Adams for his donation of the *PdgfrβCreER*^{T2} mice and to Young Hong (University of
912 Southern California) for his donation of the *Prox1-eGFP* mice (Choi et al., 2011).
913

Author contributions: S.D. Zawieja, J.A. Castorena-Gonzalez and M. J. Davis conceived and designed the experiments. S.D. Zawieja, S.E. Broyhill, J.A. Castorena-Gonzalez, H.J. Kim, B. Drumm, M. Li, C.E. Norton, and M.J. Davis performed the studies, collected, and analyzed and interpreted the data. S.D. Zawieja and M.J. Davis drafted the manuscript and all authors participated in critically revising the manuscript for intellectual concepts and content. All authors have approved the final draft of the manuscript and their contributions qualify them as authors.
The authors declare no competing financial interests. This work was supported by NIH HL-122608 and HL-122578 to MJD, HL-143198 to SDZ, and HL-141143 and HL-168568 to JAC-G, and AHA CDA-931652 to CEN.

Aalkjaer, C., D. Boedtkjer, and V. Matchkov. 2011. Vasomotion - what is currently thought? *Acta Physiol (Oxf)*. 202:253-269.
Andrae, J., R. Gallini, and C. Betsholtz. 2008. Role of platelet-derived growth factors in physiology and medicine. *Genes Dev*. 22:1276-1312.
Baker, S.A., B.T. Drumm, D. Saur, G.W. Hennig, S.M. Ward, and K.M. Sanders. 2016. Spontaneous Ca(2+) transients in interstitial cells of Cajal located within the deep muscular plexus of the murine small intestine. *J Physiol*. 594:3317-3338.
Baker, S.A., S.J. Hwang, P.J. Blair, C. Sireika, L. Wei, S. Ro, S.M. Ward, and K.M. Sanders. 2021a. Ca(2+) transients in ICC-MY define the basis for the dominance of the corpus in gastric pacemaking. *Cell Calcium*. 99:102472.
Baker, S.A., W.A. Leigh, G. Del Valle, I.F. De Yturriaga, S.M. Ward, C.A. Cobine, B.T. Drumm, and K.M. Sanders. 2021b. Ca(2+) signaling driving pacemaker activity in submucosal interstitial cells of Cajal in the murine colon. *Elife*. 10.
Basciani, S., S. Mariani, M. Arizzi, M. Brama, A. Ricci, C. Betsholtz, C. Bondjers, G. Ricci, A. Catizone, M. Galdieri, G. Spera, and L. Gnessi. 2004. Expression of platelet-derived growth factor (PDGF) in the epididymis and analysis of the epididymal development in PDGF-A, PDGF-B, and PDGF receptor beta deficient mice. *Biol Reprod*. 70:168-177.
Benoit, J.N., D.C. Zawieja, A.H. Goodman, and H.J. Granger. 1989. Characterization of intact mesenteric lymphatic pump and its responsiveness to acute edemagenic stress. *Am J Physiol*. 257:H2059-2069.
Boedtkjer, D.M., V.V. Matchkov, E. Boedtkjer, H. Nilsson, and C. Aalkjaer. 2008. Vasomotion has chloride-dependency in rat mesenteric small arteries. *Pflugers Arch*. 457:389-404.
Bolte, S., and F.P. Cordelieres. 2006. A guided tour into subcellular colocalization analysis in light microscopy. *J Microsc*. 224:213-232.
Bridenbaugh, E.A., W. Wang, M. Srimushnam, W.E. Cromer, S.D. Zawieja, S.E. Schmidt, D.C. Jupiter, H.C. Huang, V. Van Buren, and D.C. Zawieja. 2013. An immunological fingerprint differentiates muscular lymphatics from arteries and veins. *Lymphat Res Biol*. 11:155-171.
Briggs Boedtkjer, D., J. Rumessen, U. Baandrup, M. Skov Mikkelsen, N. Telinius, H. Pilegaard, C. Aalkjaer, and V. Hjortdal. 2013. Identification of interstitial Cajal-like cells in the human thoracic duct. *Cells Tissues Organs*. 197:145-158.
Castorena-Gonzalez, J.A., J.P. Scallan, and M.J. Davis. 2018a. Methods for Assessing the Contractile Function of Mouse Lymphatic Vessels Ex Vivo. *Methods in molecular biology*. 1846:229-248.

960 Castorena-Gonzalez, J.A., S.D. Zawieja, M. Li, R.S. Srinivasan, A.M. Simon, C. de Wit, R. de la
961 Torre, L.A. Martinez-Lemus, G.W. Hennig, and M.J. Davis. 2018b. Mechanisms of
962 Connexin-Related Lymphedema. *Circ Res*. 123:964-985.
963 Chakraborty, R., F.Z. Saddouk, A.C. Carrao, D.S. Krause, D.M. Greif, and K.A. Martin. 2019.
964 Promoters to Study Vascular Smooth Muscle. *Arterioscler Thromb Vasc Biol*. 39:603-
965 612.
966 Chakraborty, S., S.D. Zawieja, W. Wang, Y. Lee, Y.J. Wang, P.Y. von der Weid, D.C. Zawieja,
967 and M. Muthuchamy. 2015. Lipopolysaccharide modulates neutrophil recruitment and
968 macrophage polarization on lymphatic vessels and impairs lymphatic function in rat
969 mesentery. *Am J Physiol Heart Circ Physiol*.ajpheart 00467 02015.
970 Chatterjee, V., and A.A. Gashev. 2012. Aging-associated shifts in functional status of mast cells
971 located by adult and aged mesenteric lymphatic vessels. *Am J Physiol Heart Circ*
972 *Physiol*. 303:H693-702.
973 Chen, T.W., T.J. Wardill, Y. Sun, S.R. Pulver, S.L. Renninger, A. Baohan, E.R. Schreiter, R.A.
974 Kerr, M.B. Orger, V. Jayaraman, L.L. Looger, K. Svoboda, and D.S. Kim. 2013.
975 Ultrasensitive fluorescent proteins for imaging neuronal activity. *Nature*. 499:295-300.
976 Cheng, X., J. Liu, M. Asuncion-Chin, E. Blaskova, J.P. Bannister, A.M. Dopico, and J.H. Jaggar.
977 2007. A novel Ca(V)1.2 N terminus expressed in smooth muscle cells of resistance size
978 arteries modifies channel regulation by auxiliary subunits. *J Biol Chem*. 282:29211-
979 29221.
980 Choi, I., H.K. Chung, S. Ramu, H.N. Lee, K.E. Kim, S. Lee, J. Yoo, D. Choi, Y.S. Lee, B.
981 Aguilar, and Y.K. Hong. 2011. Visualization of lymphatic vessels by Prox1-promoter
982 directed GFP reporter in a bacterial artificial chromosome-based transgenic mouse.
983 *Blood*. 117:362-365.
984 Clayton, D.R., W.G. Ruiz, M.G. Dalghi, N. Montalbetti, M.D. Carattino, and G. Apodaca. 2022.
985 Studies of ultrastructure, gene expression, and marker analysis reveal that mouse bladder
986 PDGFRA(+) interstitial cells are fibroblasts. *Am J Physiol Renal Physiol*. 323:F299-
987 F321.
988 Cobine, C.A., E.E. Hannah, M.H. Zhu, H.E. Lyle, J.R. Rock, K.M. Sanders, S.M. Ward, and
989 K.D. Keef. 2017. ANO1 in intramuscular interstitial cells of Cajal plays a key role in the
990 generation of slow waves and tone in the internal anal sphincter. *J Physiol*. 595:2021-
991 2041.
992 Davis, M.J., J.A. Castorena-Gonzalez, H.J. Kim, M. Li, M. Remedi, and C.G. Nichols. 2023.
993 Lymphatic contractile dysfunction in mouse models of Cantu Syndrome with K(ATP)
994 channel gain-of-function. *Function (Oxf)*. 4:zqad017.
995 Davis, M.J., H.J. Kim, M. Li, and S.D. Zawieja. 2022. A vascular smooth muscle-specific
996 integrin-alpha8 Cre mouse for lymphatic contraction studies that allows male-female
997 comparisons and avoids visceral myopathy. *Front Physiol*. 13:1060146.
998 Davis, M.J., H.J. Kim, S.D. Zawieja, J.A. Castorena-Gonzalez, P. Gui, M. Li, B.T. Saunders,
999 B.H. Zinselmeyer, G.J. Randolph, M.S. Remedi, and C.G. Nichols. 2020. Kir6.1-
1000 dependent KATP channels in lymphatic smooth muscle and vessel dysfunction in mice
1001 with Kir6.1 gain-of-function. *J Physiol*.
1002 Davis, M.J., E. Rahbar, A.A. Gashev, D.C. Zawieja, and J.E. Moore, Jr. 2011. Determinants of
1003 valve gating in collecting lymphatic vessels from rat mesentery. *Am J Physiol Heart Circ*
1004 *Physiol*. 301:H48-60.

1005 Davis, M.J., J.P. Scallan, J.H. Wolpers, M. Muthuchamy, A.A. Gashev, and D.C. Zawieja. 2012.
1006 Intrinsic increase in lymphangion muscle contractility in response to elevated afterload.
1007 *Am J Physiol Heart Circ Physiol*. 303:H795-808.
1008 Drumm, B.T., G.W. Hennig, S.A. Baker, and K.M. Sanders. 2019. Applications of spatio-
1009 temporal mapping and particle analysis techniques to quantify intracellular Ca 2+
1010 signaling in situ. *Journal of Visualized Experiments*. 2019:1-13.
1011 Drumm, B.T., G.W. Hennig, M.J. Battersby, E.K. Cunningham, T.S. Sung, S.M. Ward, K.M.
1012 Sanders, and S.A. Baker. 2017. Clustering of Ca2+ transients in interstitial cells of Cajal
1013 defines slow wave duration. *The Journal of General Physiology*. 149:703-725.
1014 Drumm, B.T., B.E. Rembetski, C.A. Cobine, S.A. Baker, G.P. Sergeant, M.A. Hollywood, K.D.
1015 Thornbury, and K.M. Sanders. 2018. Ca(2+) signalling in mouse urethral smooth muscle
1016 in situ: role of Ca(2+) stores and Ca(2+) influx mechanisms. *J Physiol*. 596:1433-1466.
1017 Engeset, A., W. Olszewski, P.M. Jaeger, J. Sokolowski, and L. Theodorsen. 1977. Twenty-four
1018 hour variation in flow and composition of leg lymph in normal men. *Acta physiologica*
1019 *Scandinavica*. 99:140-148.
1020 Ferrusi, I., J. Zhao, D. van Helden, and P.Y. von der Weid. 2004. Cyclopiazonic acid decreases
1021 spontaneous transient depolarizations in guinea pig mesenteric lymphatic vessels in
1022 endothelium-dependent and -independent manners. *Am J Physiol Heart Circ Physiol*.
1023 286:H2287-2295.
1024 Gaengel, K., G. Genove, A. Armulik, and C. Betsholtz. 2009. Endothelial-mural cell signaling in
1025 vascular development and angiogenesis. *Arterioscler Thromb Vasc Biol*. 29:630-638.
1026 Gashev, A.A., M.J. Davis, M.D. Delp, and D.C. Zawieja. 2004. Regional variations of
1027 contractile activity in isolated rat lymphatics. *Microcirculation*. 11:477-492.
1028 Geng, X., B. Cha, M.R. Mahamud, K.C. Lim, R. Silasi-Mansat, M.K.M. Uddin, N. Miura, L.
1029 Xia, A.M. Simon, J.D. Engel, H. Chen, F. Lupu, and R.S. Srinivasan. 2016. Multiple
1030 mouse models of primary lymphedema exhibit distinct defects in lymphovenous valve
1031 development. *Dev Biol*. 409:218-233.
1032 Gerl, K., L. Miquerol, V.T. Todorov, C.P. Hugo, R.H. Adams, A. Kurtz, and B. Kurt. 2015.
1033 Inducible glomerular erythropoietin production in the adult kidney. *Kidney Int*. 88:1345-
1034 1355.
1035 Gomez-Pinilla, P.J., S.J. Gibbons, M.R. Bardsley, A. Lorincz, M.J. Pozo, P.J. Pasricha, M. Van
1036 de Rijn, R.B. West, M.G. Sarr, M.L. Kendrick, R.R. Cima, E.J. Dozois, D.W. Larson, T.
1037 Ordog, and G. Farrugia. 2009. Ano1 is a selective marker of interstitial cells of Cajal in
1038 the human and mouse gastrointestinal tract. *Am J Physiol Gastrointest Liver Physiol*.
1039 296:G1370-1381.
1040 Grainger, N., C.C. Shonnard, S.K. Quiggle, E.B. Fox, H. Presley, R. Daugherty, M.C. Shonnard,
1041 B.T. Drumm, and K.M. Sanders. 2022. Propagation of Pacemaker Activity and Peristaltic
1042 Contractions in the Mouse Renal Pelvis Rely on Ca(2+)-activated Cl(-) Channels and T-
1043 Type Ca(2+) Channels. *Function (Oxf)*. 3:zqac041.
1044 Hald, B.O., J.A. Castorena-Gonzalez, S.D. Zawieja, P. Gui, and M.J. Davis. 2018. Electrical
1045 Communication in Lymphangions. *Biophys J*. 115:936-949.
1046 Hashitani, H., R. Mitsui, S. Masaki, and D.F. Van Helden. 2015. Pacemaker role of pericytes in
1047 generating synchronized spontaneous Ca2+ transients in the myenteric microvasculature
1048 of the guinea-pig gastric antrum. *Cell Calcium*. 58:442-456.
1049 Heger, K., B. Seidler, J.C. Vahl, C. Schwartz, M. Kober, S. Klein, D. Voehringer, D. Saur, and
1050 M. Schmidt-Supprian. 2014. CreER(T2) expression from within the c-Kit gene locus

1051 allows efficient inducible gene targeting in and ablation of mast cells. *Eur J Immunol*.
1052 44:296-306.
1053 Hill, R.A., L. Tong, P. Yuan, S. Murikinati, S. Gupta, and J. Grutzendler. 2015. Regional Blood
1054 Flow in the Normal and Ischemic Brain Is Controlled by Arteriolar Smooth Muscle Cell
1055 Contractility and Not by Capillary Pericytes. *Neuron*. 87:95-110.
1056 Huizinga, J.D., L. Thuneberg, M. Kluppel, J. Malysz, H.B. Mikkelsen, and A. Bernstein. 1995.
1057 W/kit gene required for interstitial cells of Cajal and for intestinal pacemaker activity.
1058 *Nature*. 373:347-349.
1059 Hwang, S.J., P.J. Blair, F.C. Britton, K.E. O'Driscoll, G. Hennig, Y.R. Bayguinov, J.R. Rock,
1060 B.D. Harfe, K.M. Sanders, and S.M. Ward. 2009. Expression of anoctamin 1/TMEM16A
1061 by interstitial cells of Cajal is fundamental for slow wave activity in gastrointestinal
1062 muscles. *J Physiol*. 587:4887-4904.
1063 Imtiaz, M.S., J. Zhao, K. Hosaka, P.Y. von der Weid, M. Crowe, and D.F. van Helden. 2007.
1064 Pacemaking through Ca2+ stores interacting as coupled oscillators via membrane
1065 depolarization. *Biophys J*. 92:3843-3861.
1066 Jolly, A.J., S. Lu, K.A. Strand, A.M. Dubner, M.F. Mutryn, R.A. Nemenoff, M.W. Majesky,
1067 K.S. Moulton, and M.C.M. Weiser-Evans. 2022. Heterogeneous subpopulations of
1068 adventitial progenitor cells regulate vascular homeostasis and pathological vascular
1069 remodelling. *Cardiovasc Res*. 118:1452-1465.
1070 Kang, S.H., M. Fukaya, J.K. Yang, J.D. Rothstein, and D.E. Bergles. 2010. NG2+ CNS glial
1071 progenitors remain committed to the oligodendrocyte lineage in postnatal life and
1072 following neurodegeneration. *Neuron*. 68:668-681.
1073 Kenney, H.M., R.D. Bell, E.A. Masters, L. Xing, C.T. Ritchlin, and E.M. Schwarz. 2020.
1074 Lineage tracing reveals evidence of a popliteal lymphatic muscle progenitor cell that is
1075 distinct from skeletal and vascular muscle progenitors. *Sci Rep*. 10:18088.
1076 Kimura, K., K. Ramirez, T.A.V. Nguyen, Y. Yamashiro, A. Sada, and H. Yanagisawa. 2021.
1077 Contribution of PDGFRalpha-positive cells in maintenance and injury responses in
1078 mouse large vessels. *Sci Rep*. 11:8683.
1079 Koval, M., S.A. Molina, and J.M. Burt. 2014. Mix and match: investigating heteromeric and
1080 heterotypic gap junction channels in model systems and native tissues. *FEBS Lett*.
1081 588:1193-1204.
1082 Kramann, R., R.K. Schneider, D.P. DiRocco, F. Machado, S. Fleig, P.A. Bondzie, J.M.
1083 Henderson, B.L. Ebert, and B.D. Humphreys. 2015. Perivascular Gli1+ progenitors are
1084 key contributors to injury-induced organ fibrosis. *Cell Stem Cell*. 16:51-66.
1085 Kurahashi, M., Y. Nakano, L.E. Peri, J.B. Townsend, S.M. Ward, and K.M. Sanders. 2013. A
1086 novel population of subepithelial platelet-derived growth factor receptor alpha-positive
1087 cells in the mouse and human colon. *Am J Physiol Gastrointest Liver Physiol*. 304:G823-
1088 834.
1089 Kurahashi, M., H. Zheng, L. Dwyer, S.M. Ward, S.D. Koh, and K.M. Sanders. 2011. A
1090 functional role for the 'fibroblast-like cells' in gastrointestinal smooth muscles. *J Physiol*.
1091 589:697-710.
1092 Lee, Y., S. Chakraborty, and M. Muthuchamy. 2020. Roles of sarcoplasmic reticulum Ca(2+)
1093 ATPase pump in the impairments of lymphatic contractile activity in a metabolic
1094 syndrome rat model. *Sci Rep*. 10:12320.

1095 Li, S.W., C.Y. Wang, Y.J. Jou, T.C. Yang, S.H. Huang, L. Wan, Y.J. Lin, and C.W. Lin. 2016.
1096 SARS coronavirus papain-like protease induces Egr-1-dependent up-regulation of TGF-
1097 beta1 via ROS/p38 MAPK/STAT3 pathway. *Sci Rep*. 6:25754.
1098 Madisen, L., T. Mao, H. Koch, J.M. Zhuo, A. Berenyi, S. Fujisawa, Y.W. Hsu, A.J. Garcia, 3rd,
1099 X. Gu, S. Zanella, J. Kidney, H. Gu, Y. Mao, B.M. Hooks, E.S. Boyden, G. Buzsaki, J.M.
1100 Ramirez, A.R. Jones, K. Svoboda, X. Han, E.E. Turner, and H. Zeng. 2012. A toolbox of
1101 Cre-dependent optogenetic transgenic mice for light-induced activation and silencing.
1102 *Nat Neurosci*. 15:793-802.
1103 Maeda, H., A. Yamagata, S. Nishikawa, K. Yoshinaga, S. Kobayashi, K. Nishi, and S.
1104 Nishikawa. 1992. Requirement of c-kit for development of intestinal pacemaker system.
1105 *Development*. 116:369-375.
1106 Majesky, M.W., H. Horita, A. Ostriker, S. Lu, J.N. Regan, A. Bagchi, X.R. Dong, J. Poczobutt,
1107 R.A. Nemenoff, and M.C. Weiser-Evans. 2017. Differentiated Smooth Muscle Cells
1108 Generate a Subpopulation of Resident Vascular Progenitor Cells in the Adventitia
1109 Regulated by Klf4. *Circ Res*. 120:296-311.
1110 Malysz, J., S.J. Gibbons, S.A. Saravanaperumal, P. Du, S.T. Eisenman, C. Cao, U. Oh, D. Saur,
1111 S. Klein, T. Ordog, and G. Farrugia. 2017. Conditional genetic deletion of Ano1 in
1112 interstitial cells of Cajal impairs Ca(2+) transients and slow waves in adult mouse small
1113 intestine. *Am J Physiol Gastrointest Liver Physiol*. 312:G228-G245.
1114 McCloskey, K.D., M.A. Hollywood, K.D. Thornbury, S.M. Ward, and N.G. McHale. 2002. Kit-
1115 like immunopositive cells in sheep mesenteric lymphatic vessels. *Cell Tissue Res*.
1116 310:77-84.
1117 Mitsui, R., and H. Hashitani. 2020. Synchrony of spontaneous Ca(2+) activity in microvascular
1118 mural cells. *Journal of smooth muscle research = Nihon Heikatsukin Gakkai kikanshi*.
1119 56:1-18.
1120 Mohanakumar, S., J. Majgaard, N. Telinius, N. Katballe, E. Pahle, V.E. Hjortdal, and D.M.B.
1121 Boedtkjer. 2018. Spontaneous and alpha-adrenoceptor-induced contractility in human
1122 collecting lymphatic vessels require chloride. *Am J Physiol Heart Circ Physiol*.
1123 Muzumdar, M.D., B. Tasic, K. Miyamichi, L. Li, and L. Luo. 2007. A global double-fluorescent
1124 Cre reporter mouse. *Genesis*. 45:593-605.
1125 Olszewski, W.L. 2002. Contractility patterns of normal and pathologically changed human
1126 lymphatics. *Ann N Y Acad Sci*. 979:52-63; discussion 76-59.
1127 Olszewski, W.L. 2008. Contractility patterns of human leg lymphatics in various stages of
1128 obstructive lymphedema. *Ann N Y Acad Sci*. 1131:110-118.
1129 Ordog, T., S.M. Ward, and K.M. Sanders. 1999. Interstitial cells of cajal generate electrical slow
1130 waves in the murine stomach. *J Physiol*. 518:257-269.
1131 Pitulescu, M.E., and R.H. Adams. 2014. Regulation of signaling interactions and receptor
1132 endocytosis in growing blood vessels. *Cell Adh Migr*. 8:366-377.
1133 Popescu, L.M., and M.S. Faussone-Pellegrini. 2010. TELOCYTES - a case of serendipity: the
1134 winding way from Interstitial Cells of Cajal (ICC), via Interstitial Cajal-Like Cells
1135 (ICLC) to TELOCYTES. *J Cell Mol Med*. 14:729-740.
1136 Sanders, K.M., S.A. Baker, B.T. Drumm, and M. Kurahashi. 2022. Ca(2+) Signaling Is the Basis
1137 for Pacemaker Activity and Neurotransduction in Interstitial Cells of the GI Tract. *Adv*
1138 *Exp Med Biol*. 1383:229-241.
1139 Sanders, K.M., T. Ordog, S.D. Koh, S. Torihashi, and S.M. Ward. 1999. Development and
1140 plasticity of interstitial cells of Cajal. *Neurogastroenterol Motil*. 11:311-338.

1141 Sanders, K.M., S.M. Ward, and S.D. Koh. 2014. Interstitial cells: regulators of smooth muscle
1142 function. *Physiol Rev*. 94:859-907.
1143 Sasmono, R.T., D. Oceandy, J.W. Pollard, W. Tong, P. Pavli, B.J. Wainwright, M.C. Ostrowski,
1144 S.R. Himes, and D.A. Hume. 2003. A macrophage colony-stimulating factor receptor-
1145 green fluorescent protein transgene is expressed throughout the mononuclear phagocyte
1146 system of the mouse. *Blood*. 101:1155-1163.
1147 Scallan, J.P., and M.J. Davis. 2013. Genetic removal of basal nitric oxide enhances contractile
1148 activity in isolated murine collecting lymphatic vessels. *J Physiol*. 591:2139-2156.
1149 Scallan, J.P., S.D. Zawieja, J.A. Castorena-Gonzalez, and M.J. Davis. 2016. Lymphatic
1150 pumping: Mechanics, mechanisms and malfunction. *J Physiol*.
1151 Sidney, L.E., M.J. Branch, S.E. Dunphy, H.S. Dua, and A. Hopkinson. 2014. Concise review:
1152 evidence for CD34 as a common marker for diverse progenitors. *Stem Cells*. 32:1380-
1153 1389.
1154 Singh, R.D., S.J. Gibbons, S.A. Saravanaperumal, P. Du, G.W. Hennig, S.T. Eisenman, A.
1155 Mazzone, Y. Hayashi, C. Cao, G.J. Stoltz, T. Ordog, J.R. Rock, B.D. Harfe, J.H.
1156 Szurszewski, and G. Farrugia. 2014. Ano1, a Ca2+-activated Cl- channel, coordinates
1157 contractility in mouse intestine by Ca2+ transient coordination between interstitial cells
1158 of Cajal. *J Physiol*. 592:4051-4068.
1159 Song, K., Y. Qing, Q. Guo, E.K. Peden, C. Chen, W.E. Mitch, L. Truong, and J. Cheng. 2020.
1160 PDGFRA in vascular adventitial MSCs promotes neointima formation in arteriovenous
1161 fistula in chronic kidney disease. *JCI Insight*. 5.
1162 Spandidos, A., X. Wang, H. Wang, S. Dragnev, T. Thurber, and B. Seed. 2008. A
1163 comprehensive collection of experimentally validated primers for Polymerase Chain
1164 Reaction quantitation of murine transcript abundance. *BMC Genomics*. 9:633.
1165 Spandidos, A., X. Wang, H. Wang, and B. Seed. 2010. PrimerBank: a resource of human and
1166 mouse PCR primer pairs for gene expression detection and quantification. *Nucleic Acids*
1167 *Res*. 38:D792-799.
1168 Stolarz, A.J., M. Sarimollaoglu, J.C. Marecki, T.W. Fletcher, E.I. Galanzha, S.W. Rhee, V.P.
1169 Zharov, V.S. Klimberg, and N.J. Rusch. 2019. Doxorubicin Activates Ryanodine
1170 Receptors in Rat Lymphatic Muscle Cells to Attenuate Rhythmic Contractions and
1171 Lymph Flow. *J Pharmacol Exp Ther*. 371:278-289.
1172 To, K.H.T., P. Gui, M. Li, S.D. Zawieja, J.A. Castorena-Gonzalez, and M.J. Davis. 2020. T-type,
1173 but not L-type, voltage-gated calcium channels are dispensable for lymphatic pacemaking
1174 and spontaneous contractions. *Sci Rep*. 10:70.
1175 Toland, H.M., K.D. McCloskey, K.D. Thornbury, N.G. McHale, and M.A. Hollywood. 2000.
1176 Ca(2+)-activated Cl(-) current in sheep lymphatic smooth muscle. *Am J Physiol Cell*
1177 *Physiol*. 279:C1327-1335.
1178 Torihashi, S., S.M. Ward, S. Nishikawa, K. Nishi, S. Kobayashi, and K.M. Sanders. 1995. c-kit-
1179 dependent development of interstitial cells and electrical activity in the murine
1180 gastrointestinal tract. *Cell Tissue Res*. 280:97-111.
1181 Truett, G.E., P. Heeger, R.L. Mynatt, A.A. Truett, J.A. Walker, and M.L. Warman. 2000.
1182 Preparation of PCR-quality mouse genomic DNA with hot sodium hydroxide and tris
1183 (HotSHOT). *Biotechniques*. 29:52, 54.
1184 Van Helden, D.A., P.Y. Von Der Weid, and M. Crowe. 1996. Intracellular Ca Release: A basis
1185 for electrical pacemaking in lymphatic smooth muscle. *In* Smooth muscle excitation. T.B.
1186 Ed. Bolton and T. Tomita, editors. London: Academic Press. 355–373.

1187 Van Helden, D.F. 1993. Pacemaker potentials in lymphatic smooth muscle of the guinea-pig
1188 mesentery. *J Physiol*. 471:465-479.
1189 van Helden, D.F., K. Hosaka, and M.S. Imtiaz. 2006. Rhythmicity in the microcirculation. *Clin*
1190 *Hemorheol Microcirc*. 34:59-66.
1191 van Helden, D.F., and M.S. Imtiaz. 2019. Venous Vasomotion. *Adv Exp Med Biol*. 1124:313-
1192 328.
1193 Van Helden, D.F., and J. Zhao. 2000. Lymphatic vasomotion. *Clin Exp Pharmacol Physiol*.
1194 27:1014-1018.
1195 Van, S., S. Pal, B.R. Garner, K. Steed, V. Sridharan, S. Mu, N.J. Rusch, and A.J. Stolarz. 2021.
1196 Dantrolene Prevents the Lymphostasis Caused by Doxorubicin in the Rat Mesenteric
1197 Circulation. *Front Pharmacol*. 12:727526.
1198 Vannucchi, M.G., C. Traini, M. Manetti, L. Ibba-Manneschi, and M.S. Faussone-Pellegrini.
1199 2013. Telocytes express PDGFRalpha in the human gastrointestinal tract. *J Cell Mol*
1200 *Med*. 17:1099-1108.
1201 von der Weid, P.Y., M. Rahman, M.S. Imtiaz, and D.F. van Helden. 2008. Spontaneous transient
1202 depolarizations in lymphatic vessels of the guinea pig mesentery: pharmacology and
1203 implication for spontaneous contractility. *Am J Physiol Heart Circ Physiol*. 295:H1989-
1204 2000.
1205 Wang, X., and B. Seed. 2003. A PCR primer bank for quantitative gene expression analysis.
1206 *Nucleic Acids Res*. 31:e154.
1207 Wang, Y., Y. Jin, M.A. Mae, Y. Zhang, H. Ortsater, C. Betsholtz, T. Makinen, and L. Jakobsson.
1208 2017. Smooth muscle cell recruitment to lymphatic vessels requires PDGFB and impacts
1209 vessel size but not identity. *Development*. 144:3590-3601.
1210 Ward, S.M., A.J. Burns, S. Torihashi, and K.M. Sanders. 1994. Mutation of the proto-oncogene
1211 c-kit blocks development of interstitial cells and electrical rhythmicity in murine
1212 intestine. *J Physiol*. 480 (Pt 1):91-97.
1213 Warthi, G., J.L. Faulkner, J. Doja, A.R. Ghanam, P. Gao, A.C. Yang, O.J. Slivano, C.T. Barris,
1214 T.C. Kress, S.D. Zawieja, S.H. Griffin, X. Xie, A. Ashworth, C.K. Christie, W.B. Bryant,
1215 A. Kumar, M.J. Davis, X. Long, L. Gan, E.J. Belin de Chantemele, Q. Lyu, and J.M.
1216 Miano. 2022. Generation and Comparative Analysis of an Itga8-CreER (T2) Mouse with
1217 Preferential Activity in Vascular Smooth Muscle Cells. *Nat Cardiovasc Res*. 1:1084-
1218 1100.
1219 Wirth, A., Z. Benyo, M. Lukasova, B. Leutgeb, N. Wettschureck, S. Gorbey, P. Orsy, B.
1220 Horvath, C. Maser-Gluth, E. Greiner, B. Lemmer, G. Schutz, J.S. Gutkind, and S.
1221 Offermanns. 2008. G12-G13-LARG-mediated signaling in vascular smooth muscle is
1222 required for salt-induced hypertension. *Nat Med*. 14:64-68.
1223 Xiao, J., F. Wang, Z. Liu, and C. Yang. 2013. Telocytes in liver: electron microscopic and
1224 immunofluorescent evidence. *J Cell Mol Med*. 17:1537-1542.
1225 Zawieja, D.C., K.L. Davis, R. Schuster, W.M. Hinds, and H.J. Granger. 1993. Distribution,
1226 propagation, and coordination of contractile activity in lymphatics. *Am J Physiol*.
1227 264:H1283-1291.
1228 Zawieja, S.D., J.A. Castorena, P. Gui, M. Li, S.A. Bulley, J.H. Jaggar, J.R. Rock, and M.J.
1229 Davis. 2019. Ano1 mediates pressure-sensitive contraction frequency changes in mouse
1230 lymphatic collecting vessels. *J Gen Physiol*. 151:532-554.

1231 Zawieja, S.D., J.A. Castorena-Gonzalez, J. Scallan, and M.J. Davis. 2018. Differences in L-type
1232 calcium channel activity partially underlie the regional dichotomy in pumping behavior
1233 by murine peripheral and visceral lymphatic vessels. *Am J Physiol Heart Circ Physiol*.
1234 Zawieja, S.D., W. Wang, S. Chakraborty, D.C. Zawieja, and M. Muthuchamy. 2016.
1235 Macrophage alterations within the mesenteric lymphatic tissue are associated with
1236 impairment of lymphatic pump in metabolic syndrome. *Microcirculation*. 23:558-570.
1237 Zhou, Q., L. Wei, C. Zhong, S. Fu, Y. Bei, R.I. Huica, F. Wang, and J. Xiao. 2015. Cardiac
1238 telocytes are double positive for CD34/PDGFR-alpha. *J Cell Mol Med*. 19:2036-2042.
1239 Zhu, M.H., T.W. Kim, S. Ro, W. Yan, S.M. Ward, S.D. Koh, and K.M. Sanders. 2009. A
1240 Ca(2+)-activated Cl(-) conductance in interstitial cells of Cajal linked to slow wave
1241 currents and pacemaker activity. *J Physiol*. 587:4905-4918.
1242 Zhu, X., D.E. Bergles, and A. Nishiyama. 2008. NG2 cells generate both oligodendrocytes and
1243 gray matter astrocytes. *Development*. 135:145-157.
1244
1245

Table 1 Primer list for RT-PCR						
Gene	**Strand**	**Accession #**	**Sequence(5'-3')**	**Siza**	**Exon**	**Source**
Prox1	s	NM_008937	GTA AGA CAT CAC CGC GTG C	218	1	NIH Primer Tool
	as		TCA TGG TCA GGC ATC ACT GG		2	
CD11b (Itgam)	s	NM_008401	ATG GAC GCT GAT GGC AAT ACC	203	13	MGH Primer Bank ID 668048a1
	as		TCC CCA TTC ACG TCT CCC A		14	
Pdgfrα	s	NM_011058	AGA GTT ACA CGT TTG AGC TGT C	252	8	MGH Primer Bank 26349287a1
	as		GTC CCT CCA CGG TAC TCC T		10	
						-
Myh11	s	NM_013607	AAG CTG CGG CTA GAG GTC A	238	33	MGH Primer Bank ID 7305295a1
	as		CCC TCC CTT TGA TGG CTG AG		34	
CD117 (cKit)	s	NM_021099	CGC CTG CCG AAA TGT ATG ACG	162	21	(Drumm et al., 2018)
	as		GGT TCT CTG GGT TGG GGT TGC		23	
Pdgfrβ	s	NM_008809	AGC TAC ATG GCC CCT TAT GA	367	16	(Basciani et al., 2004)
	as		GGA TCC CAA AAG ACC AGA CA		19	
CD144 (VE-cadherin)	s	NM_009868	CTT CCT TAC TGC CCT CAT TGT	313	3	IDT Primer Quest
	as		CTG TTT CTC TCG GTC CAA GTT		5	
Nos3 (eNOS)	s	NM_008713	ctg cca cct gat cct aac ttg	143	22	IDT Real time primer tool
	as		cag cca aac acc aaa gtc atg		23	
Acta2 (Smooth Muscle Actin)	s	NM_007392	GAG CTA CGA ACT GCC TGA C	129	7	IDT TaqMan Mm.PT.58.16320644
	as		CTG TTA TAG GTG GTT TCG TGG A		8	
CaV 1.2 exon1b	s	NM_001159533	ATG GTC AAT GAA AAC ACG AGG ATG		1	(Cheng et al., 2007)

	as		GGA ACT GAC GGT AGA GAT GGT TGC	234	2	
CD34	as	NM_001111059	GGT ACA GGA GAA TGC AGG TC	119	2	IDT Mm.PT.58.8626728
	s	NM_133654	CGT GGT AGC AGA AGT CAA GT		1	
Cspg4 (Ng2)	as	NM_139001	CTT CAC GAT CAC CAT CCT TCC	132	5	IDT Mm.PT.58.29461721
	s		CCC GAA TCA TTG TCT GTT CCC		6	
-	-	-	-	-	-	
Vimentin	s	NM_011701	CTG TAC GAG GAG GAG ATG CG	249	1	(Li et al., 2016)
	as		AAT TTC TTC CTG CAA GGA TT		3	
Desmin	s	NM_010043	GTG GAT GCA GCC ACT CTA GC	218	3	MGH Primer Bank ID 33563250a1
	as		TTA GCC GCG ATG GTC TCA TAC		4	
CD146 (Mcam)	s	NM_023061	CCC AAA CTG GTG TGC GTC TT	220	1	MGH Primer Bank 10566955a1
	as		GGA AAA TCA GTA TCT GCC TCT CC		3	
KLF4	s	NM_010637	ATT AAT GAG GCA GCC ACC TG	400	1	(Majesky et al., 2017)
	as		GGA AGA CGA GGA TGA AGC TG		3	
Ly6a (Sca1)	s	NM_001271416	CTC TGA GGA TGG ACA CTT CT	400	2	(Majesky et al., 2017)
	as		GGT CTG CAG GAG GAC TGA GC		4	
Gli1	s	NM_01029	ATC ACC TGT TGG GGA TGC TGG AT	316	8	(Kramann et al., 2015)
	as		CGT GAA TAG GAC TTC CGA CAG		10	
CD29 (Itgb1)	s	NM_010578	TCG ATC CTG TGA CCC ATT GC	170	14	NIH Primer Tool
	as		AAC AAT TCC AGC AAC CAC GC		15	

CD105 (Endoglin)	s	NM_007932	TGA GCG TGT CTC CAT TGA CC	416	11	NIH Primer Tool
	as		GGG GCC ACG TGT GTG AGA A		15	
CD44	as	NM_009851	CAC CAT TTC CTG AGA CTT GCT	148	19	IDT Mm.PT.58.12084136
	s		TCT GAT TCT TGC CGT CTG C		18	
CD31 (Pecam1)	s	NM_008816	CTG CCA GTC CGA AAA TGG AAC	218	7	MGH Primer Bank ID 6679273a1
	as		CTT CAT CCA CTG GGG CTA TC		8	
GJC1 (Connexin 45)	s	NM_008122	GGT AAC AGG AGT TCT GGT GAA	140	2	IDT Mm.PT.58.8383900
	as		TCG AAA GAC AAT CAG CAC AGT		3	
Anoctamin 1 (TMEM16A)	s	NM_178642	ggc att tgt cat tgt ctt cca g	141	25	IDT Real time primer tool
	as		tcc tca cgc ata aac agc tc		26	
CD45 (Ptprc)	s	NM_001111316	ATG CAT CCA TCC TCG TCC AC	225	29	NIH Primer Tool
	as		TGA CTT GTC CAT TCT GGG CG		31	
MGH Harvard Primer Bank (Wang and Seed, 2003; Spandidos et al., 2008; Spandidos et al., 2010)						

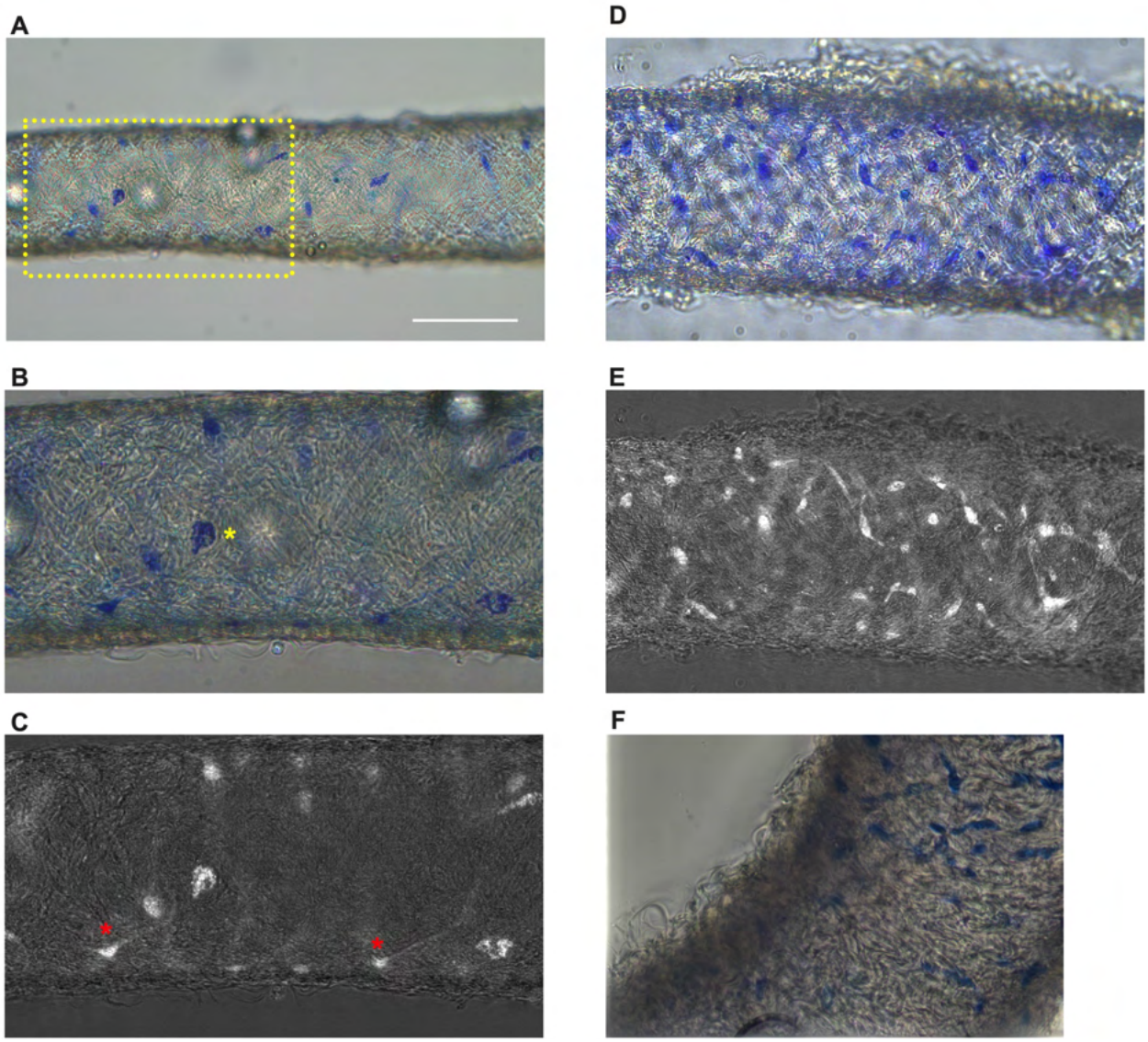

Figure 1 Methylene blue staining of isolated mouse IALVs

(A) Representative image of an isolated and cleaned IALV after methylene blue staining which revealed cells of various morphology. (B) is the zoomed in image of the yellow dotted box in A which contained large ovoid cells with granular staining (B, yellow asterisks). Fine cellular extensions (red asterisks) stained by methylene blue in some cells were visualized with color channel separation and division (C). (D, E) Similar as B and C, but in a separate vessel which stained with a higher density of methylene blue stained cells some of which had limited cellular processes. F) Focal reconstruction from imaging a methylene blue stained vessel using an upright microscope and immersion objective.

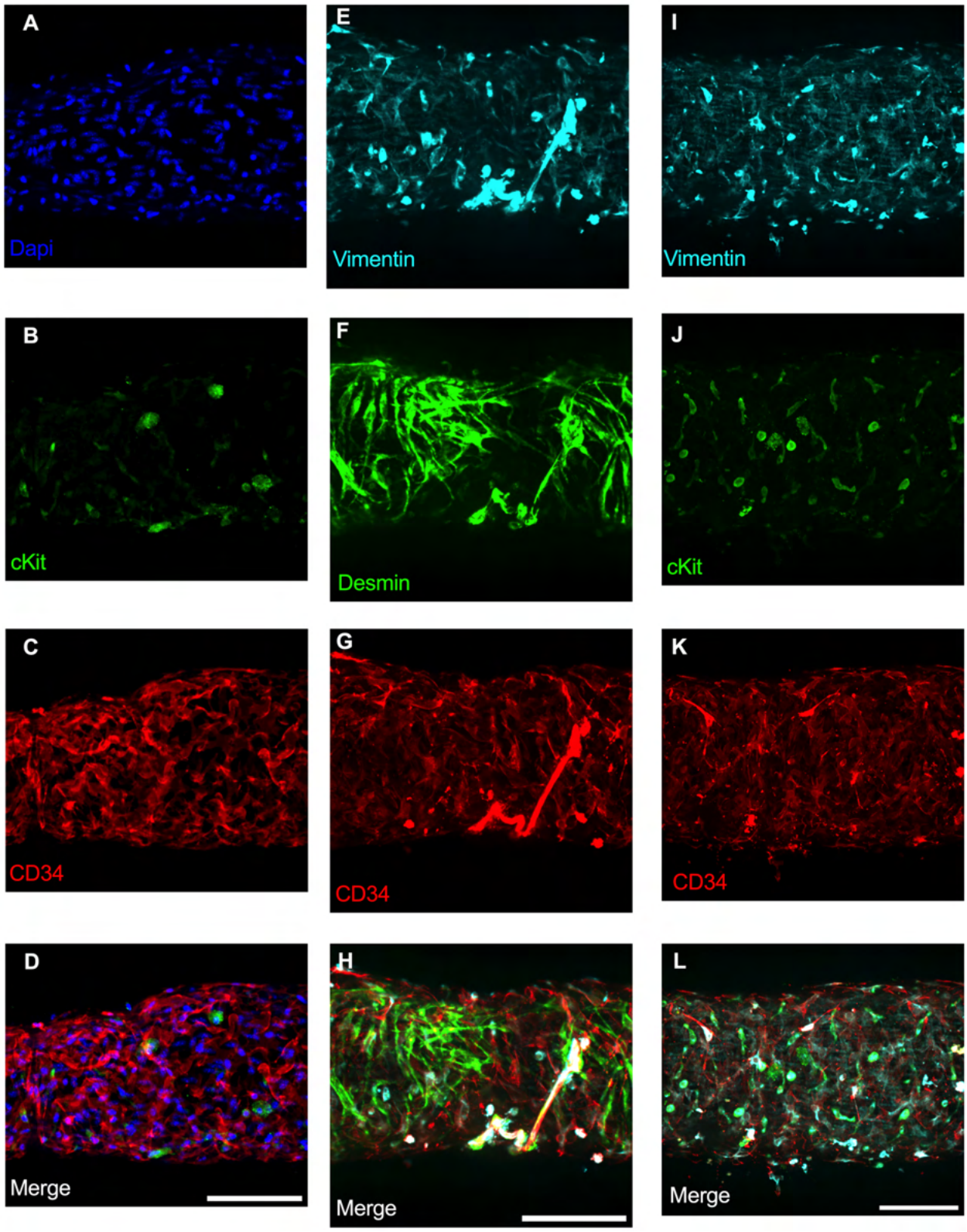

Figure 2 Staining Murine IALVs for ICLC Markers

Representative immunofluorescent max projections of half vessel confocal image stacks imaged from mouse IALVs stained for ICLC markers. DAPI (A), cKit (B), and CD34 (C) and their merged

1265 image (D). Representative max projections of the intermediate filament vimentin (E), the
1266 intermediate filament desmin (F), CD34 (G) and their merged image (H). Representative max
1267 projection of vimentin (I), cKit (J), CD34 (K) and their merged image (L). Scale bar = 100 µm for
1268 all images.
1269
1270

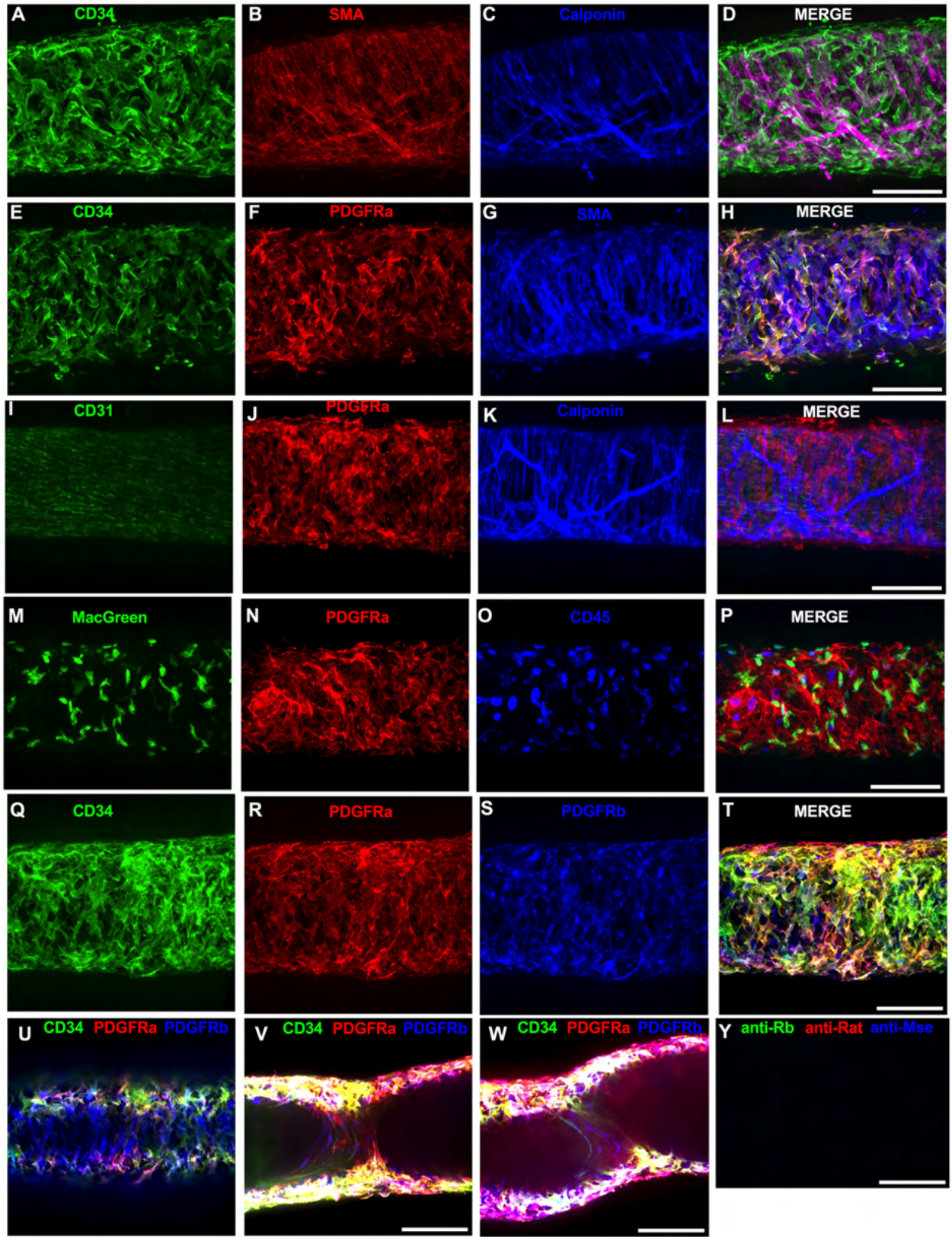

Figure 3 Immunofluorescent Labeling of Murine IALVs With Markers for ICLC, LMC, LEC, and Immune Cell Populations

1274 We stained isolated mouse IALVs with cellular markers used to differentiate various cell types
1275 observed in cLVs. Half vessel image stacks were taken with confocal microscopy and the
1276 resulting representative max projections are shown. (A) CD34 stained cells and LMC staining
1277 with SMA (B) and calponin (C) and the corresponding merged (D) image. Significant overlap in
1278 (E) CD34 staining along with the fibroblast marker PDGFRα compared to LMC staining with SMA
1279 (G) and the merged (H) image. The endothelial marker CD31 (I) to delineate LECs with PDGFRα
1280 staining (J), and the LMC marker calponin (K) with the merged image (L). Mononuclear
1281 phagocyte cells were identified by anti-GFP (M) in IALVs from MacGreen mice and counter
1282 stained with PDGFRα (N) and the hematopoietic marker CD45 (O) with (P) the merged image.
1283 PDGFRβ (S) stained many cells that were CD34 (Q) and PDGFRα (R) positive in addition to signal
1284 detected in the LMC layer (U). Max projections of only the luminal frames of a z-stack at
1285 lymphatic valve locations revealed PDGFRβ, CD34, and PDGFRα labeling in bipolar shaped cells
1286 with long extensions that traveled throughout the valve leaflets (V, W). Secondary only stained
1287 control IALV (Y). Scale bar = 100 µm for all images.
1288
1289
1290

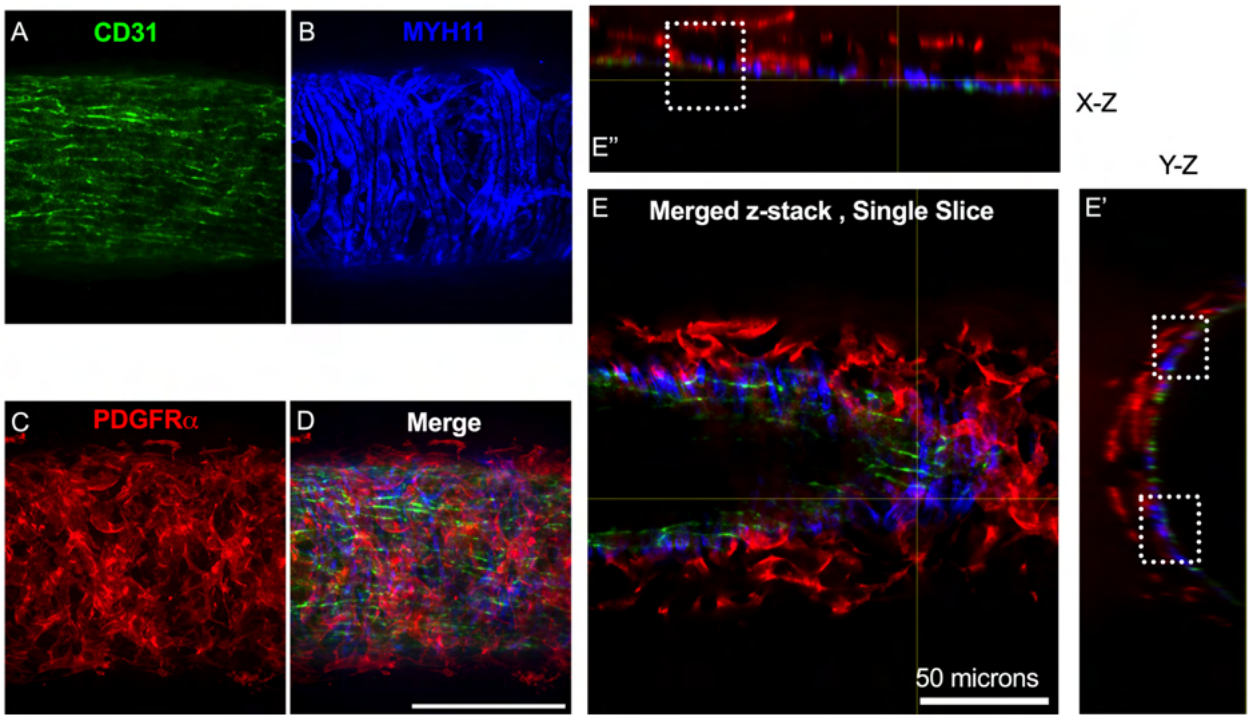

Figure 4 PDGFRα^{+} Cells Reside Primarily in the Murine Lymphatic Collecting Vessel Adventitia and Some in the Subendothelial Space

Max projection of confocal imaging of an IALV stained for LECs with CD31 (A), LMCs with MYH11(B), and for PDGFRα (C) with the corresponding merge file (D). Orthogonal views of the z-stack with (E) showing a single slice in the z stack and E' and E" the orthogonal views. White dotted boxes outline locations where PDGFRα signal is observed between LMC and LEC layers. Scale bar is 100 µm in (D) and 50 µm in (E).

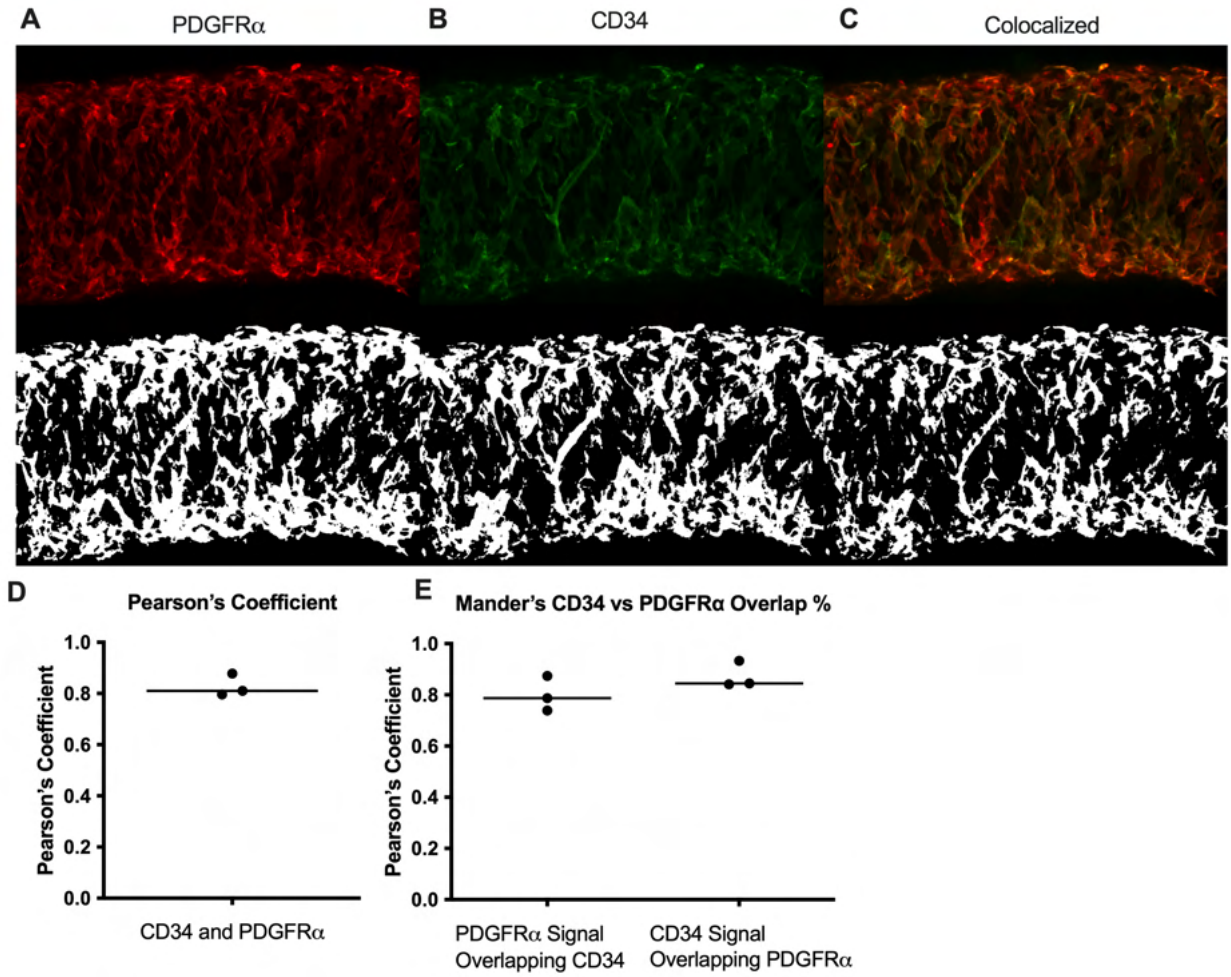

Figure 5 Colocalization of CD34 and PDGFRα

Representative max projections and their corresponding threshold adjusted images for colocalization analysis for PDGFRα (A), CD34 (B), and their colocalized signal (C). Pearson's coefficient and Mander's coefficients were calculated from 3 separate stained IALVS, each from a separate mouse.

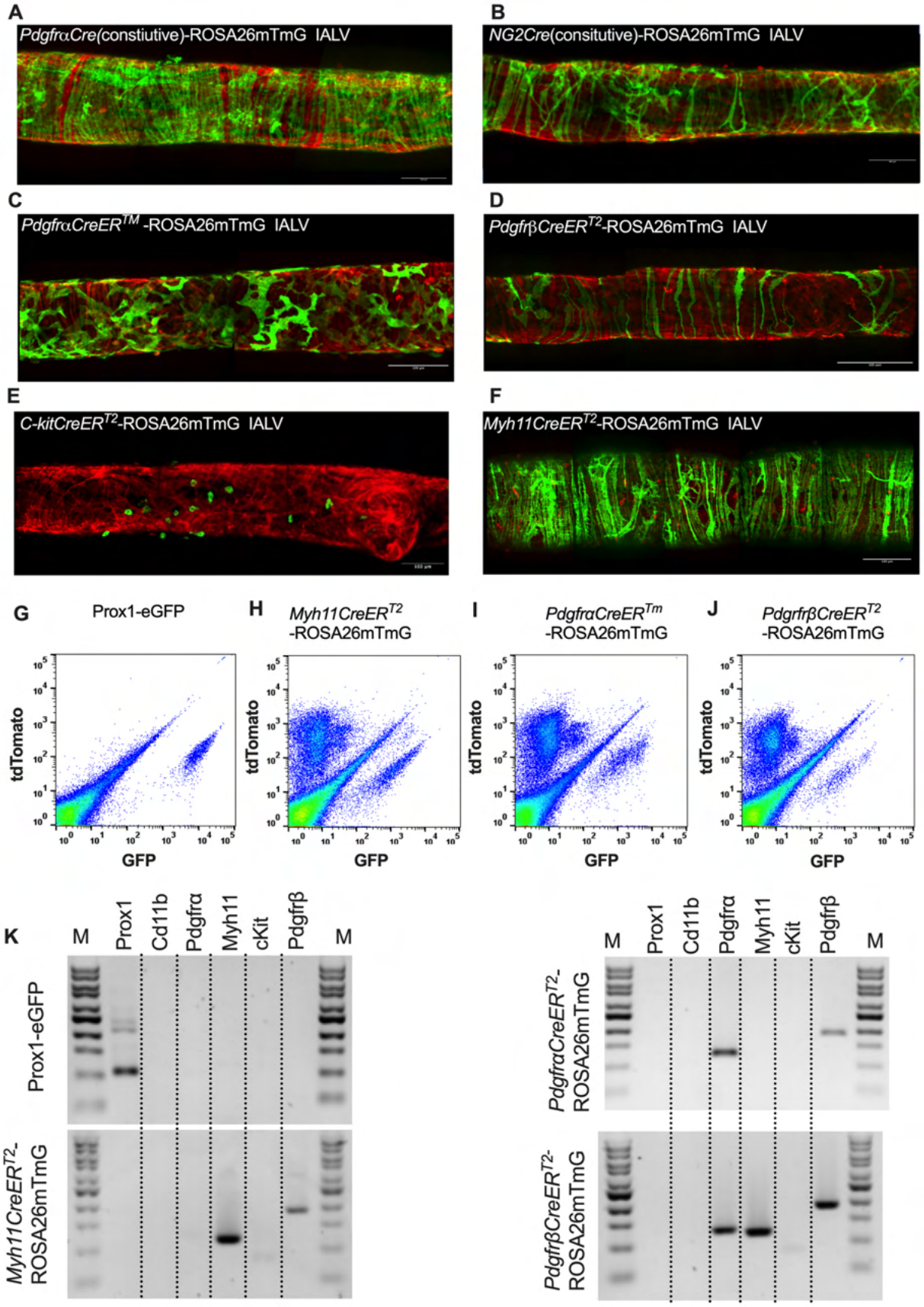
A
PdgfrαCre(constiutive)-ROSA26mTmG IALV
B
NG2Cre(consitutive)-ROSA26mTmG IALV
C
PdgfrαCreERTM -ROSA26mTmG IALV
D
PdgfrβCreERT2-ROSA26mTmG IALV
E
C-kitCreERT2-ROSA26mTmG IALV
F
Myh11CreERT2-ROSA26mTmG IALV
G
Prox1-eGFP
H
Myh11CreERT2 -ROSA26mTmG
I
PdgfraCreERTm -ROSA26mTmG
J
PdgrfrβCreERT2 -ROSA26mTmG
tdTomato
GFP
K
M
Prox1
Cd11b
Pdgfrα
Myh11
cKit
Pdgfrβ
M
Prox1-eGFP
Myh11CreERT2-ROSA26mTmG
PdgfraCreERT2-ROSA26mTmG
PdgfrβCreERT2-ROSA26mTmG

1309

1310 **Figure 6 iCre-ROSA26mTmG Labelling and Fidelity to Target Putative Pacemaker Cell Populations**
1311 Stitched montages of serial max projections of GFP and tdTomato signal from live IALVs isolated
1312 from *PdgfrαCre*-ROSA26mTmG (A), *Ng2Cre*-ROSA26mTmG (B), *PdgfrαCreER*^{TM}-ROSA26mTmG
1313 (C), *PdgfrβCreER*^{T2}-ROSA26mTmG (D), *cKitCreER*^{T2}-ROSA26mTmG (E), and *Myh11CreER*^{T2}-
1314 ROSA26mTmG (F). IALVs were digested into single cells and GFP^{+} cells were purified via FACS
1315 from *Prox1-eGFP* (G), *Myh11CreER*^{T2}-ROSA26mTmG (H), *PdgfrαCreER*^{TM}-ROSA26mTmG (I), and
1316 *PdgfrβCreER*^{T2}-ROSA26mTmG (J) mice. Representative gels demonstrating RT-PCR products
1317 corresponding to the respective gene used in the promoter of the transgenes to drive GFP
1318 signal or Cre mediated recombination of ROSA26mTmG from each GFP^{+} sorted population (K)
1319 to assess fidelity. Images are representative of IALVs from at least 3 separate mice. FACs and
1320 RT-PCR was repeated at least 3 times for each mouse.
1321
1322

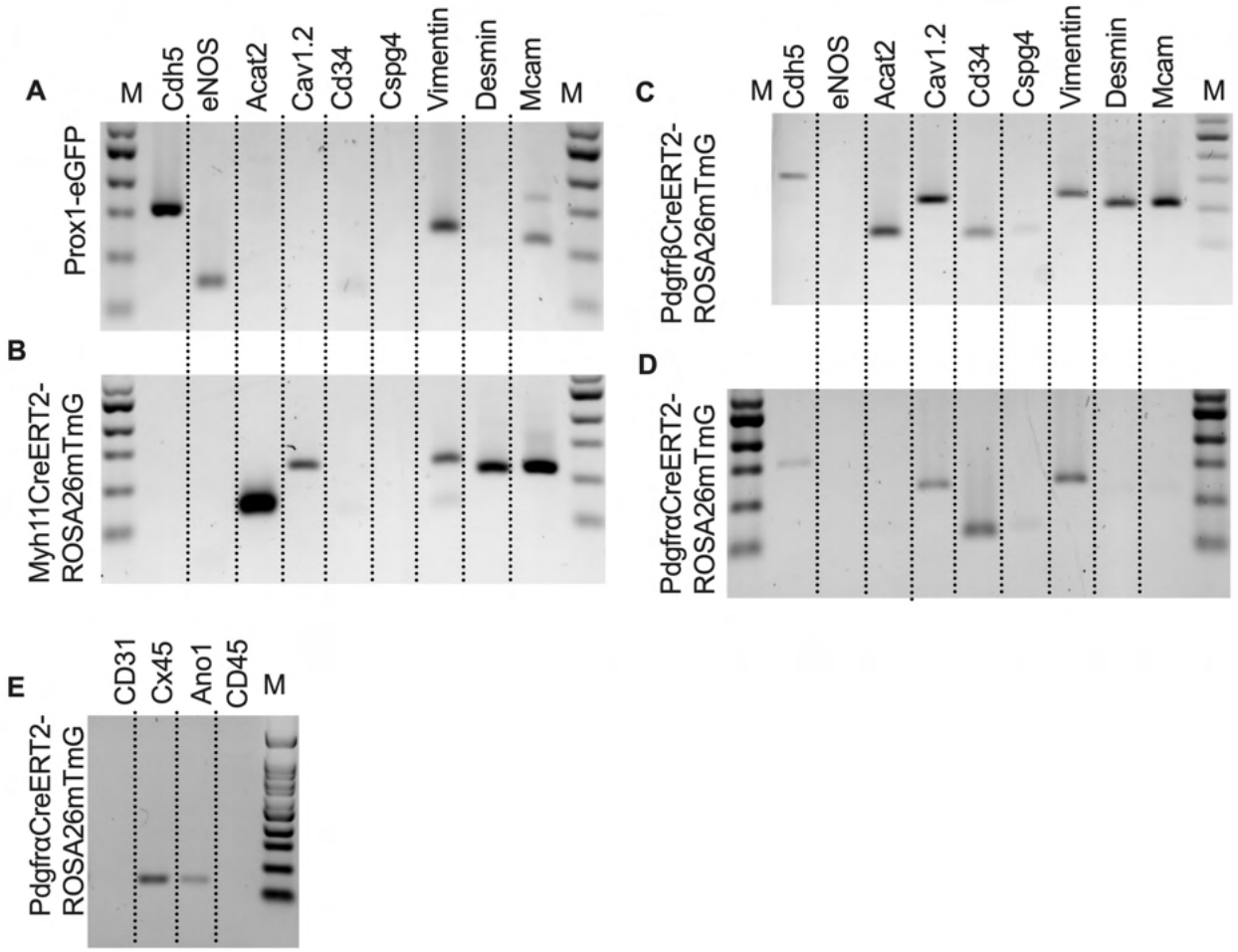

Figure 7 RT-PCR Profiling of FACs Sorted Cells from iCre-ROSA26mTmG

Expanded RT-PCR profiling of genes to discriminate LECs, LMCs, and other cell types in our GFP$^+$ sorted cells from *Prox1-eGFP* (A), *Myh11CreER^{T2}*-ROSA26mTmG (B), *PdgfrβCreER^{T2}*-ROSA26mTmG (C), and *PdgfrαCreER^{TM}*-ROSA26mTmG (D). RT-PCR results for CD31, Cx45, Ano1, and CD45 in GFP$^+$ cells sorted from *PdgfrαCreER^{TM}*-ROSA26mTmG IALVs. RT-PCR was repeated at 2-4 times for each gene over each sorted cell population collected from different mice.

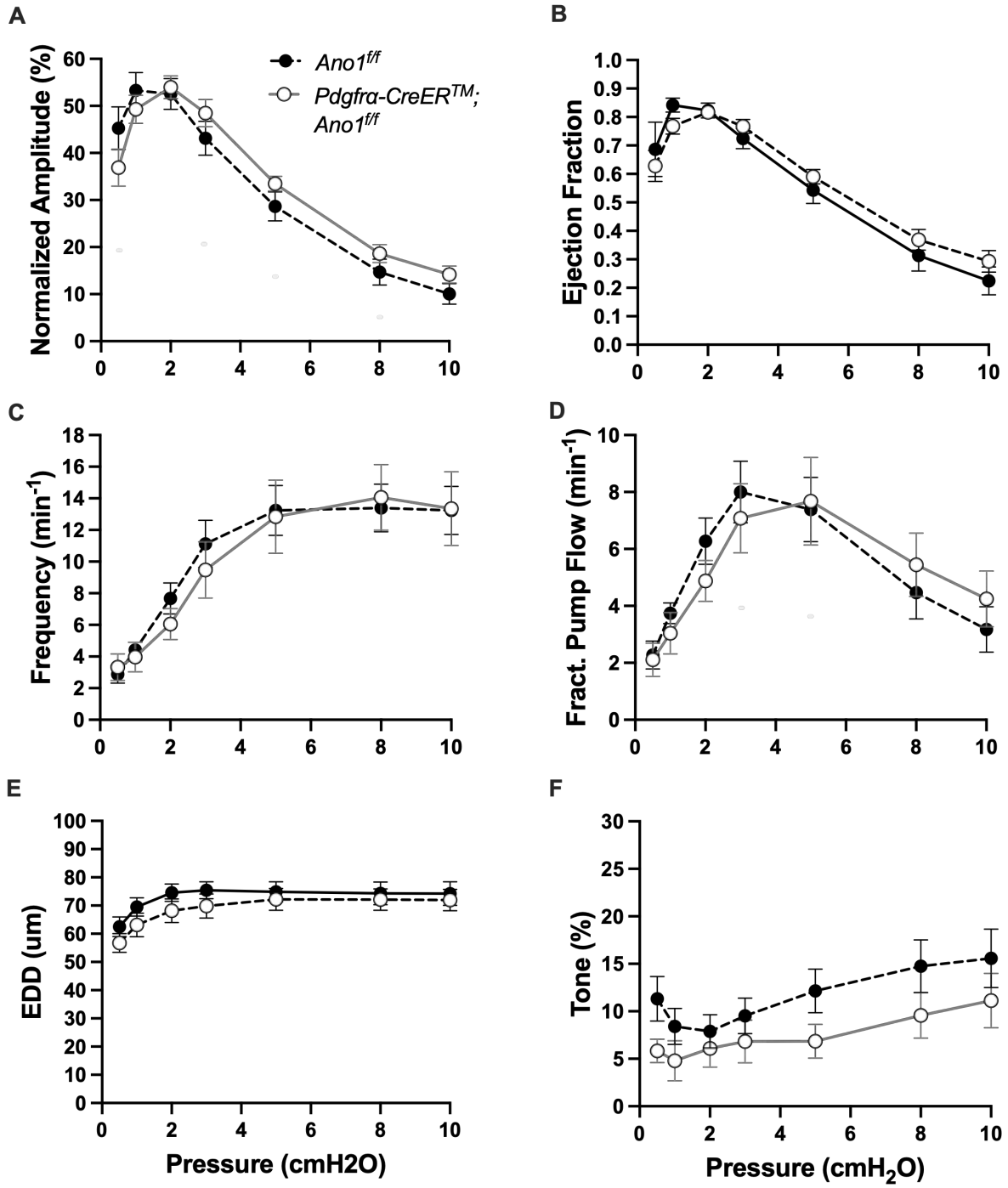

1332
1333 **Figure 8 Isobaric contractile Assessment of popliteal cLV from *PdgfrαCre*TM-Ano1 fl/fl mice**
1334 Summary of the contractile parameters recorded from popliteal cLVs in *PdgfrαCreER*^{TM}-
1335 Ano1fl/fl mice. Normalized contraction amplitude (A), ejection fraction (B), contraction
1336 frequency (C), fractional pump flow (D), end diastolic diameter (E), and vessel tone (F) were
1337 assessed. No statically significant differences observed. Mean and SEM shown, n=6 popliteal
1338 vessels from 3 mice *PdgfrαCreER*^{TM}-Ano1fl/fl mice and n=10 popliteal vessels from 6 mice
1339 Ano1fl/fl mice.

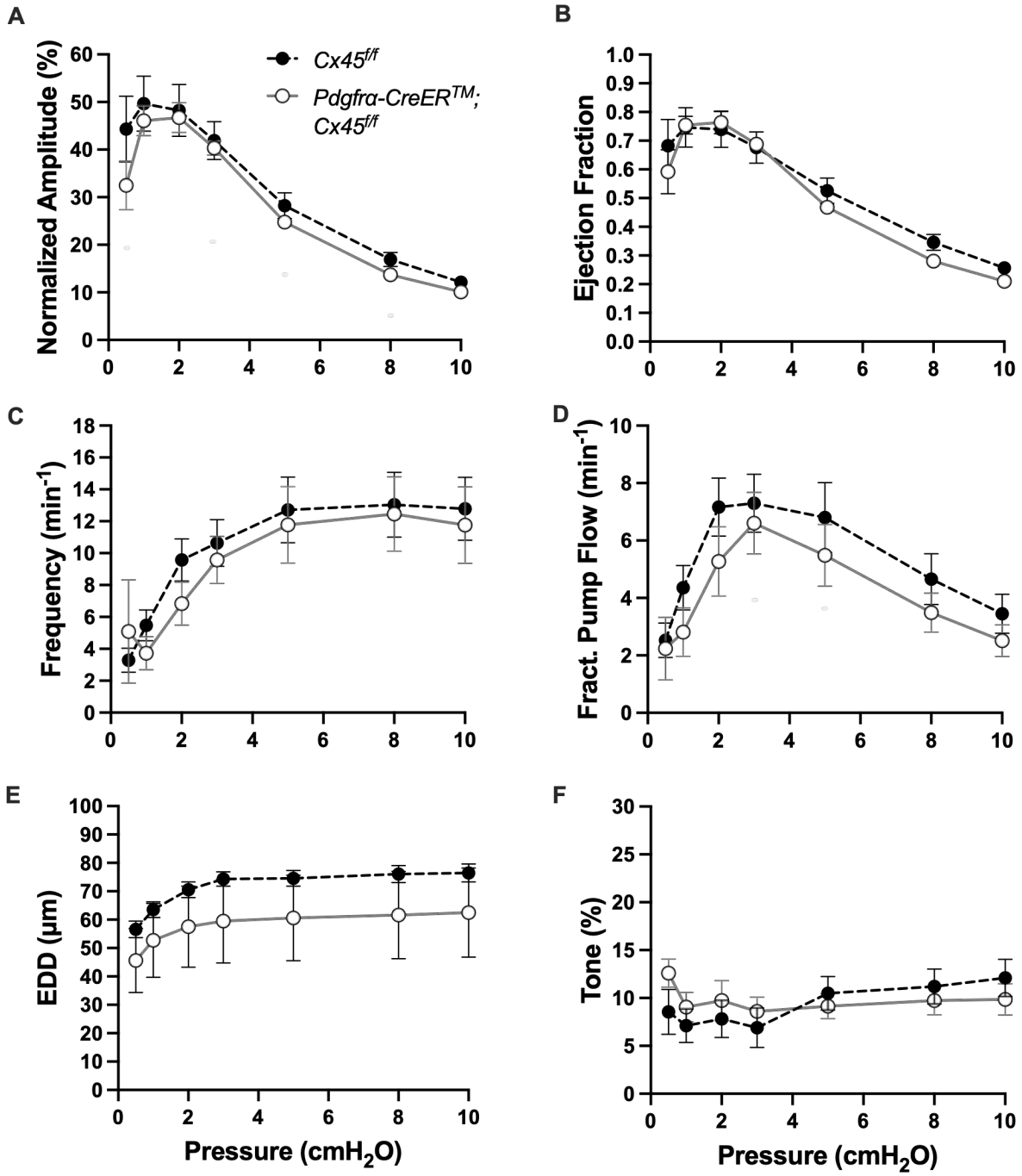

Figure 9 Isobaric contractile Assessment of popliteal cLV from *PdgfrαCre*TM-Cx45 fl/fl mice
Summary of the contractile parameters recorded from popliteal cLVs in *PdgfrαCreER*^{TM}-CX45fl/fl mice. Normalized contraction amplitude (A), ejection fraction (B), contraction frequency (C), fractional pump flow (D), end diastolic diameter (E), and vessel tone (F) were assessed. No statically significant differences observed. Mean and SEM shown, n=5 popliteal vessels from 3 mice *PdgfrαCreER*^{TM}-CX45fl/fl mice and n=8 popliteal vessels from 11 mice CX45fl/fl mice.

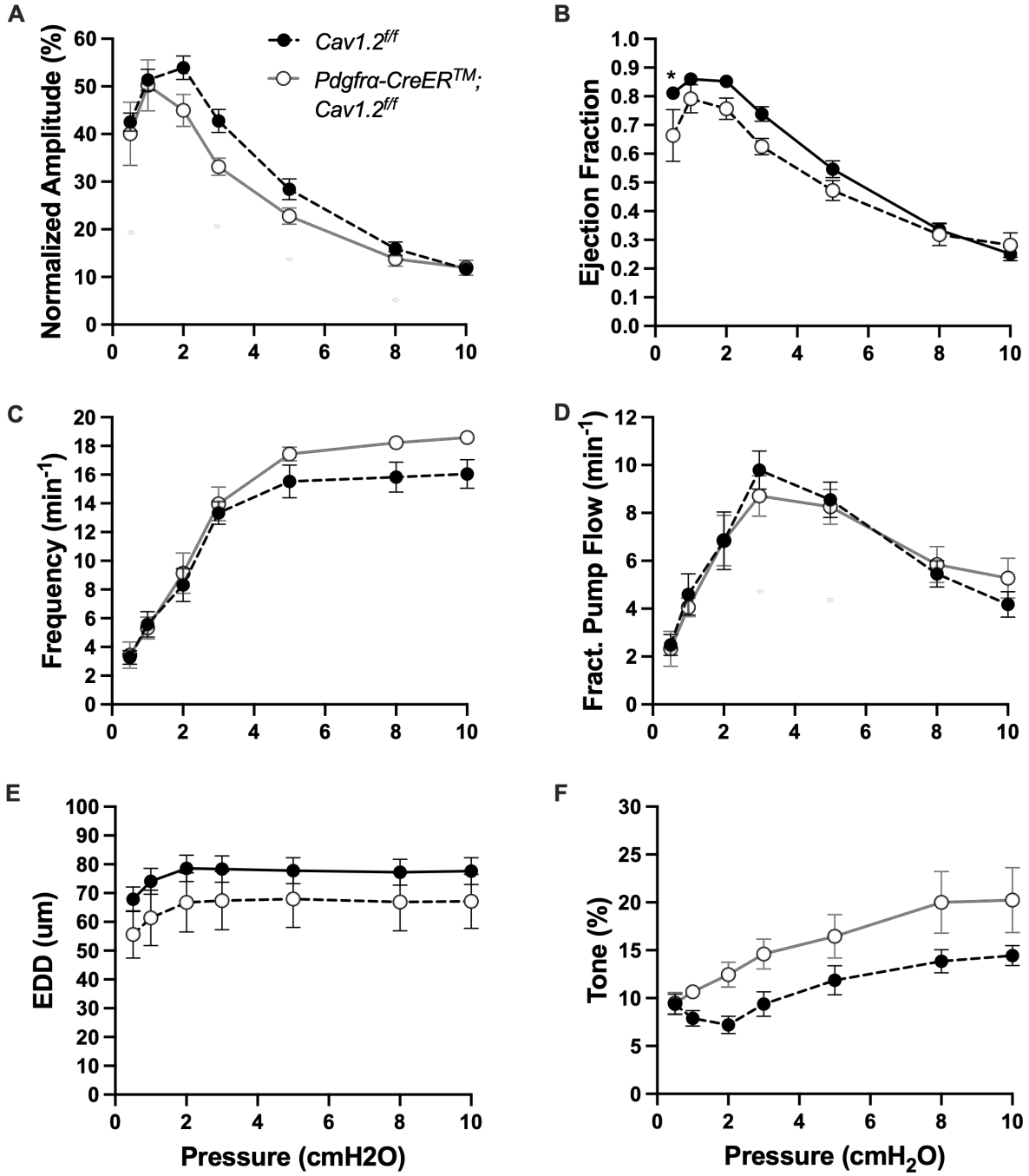

Figure 10 Isobaric contractile Assessment of popliteal cLV from *PdgfrαCre*TM-Cav1.2 fl/fl mice Summary of the contractile parameters recorded from popliteal cLVs in *PdgfrαCreER*^{TM}-Cav1.2fl/fl mice. Normalized contraction amplitude (A), ejection fraction (B), contraction frequency (C), fractional pump flow (D), end diastolic diameter (E), and vessel tone (F) were assessed. Mean and SEM shown, n=6 popliteal vessels from 3 mice *PdgfrαCreER*^{TM}-Cav1.2fl/fl mice and n=9 popliteal vessels from 20 mice Cav1.2fl/fl mice. The contractile data from control Cav1.2fl/fl vessels was previously published but was separated by sex (Davis et al., 2022) while they are combined here. * denotes significance at $p < 0.05$.

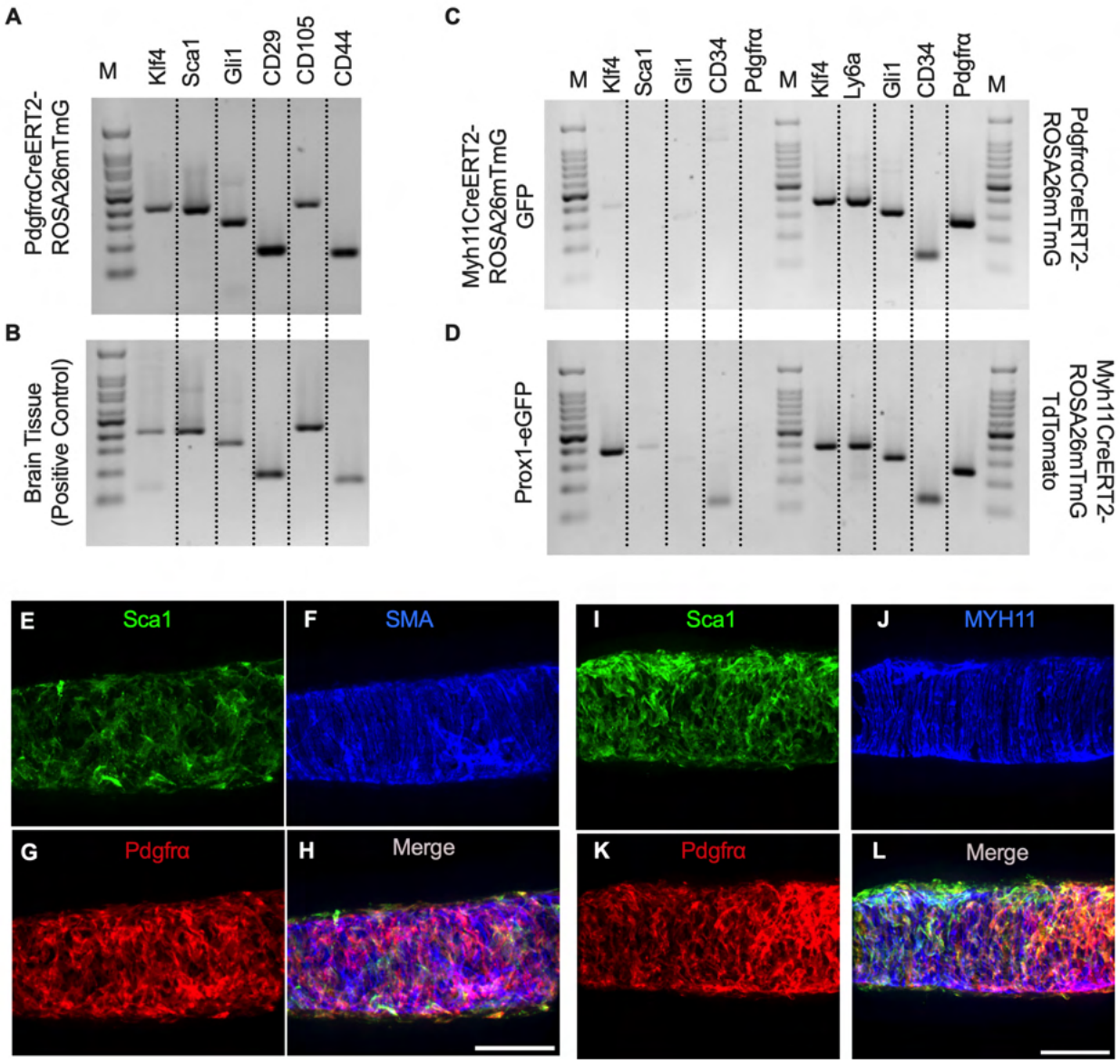

Figure 11 PDGFRα Cells Express Multipotent Cell Makers

Representative RT-PCR results profiling purified GFP+ cells purified from IALVs isolated from *PdgfrαCreER*TM-ROSA26mTmG via FACS. PDGFRα cells expressed the multipotent markers Klf4, Sca1, Gli1, CD29, CD105, and CD44 (A) with total brain cDNA serving as a positive control (B). Representative RT-PCR results showing lack of expression of some of these markers in the GFP^{+} cells purified from *Myh11CreER*^{T2}--ROSA26mTmG (C) or *Prox1-eGFP* mice, in contrast to the RFP^{+} population from *Myh11CreER*^{T2}--ROSA26mTmG mice (D). RT-PCRs were repeated at least 2 times from separate purified cells populations from different mice. Representative max projections of IALVs stained for Sca1 (E), PDGFRα (E), SMA (F) or Sca1 (I), PDGFRα (K), MYH11 (J), and their corresponding merged file (H, L). Scale bar is 100 µm.

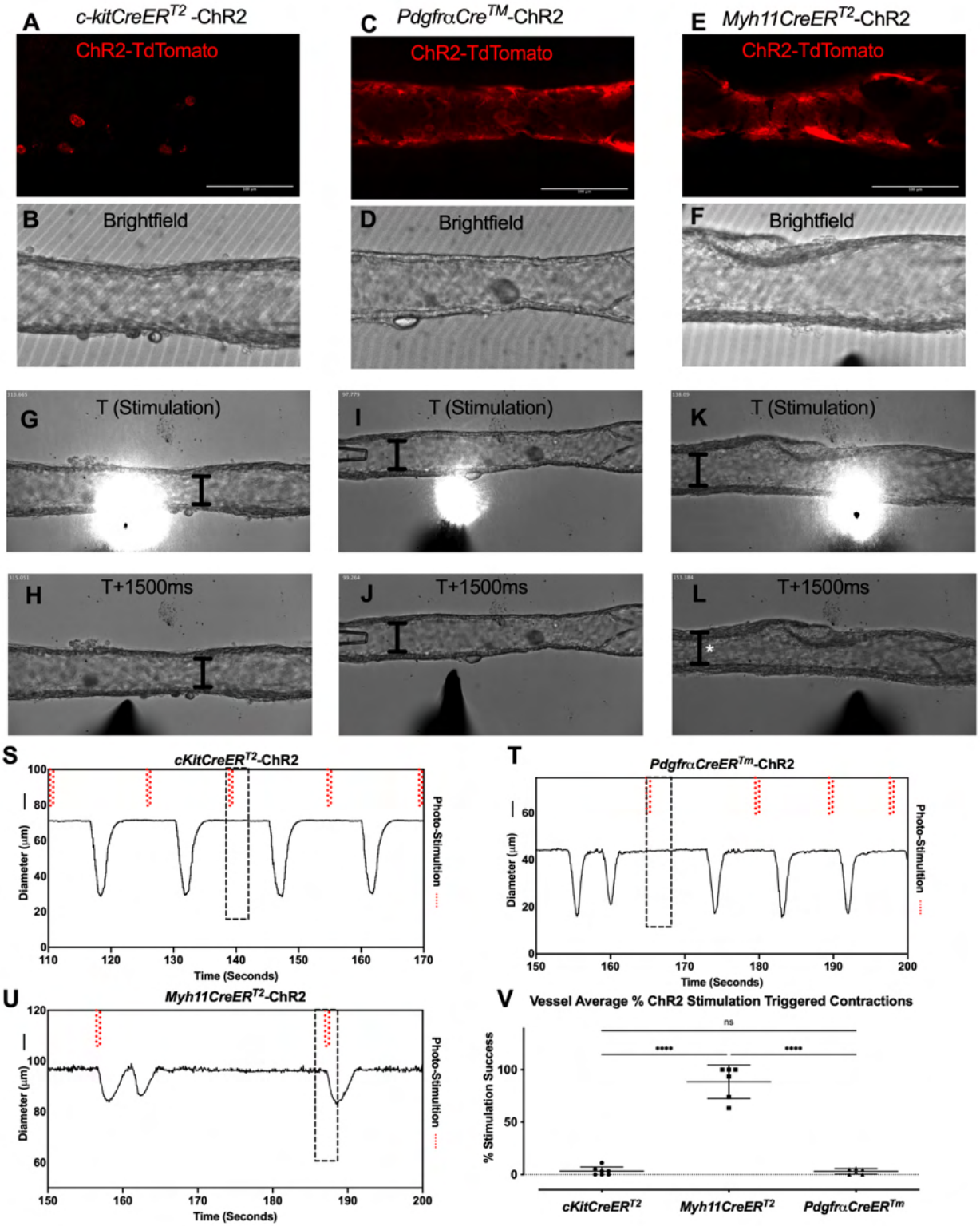

Figure 12 ChR2-Mediated Depolarization in LMCs Only Triggers Contraction
Representative max projections of tdTomato-ChR2 signal in popliteal cLVs isolated from *cKitCreER^{T2}*-ChR2-tdTomato (A), *PdgfrαCreER^{TM}*-ChR2-tdTomato (C), and *Myh11CreER^{T2}*- ChR2-tdTomato (E) with their corresponding brightfield image (B, D, F) respectively. Time-lapse

1378 brightfield images every 0.5 s starting at stimulation t=0 for *cKitCreER*^{T2}-ChR2-tdTomato (G-J),
1379 *PdgfrαCreER*^{TM}-ChR2-tdTomato (K-N), and *Myh11CreER*^{T2}- ChR2-tdTomato (O-R). The I bar
1380 denotes the inner diameter at t=0 over time and white asterisks denote the contraction.
1381 Representative diameter trace for the popliteal cLV demonstrate spontaneous contractions
1382 with the dotted boxes indicating the optical stimulation event in the respective brightfield
1383 images of the time lapse images. Isolated cLVs from *cKitCreER*^{T2}-ChR2-tdTomato (S),
1384 *PdgfrαCreER*^{TM}-ChR2-tdTomato (T), and *Myh11CreER*^{T2}- ChR2-tdTomato (U) were stimulated
1385 with light pulses (red dashed lines) and the summation of contraction triggering for each
1386 genotype (V). Mean and SEM are shown, **** denotes p<0.0001. Contraction recorded from at
1387 least 6 popliteal cLVs from 3 mice per genotype.
1388
1389

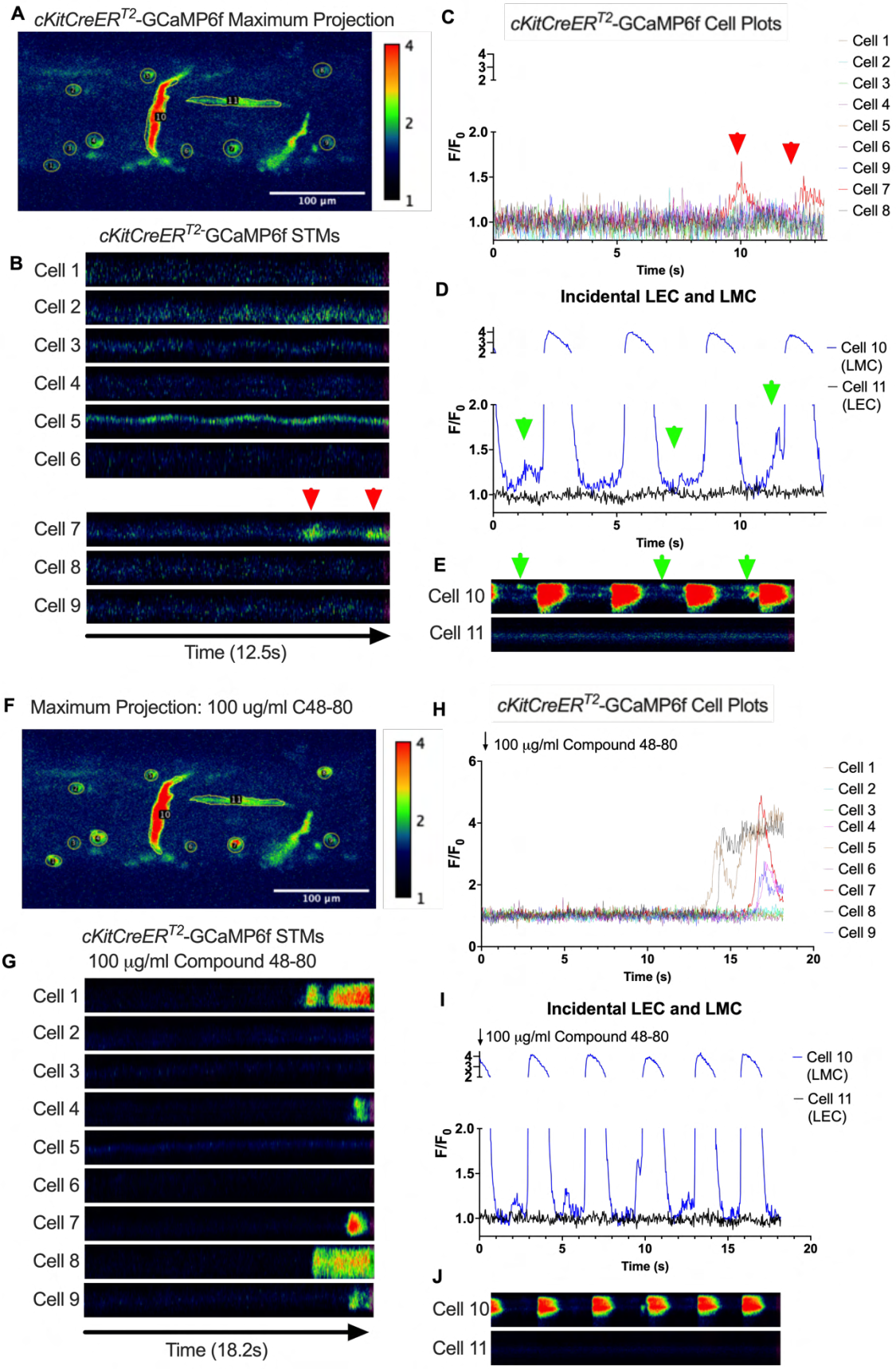
A
cKitCreER^{T2}-GCaMP6f Maximum Projection
100 µm
B
cKitCreER^{T2}-GCaMP6f STMs
Cell 1
Cell 2
Cell 3
Cell 4
Cell 5
Cell 6
Cell 7
Cell 8
Cell 9
Time (12.5s)
C
cKitCreER^{T2}-GCaMP6f Cell Plots
F/F$_0$
Time (s)
D
Incidental LEC and LMC
Cell 10 (LMC)
Cell 11 (LEC)
E
Cell 10
Cell 11
F
Maximum Projection: 100 ug/ml C48-80
100 µm
G
cKitCreER^{T2}-GCaMP6f STMs
100 µg/ml Compound 48-80
Time (18.2s)
H
cKitCreER^{T2}-GCaMP6f Cell Plots
100 µg/ml Compound 48-80
I
Incidental LEC and LMC
J

1390

1391 **Figure 13 *cKitCreER*T2 Drives GCaMP6f Expression in Primarily Mast Cells in Murine IALVs**
1392 Representative max projection of GCaMP6f signal over time in an IALV isolated from a
1393 *cKitCreER^{T2}*-GCaMP6f mouse with ROI indicated around individual cells, primarily large ovoid
1394 cells, but also including a circumferential LMC (Cell10) and a horizontal LEC (Cell 11). Of cells 1-
1395 9, only cell 7 had any Ca^{2+} activity (red arrows) during the recording time as indicated by the
1396 STMs from each ROI (B) and their normalized F/F_0 plots in (C). In contrast, the LMC in ROI 10
1397 had both rhythmic global Ca^{2+} events (D) that spanned the cell axis (vertical axis) in the STM (E)
1398 in addition to localized Ca^{2+} events intervening the time between global events (green arrows).
1399 Representative max projection of GCaMP6f signal over time after stimulation with C48-80 (F)
1400 with many large ovoid cells displaying long lasting global Ca^{2+} events (G,H) while not
1401 immediately affecting the LMC Ca^{2+} dynamics (I,J).
1402
1403

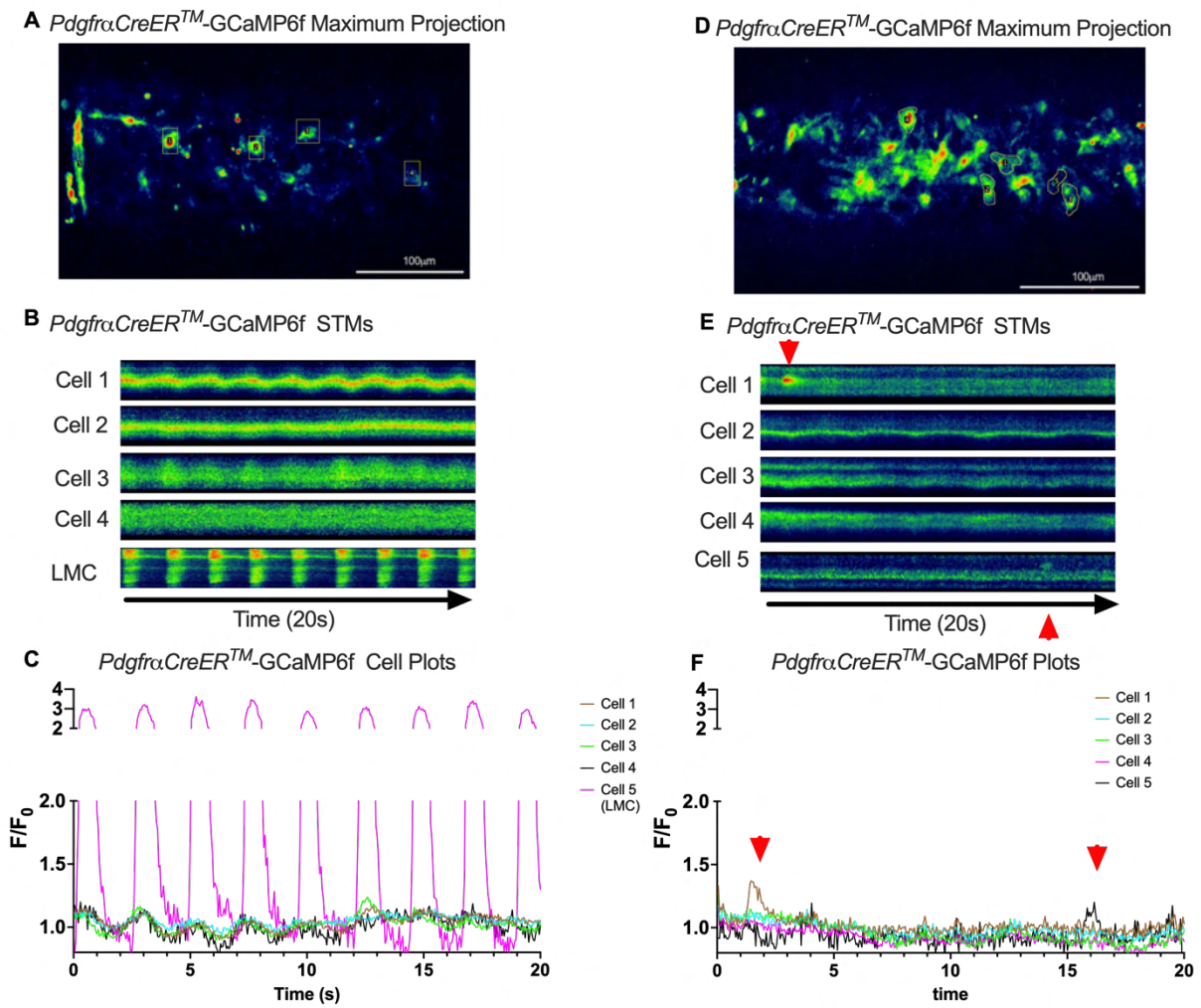

Figure 14 Lack of coordinated Ca^{2+} Activity Across Contraction Cycle in PDGFRα Cells
Representative max projections of GCaMP6f signal over time in an IALVs isolated from *PdgfrαCreER^{TM}*-GCaMP6f mice (A, D). ROIs were made around cells and GCaMP6f recorded over time to generate the corresponding STMs (B, E) for each cell and plots (C, F) respectively. Once again, incidental recombination occurred in a LMC which displayed rhythmic Ca^{2+} flashes (C) while the slight undulation in the other cells is due to movement artifact (B). Red arrows indicate the limited local Ca^{2+} activity observed in two cells from a *PdgfrαCreER^{TM}*-GCaMP6f IALV.

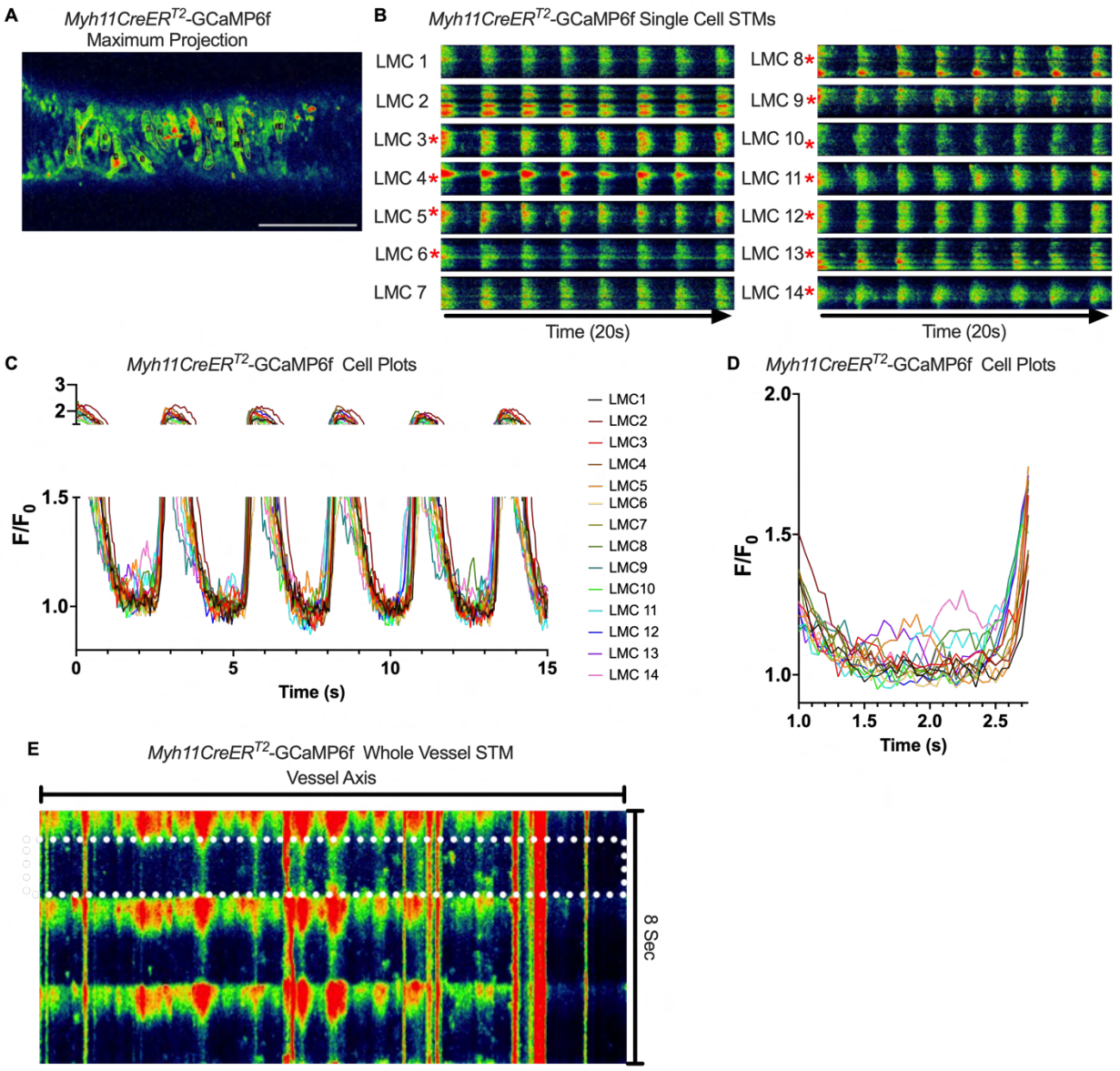

Figure 15 Heterogeneous Diastolic Ca^{2+} Transient Activity in LMCs

Representative max projections of GCaMP6f signal over time in an IALVs isolated from *Myh11CreER^{T2}*-GCaMP6f mice (A). LMCs were outlined with ROIs to assess GCaMp6F signal over time. Rhythmic global flashes (B) were entrained across all the LMCs in the FOV (C) with many cells exhibiting diastolic Ca^{2+} release events. Cells exhibiting at least one diastolic Ca^{2+} event, within the context of our focal plane constraints, over the recorded time were denoted by the red asterisks. The plot in (D) magnifies the first diastolic period, seconds 1-3, of C to assist in visualizing the lack of coordination of the diastolic events. (E) Max projection of the pseudo-linescan analysis across the axis of the vessel to highlight diastolic Ca^{2+} transients in all cells in the field of view and their lack of coordination across the cells (x-axis). The white dotted box shows the first diastolic period plotted in (D).

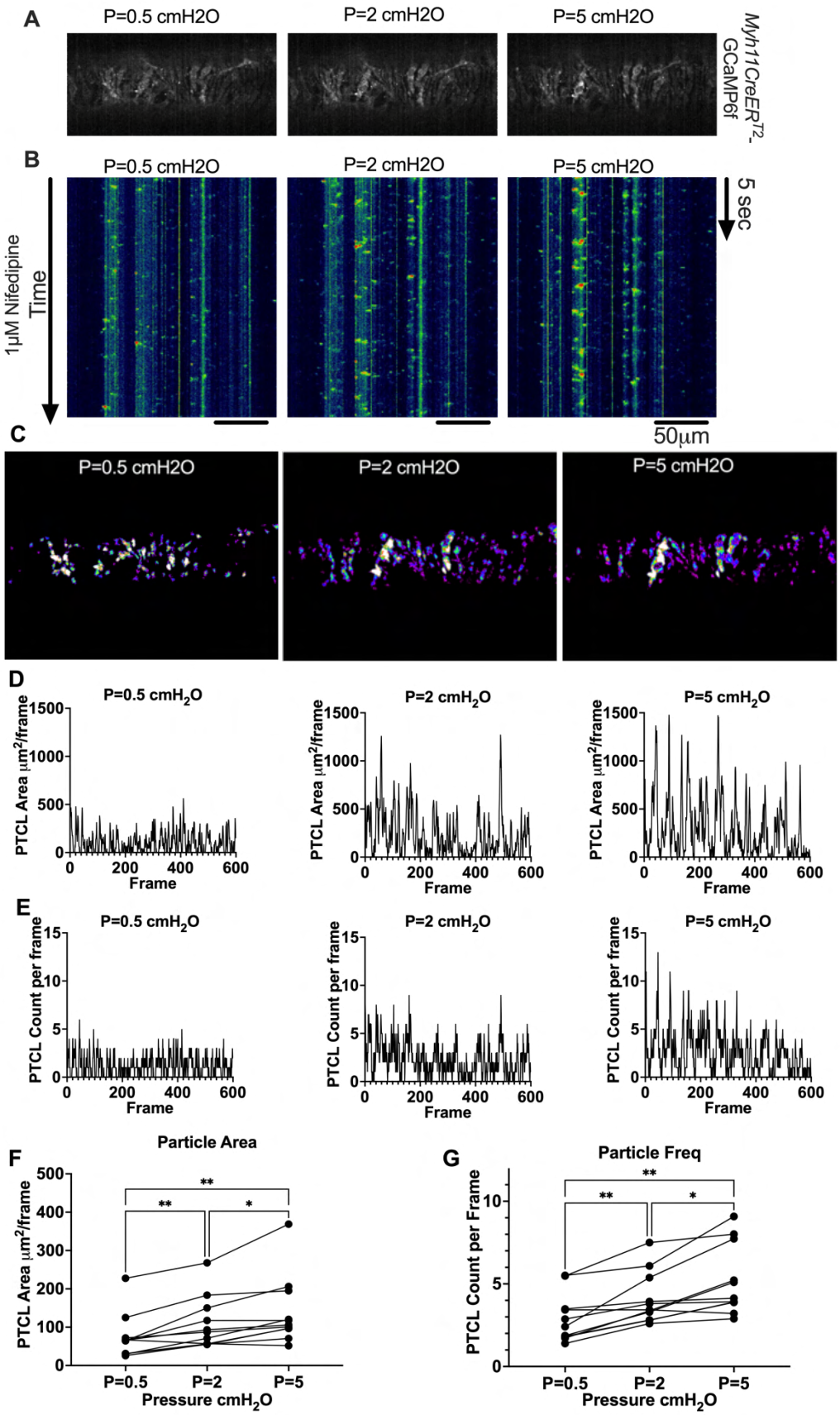
A
P=0.5 cmH2O
P=2 cmH2O
P=5 cmH2O
Myh11CreERT2-GCaMP6f
B
P=0.5 cmH2O
P=2 cmH2O
P=5 cmH2O
1μM Nifedipine
Time
5 sec
50μm
C
P=0.5 cmH2O
P=2 cmH2O
P=5 cmH2O
D
P=0.5 cmH2O
P=2 cmH2O
P=5 cmH2O
PTCL Area μm2/frame
Frame
E
P=0.5 cmH2O
P=2 cmH2O
P=5 cmH2O
PTCL Count per frame
Frame
F
Particle Area
PTCL Area μm2/frame
Pressure cmH2O
P=0.5
P=2
P=5
G
Particle Freq
PTCL Count per Frame
Pressure cmH2O
P=0.5
P=2
P=5

1429

1430 **Figure 16 Pressure Dependency of Murine LMC Diastolic Ca^{2+} Transients**
1431 Representative max projection of GCaMP6f signal over 20 s in an IALVs isolated from
1432 *Myh11CreER^{T2}*-GCaMP6f mice in the presence of the L-type blocker nifedipine (1µM) (A)
1433 pressurized to 0.5 cmH_2O, 2 cmH_2O, 5 cmH_2O. The local diastolic Ca^{2+} transients persist in the
1434 presence of nifedipine and increase with increasing pressure as demonstrated in the whole
1435 vessel STMs (B). Particle occurrence maps highlight the Ca^{2+} activity in each LMC as pressure is
1436 raised (C). Representative particle analysis plots for particle area (D) and particle counts/frame
1437 at each pressure (E). Summary files for particle area (F) and count /frame (G0. * denotes
1438 $p<0.05$, Mean and SEM shown with n=12 separate IALVs from 8 MYH11-CreER^{T2}-GCaMP6f mice.

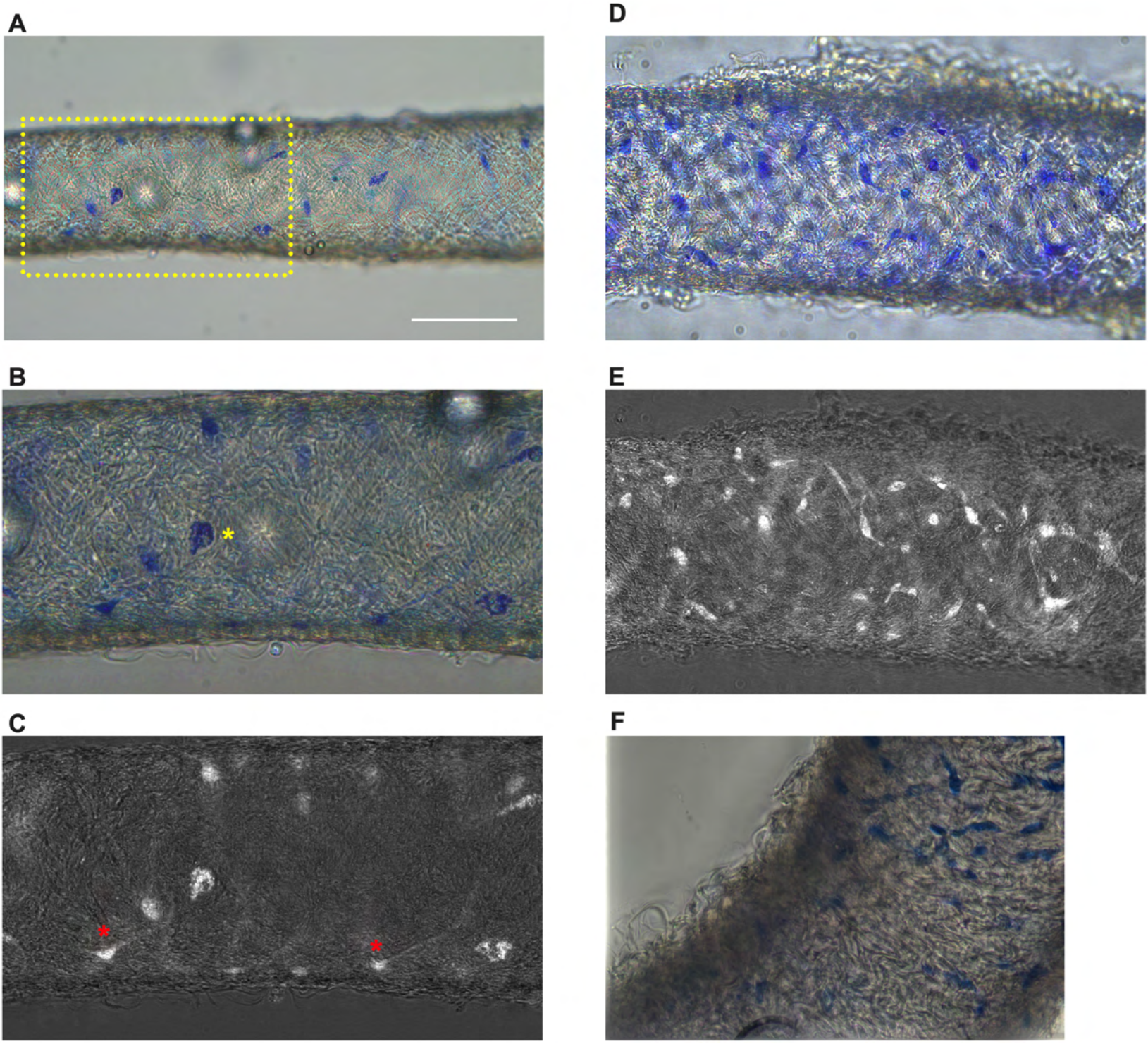
A
B
C
D
E
F

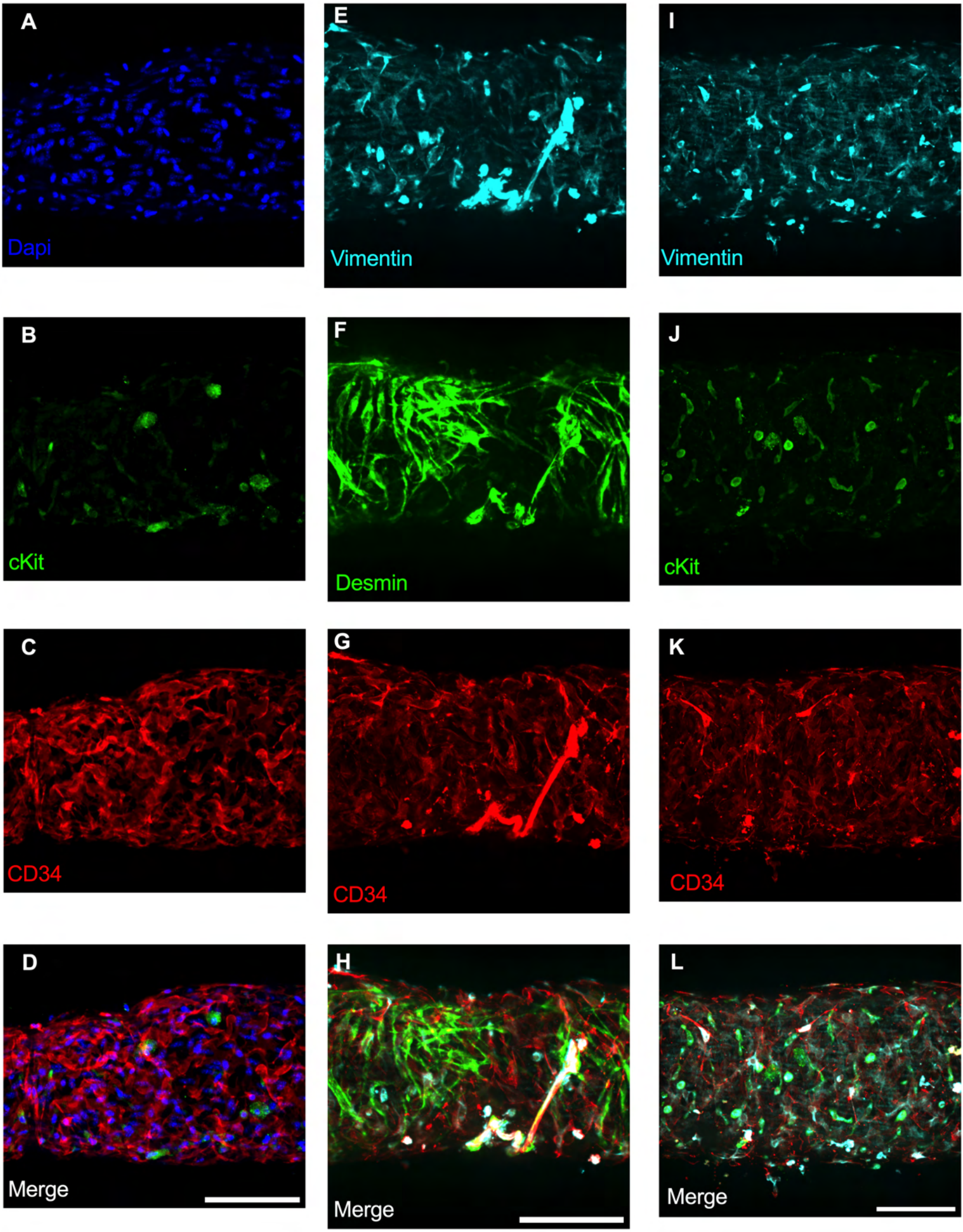
A
Dapi
E
Vimentin
I
Vimentin
B
cKit
F
Desmin
J
cKit
C
CD34
G
CD34
K
CD34
D
Merge
H
Merge
L
Merge

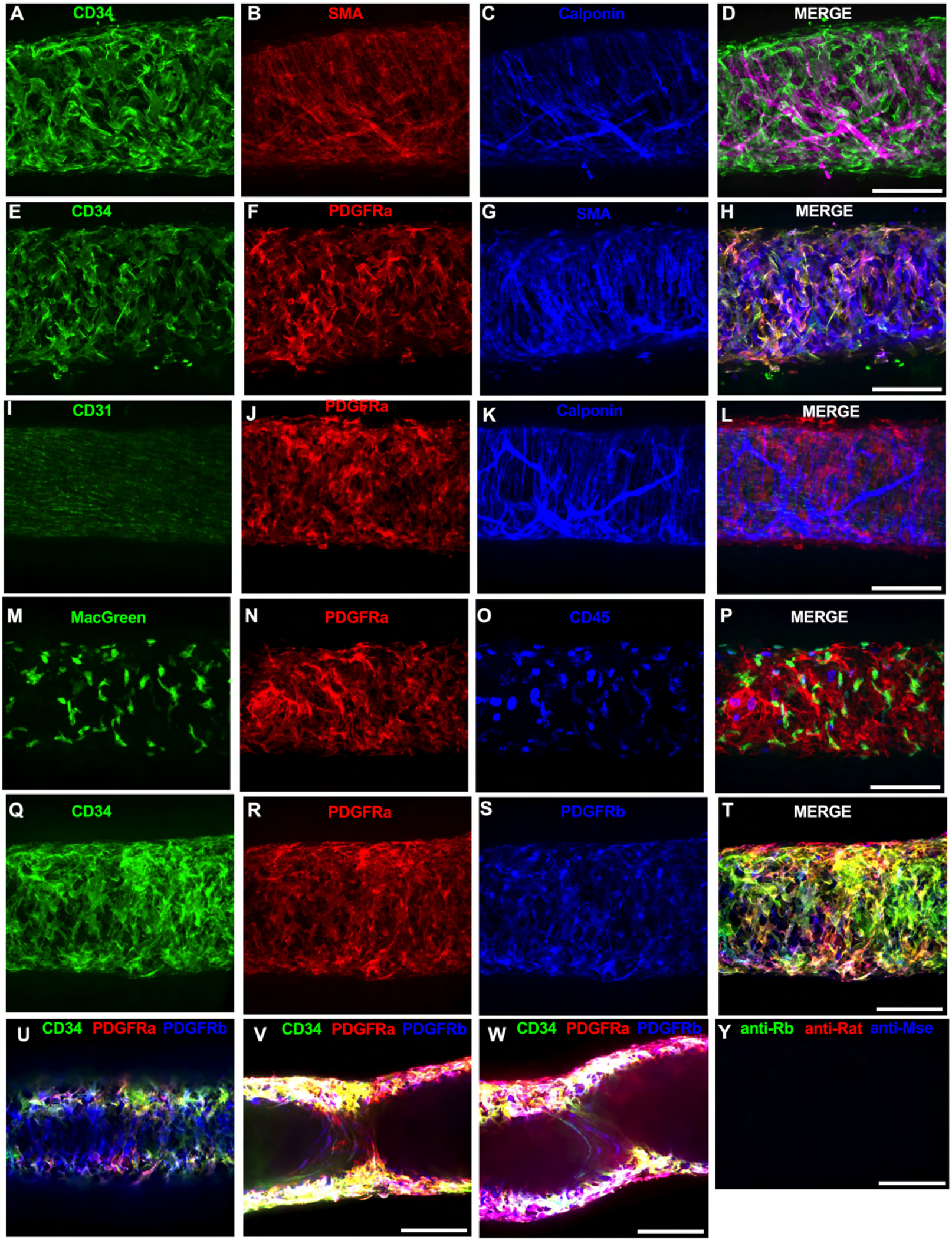
A CD34
B SMA
C Calponin
D MERGE
E CD34
F PDGFRa
G SMA
H MERGE
I CD31
J PDGFRa
K Calponin
L MERGE
M MacGreen
N PDGFRa
O CD45
P MERGE
Q CD34
R PDGFRa
S PDGFRb
T MERGE
U CD34 PDGFRa PDGFRb
V CD34 PDGFRa PDGFRb
W CD34 PDGFRa PDGFRb
Y anti-Rb anti-Rat anti-Mse

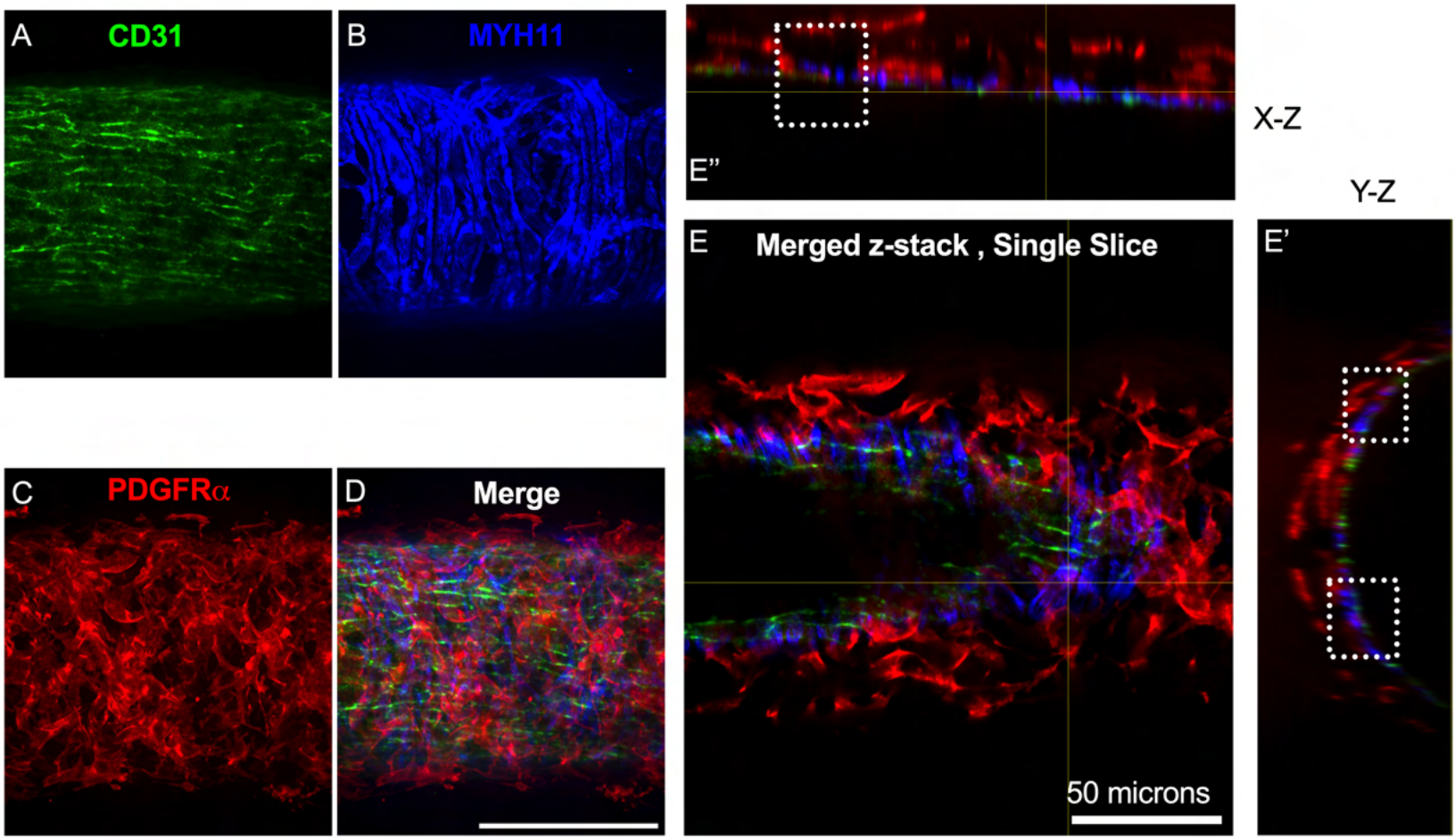
A
CD31
B
MYH11
C
PDGFRα
D
Merge
E
Merged z-stack , Single Slice
50 microns
E"
X-Z
Y-Z
E'

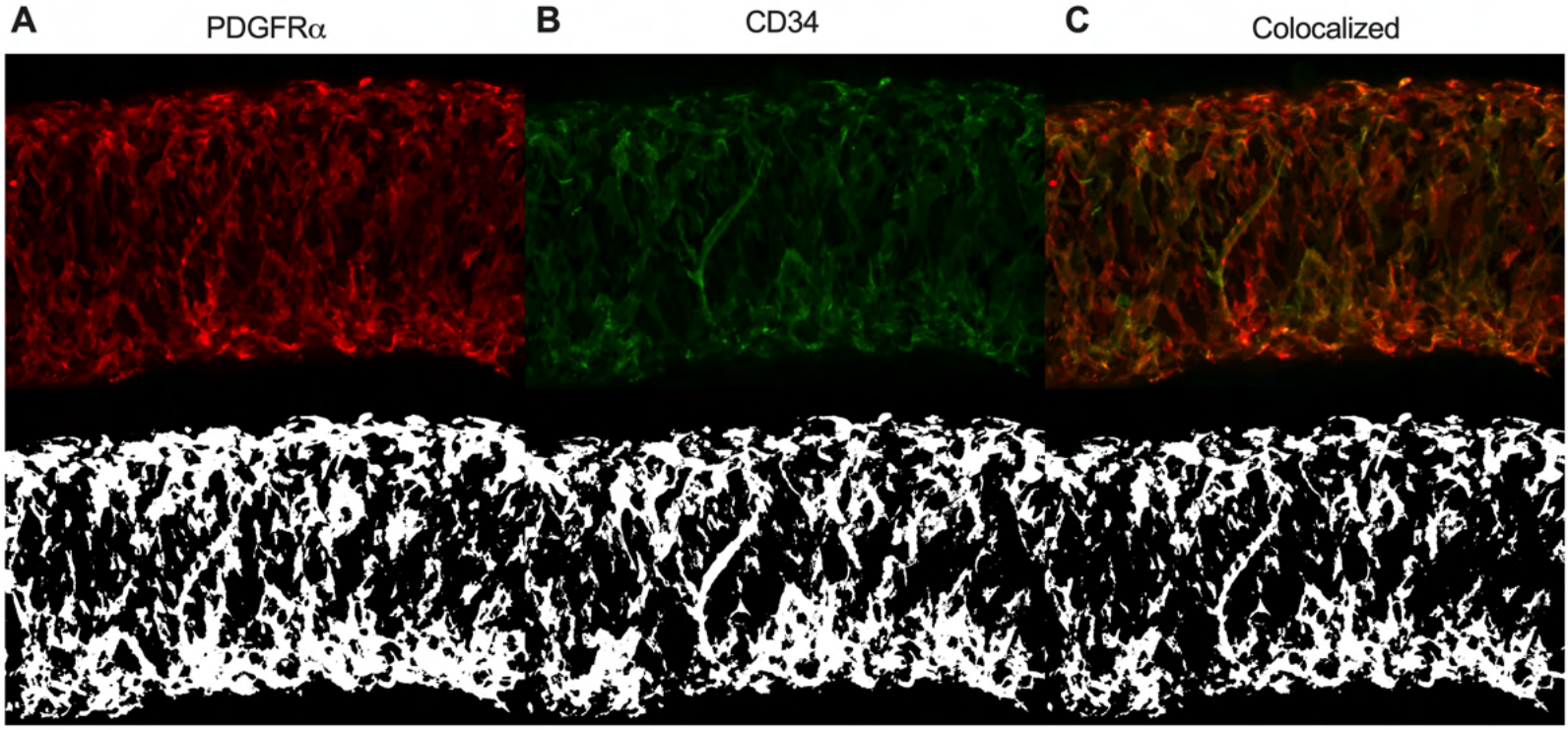
A
PDGFRα
B
CD34
C
Colocalized

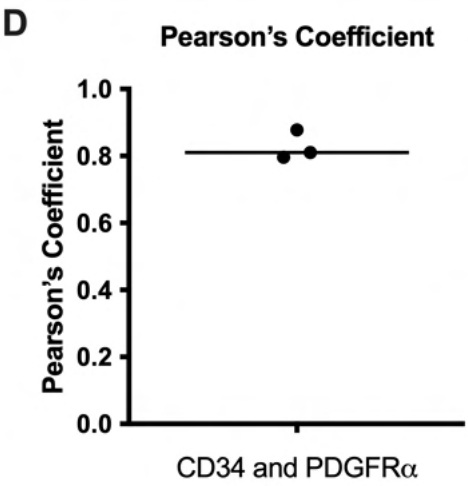
D
Pearson's Coefficient
Pearson's Coefficient
1.0
0.8
0.6
0.4
0.2
0.0
CD34 and PDGFRα

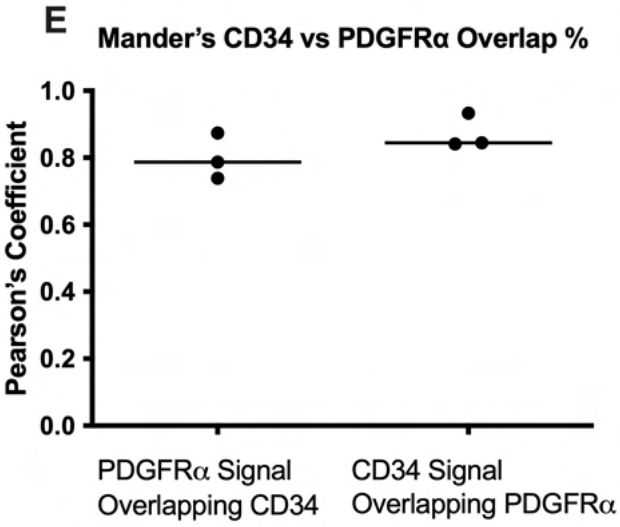
E
Mander's CD34 vs PDGFRα Overlap %
Pearson's Coefficient
1.0
0.8
0.6
0.4
0.2
0.0
PDGFRα Signal Overlapping CD34
CD34 Signal Overlapping PDGFRα

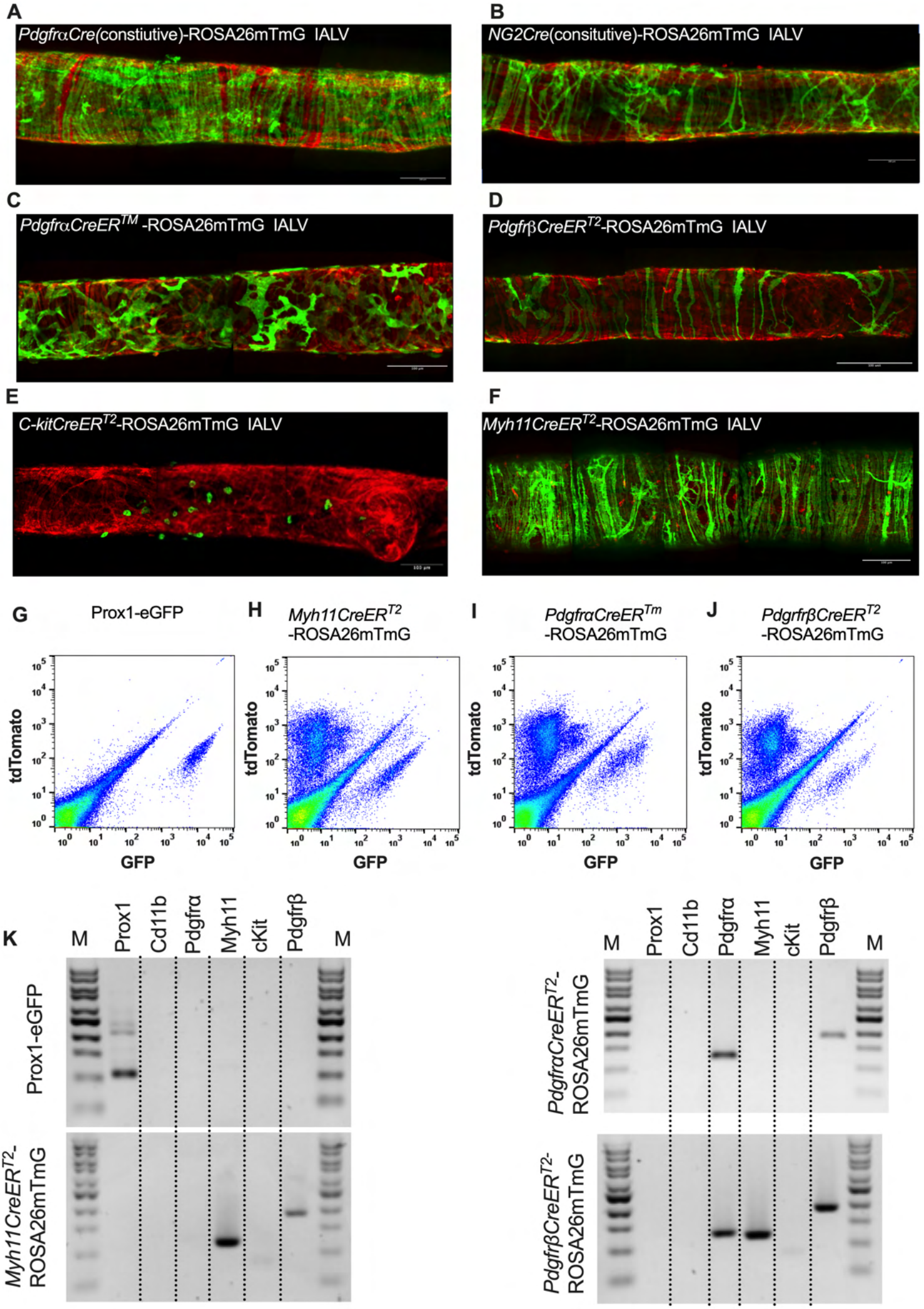
A
PdgfrαCre(constiutive)-ROSA26mTmG IALV
B
NG2Cre(consitutive)-ROSA26mTmG IALV
C
PdgfrαCreER^{TM} -ROSA26mTmG IALV
D
PdgfrβCreER^{T2}-ROSA26mTmG IALV
E
C-kitCreER^{T2}-ROSA26mTmG IALV
F
Myh11CreER^{T2}-ROSA26mTmG IALV
G
Prox1-eGFP
H
Myh11CreER^{T2} -ROSA26mTmG
I
PdgfrαCreER^{Tm} -ROSA26mTmG
J
PdgrfrβCreER^{T2} -ROSA26mTmG
tdTomato
GFP
K
M
Prox1
Cd11b
Pdgfrα
Myh11
cKit
Pdgfrβ
M
Prox1-eGFP
Myh11CreER^{T2}-ROSA26mTmG
PdgfrαCreER^{T2}-ROSA26mTmG
PdgfrβCreER^{T2}-ROSA26mTmG

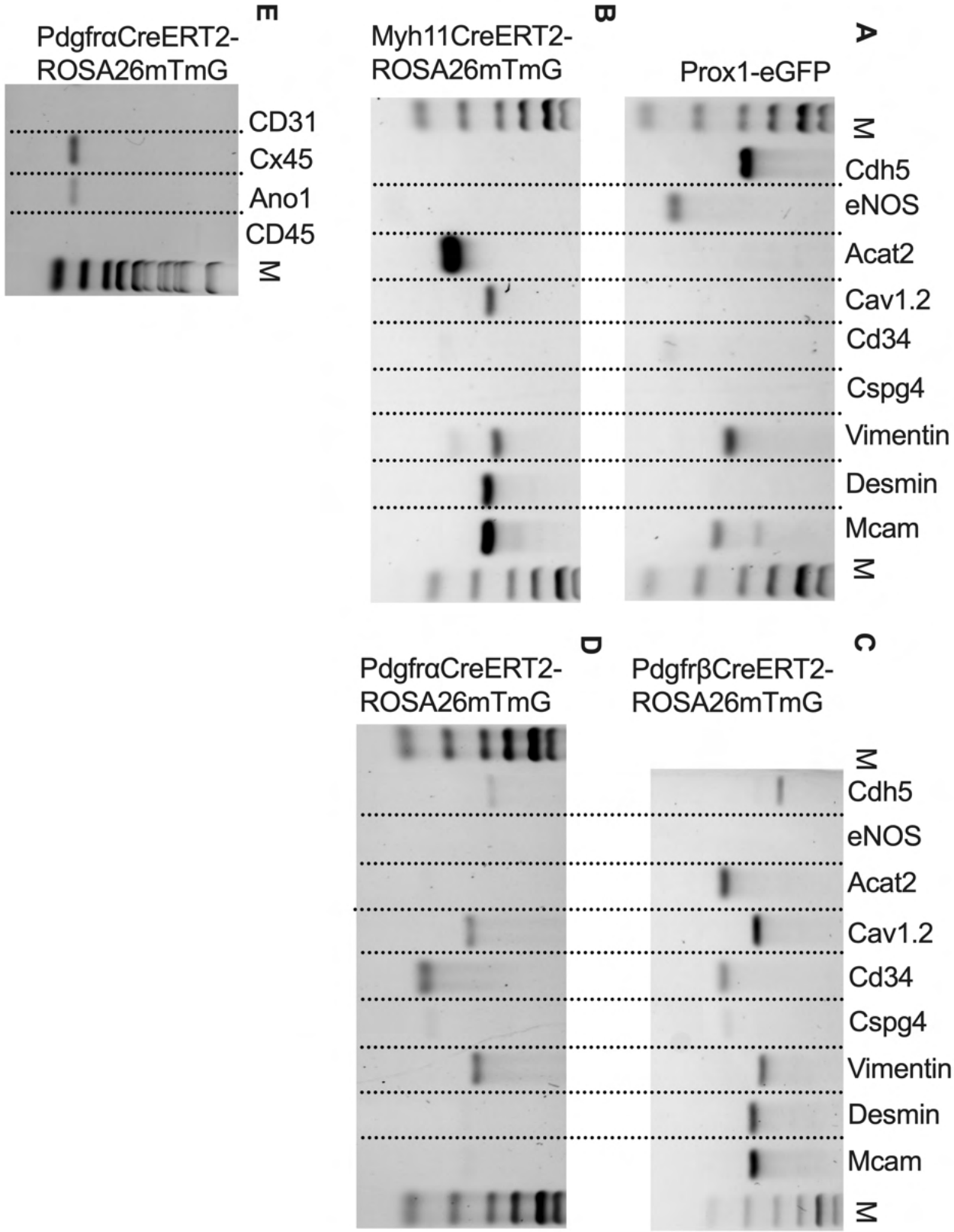
E
PdgfrαCreERT2-
ROSA26mTmG
CD31
Cx45
Ano1
CD45
M
B
Myh11CreERT2-
ROSA26mTmG
A
Prox1-eGFP
M
Cdh5
eNOS
Acat2
Cav1.2
Cd34
Cspg4
Vimentin
Desmin
Mcam
M
D
PdgfrαCreERT2-
ROSA26mTmG
C
PdgfrβCreERT2-
ROSA26mTmG
M
Cdh5
eNOS
Acat2
Cav1.2
Cd34
Cspg4
Vimentin
Desmin
Mcam
M

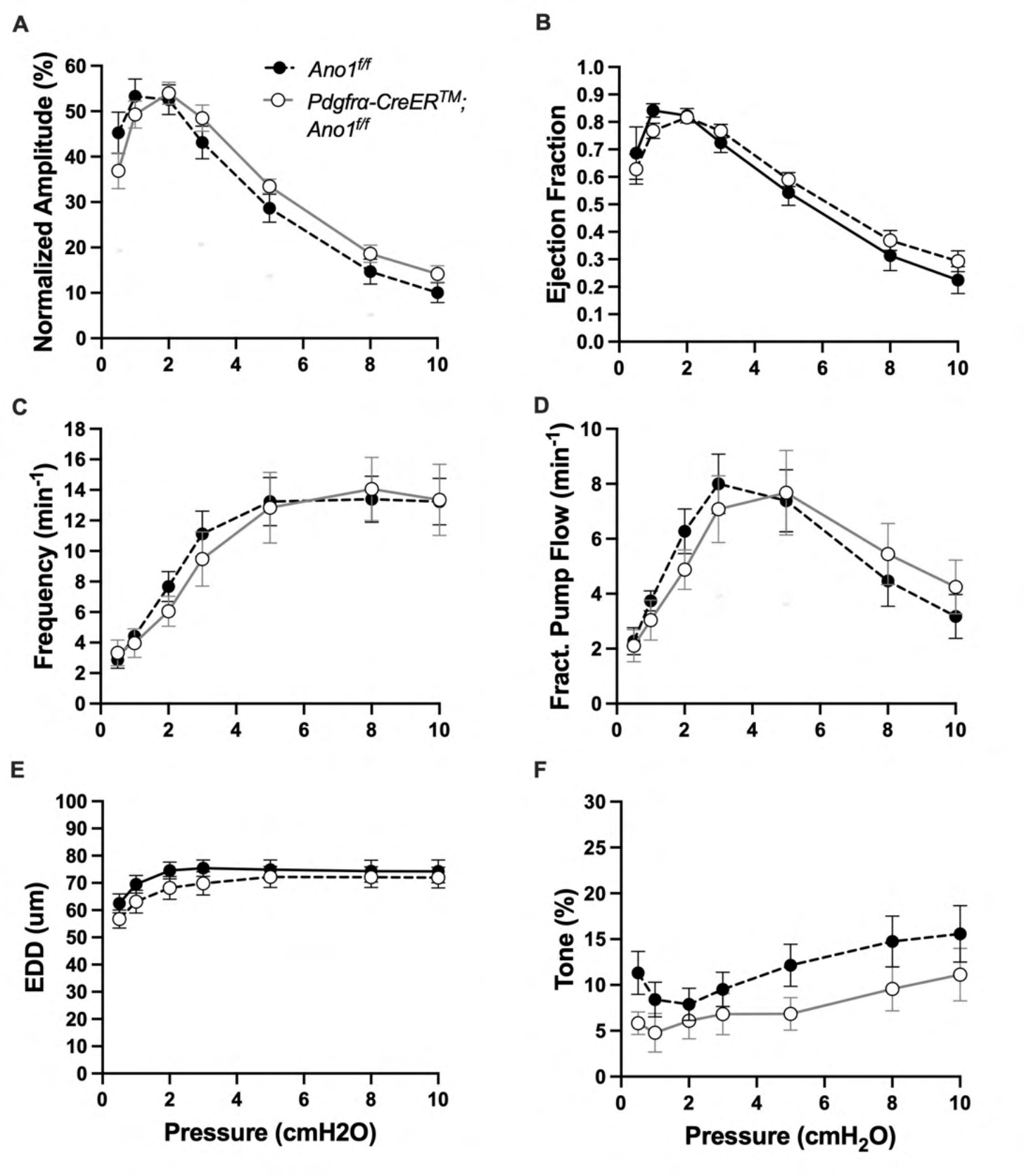
A
Ano1f/f
Pdgfrα-CreERTM; Ano1f/f
Normalized Amplitude (%)
B
Ejection Fraction
C
Frequency (min-1)
D
Fract. Pump Flow (min-1)
E
EDD (um)
Pressure (cmH2O)
F
Tone (%)
Pressure (cmH2O)

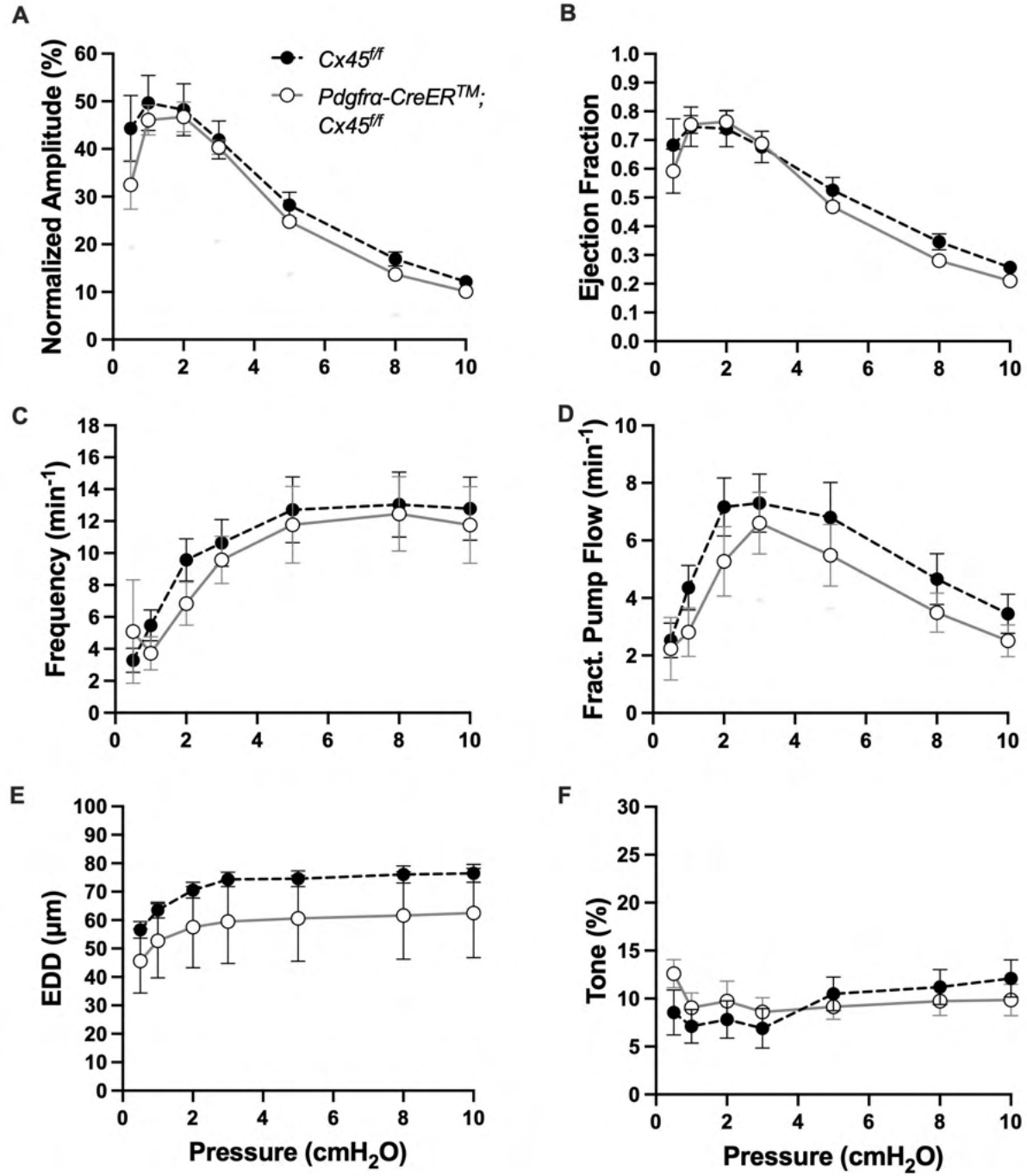
A
Normalized Amplitude (%)
Cx45f/f
Pdgfrα-CreERTM; Cx45f/f
B
Ejection Fraction
C
Frequency (min-1)
D
Fract. Pump Flow (min-1)
E
EDD (μm)
Pressure (cmH2O)
F
Tone (%)
Pressure (cmH2O)

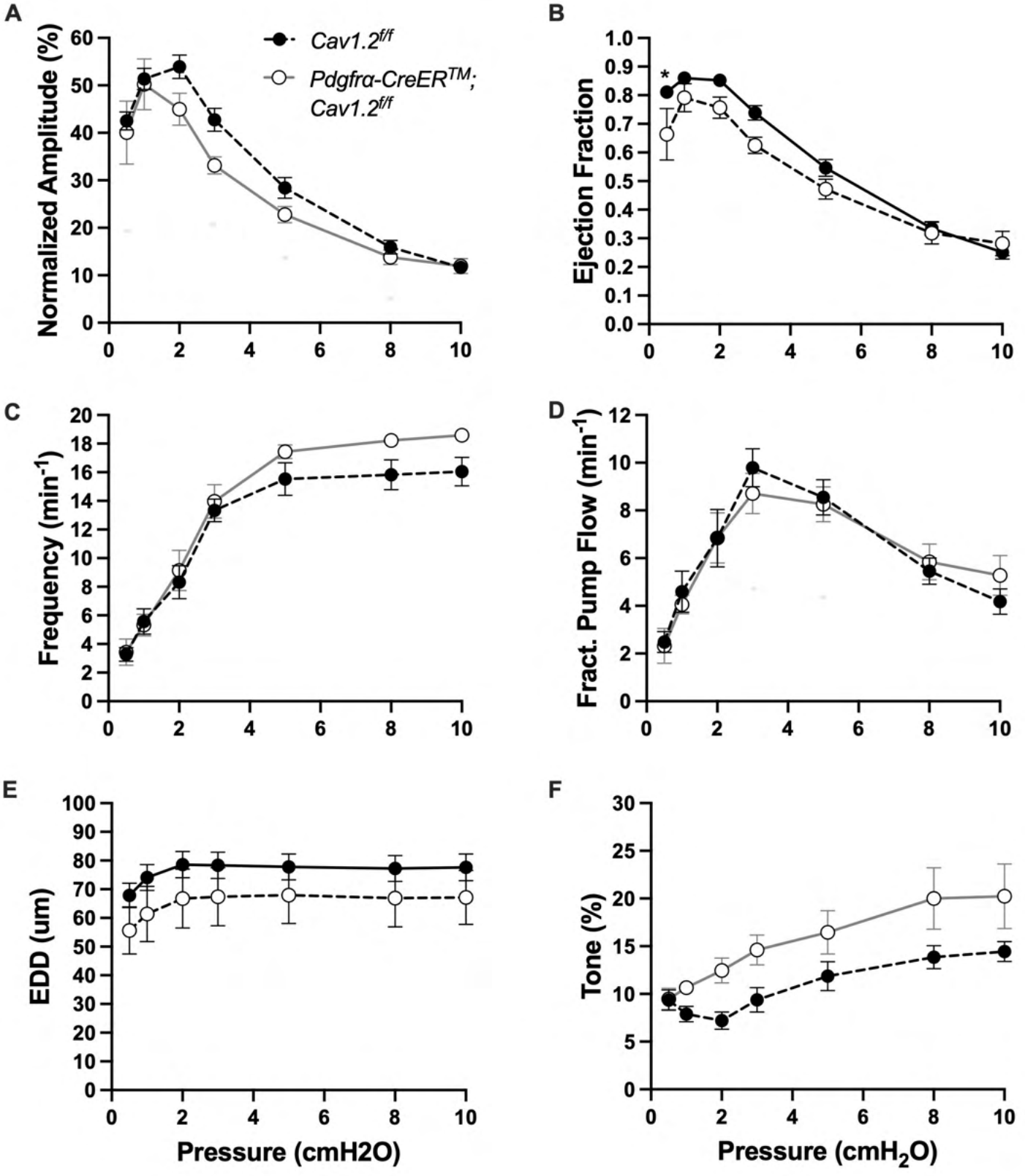
A
Normalized Amplitude (%)
Cav1.2f/f
Pdgfrα-CreERTM; Cav1.2f/f
B
Ejection Fraction
*
C
Frequency (min-1)
D
Fract. Pump Flow (min-1)
E
EDD (um)
Pressure (cmH2O)
F
Tone (%)
Pressure (cmH2O)

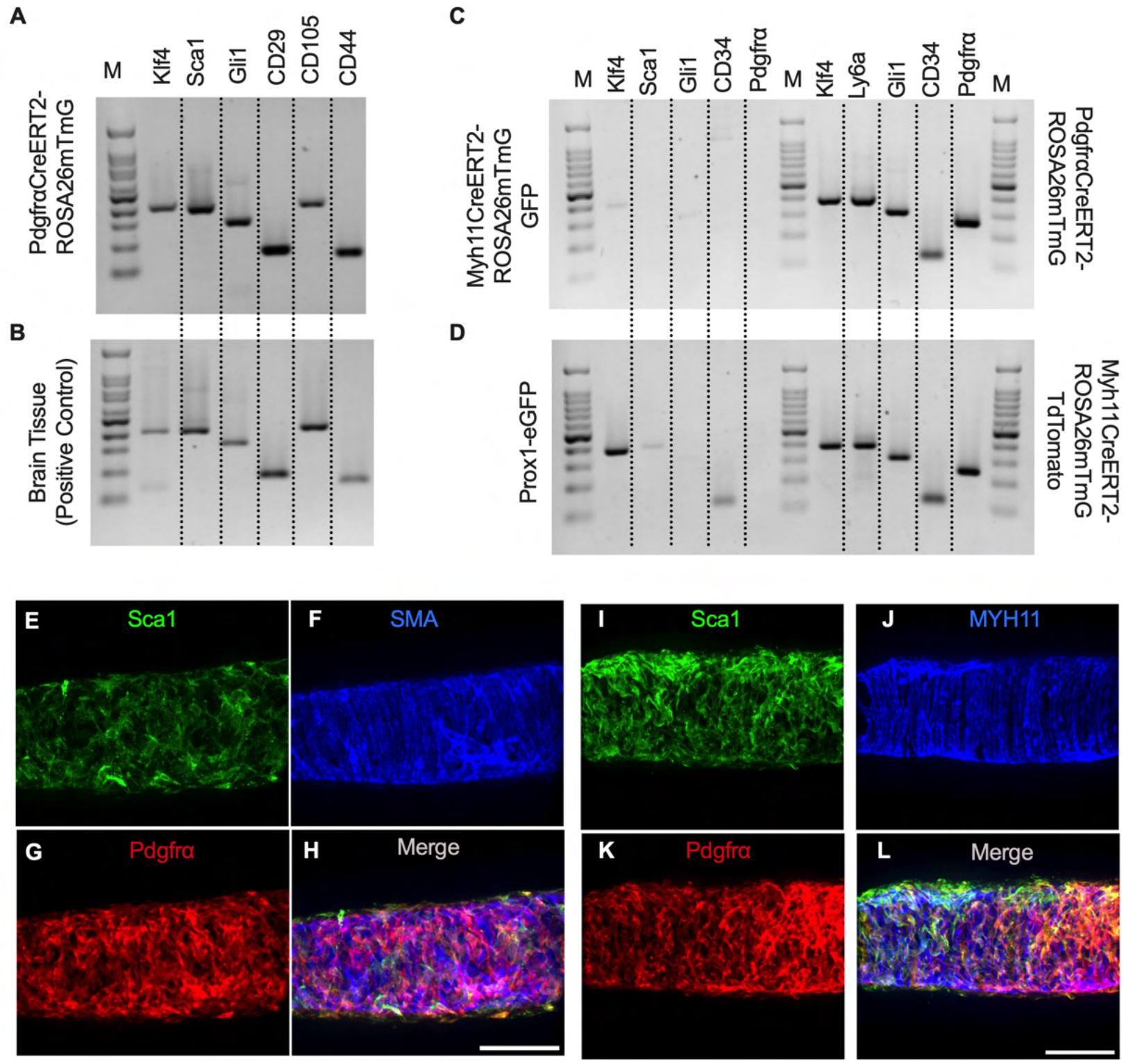
A
M
Klf4
Sca1
Gli1
CD29
CD105
CD44
PdgfrαCreERT2-ROSA26mTmG
B
Brain Tissue (Positive Control)
C
M
Klf4
Sca1
Gli1
CD34
Pdgfrα
M
Klf4
Ly6a
Gli1
CD34
Pdgfrα
M
Myh11CreERT2-ROSA26mTmG GFP
PdgfrαCreERT2-ROSA26mTmG
D
Prox1-eGFP
Myh11CreERT2-ROSA26mTmG TdTomato
E
Sca1
F
SMA
G
Pdgfrα
H
Merge
I
Sca1
J
MYH11
K
Pdgfrα
L
Merge

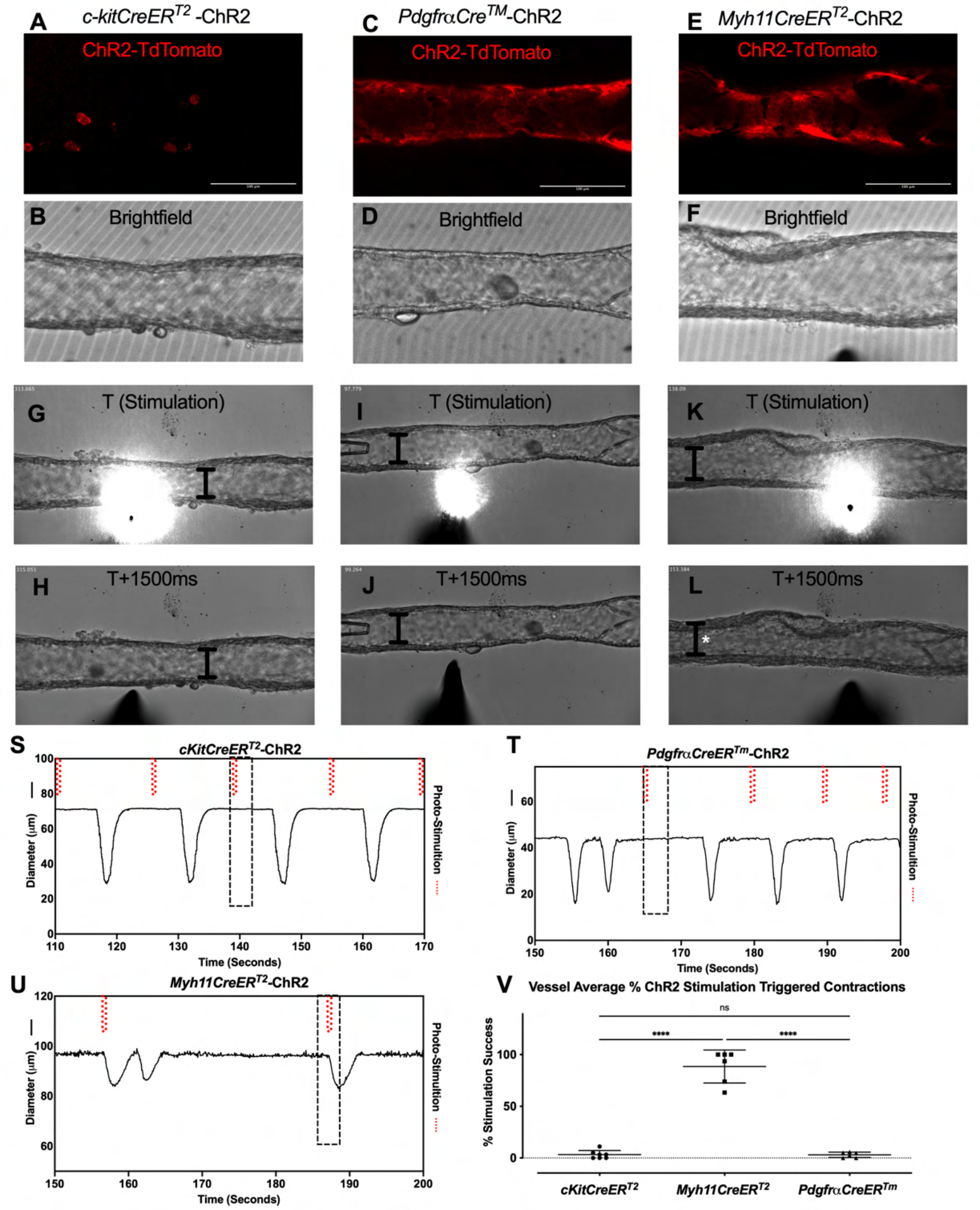
A
c-kitCreER^{T2} -ChR2
ChR2-TdTomato
C
PdgfrαCre^{TM}-ChR2
ChR2-TdTomato
E
Myh11CreER^{T2}-ChR2
ChR2-TdTomato
B
Brightfield
D
Brightfield
F
Brightfield
G
T (Stimulation)
I
T (Stimulation)
K
T (Stimulation)
H
T+1500ms
J
T+1500ms
L
T+1500ms
S
cKitCreER^{T2}-ChR2
Diameter (μm)
Time (Seconds)
Photo-Stimultion
T
PdgfrαCreER^{Tm}-ChR2
Diameter (μm)
Time (Seconds)
Photo-Stimultion
U
Myh11CreER^{T2}-ChR2
Diameter (μm)
Time (Seconds)
Photo-Stimultion
V
Vessel Average % ChR2 Stimulation Triggered Contractions
ns
****
****
% Stimulation Success
cKitCreER^{T2}
Myh11CreER^{T2}
PdgfrαCreER^{Tm}

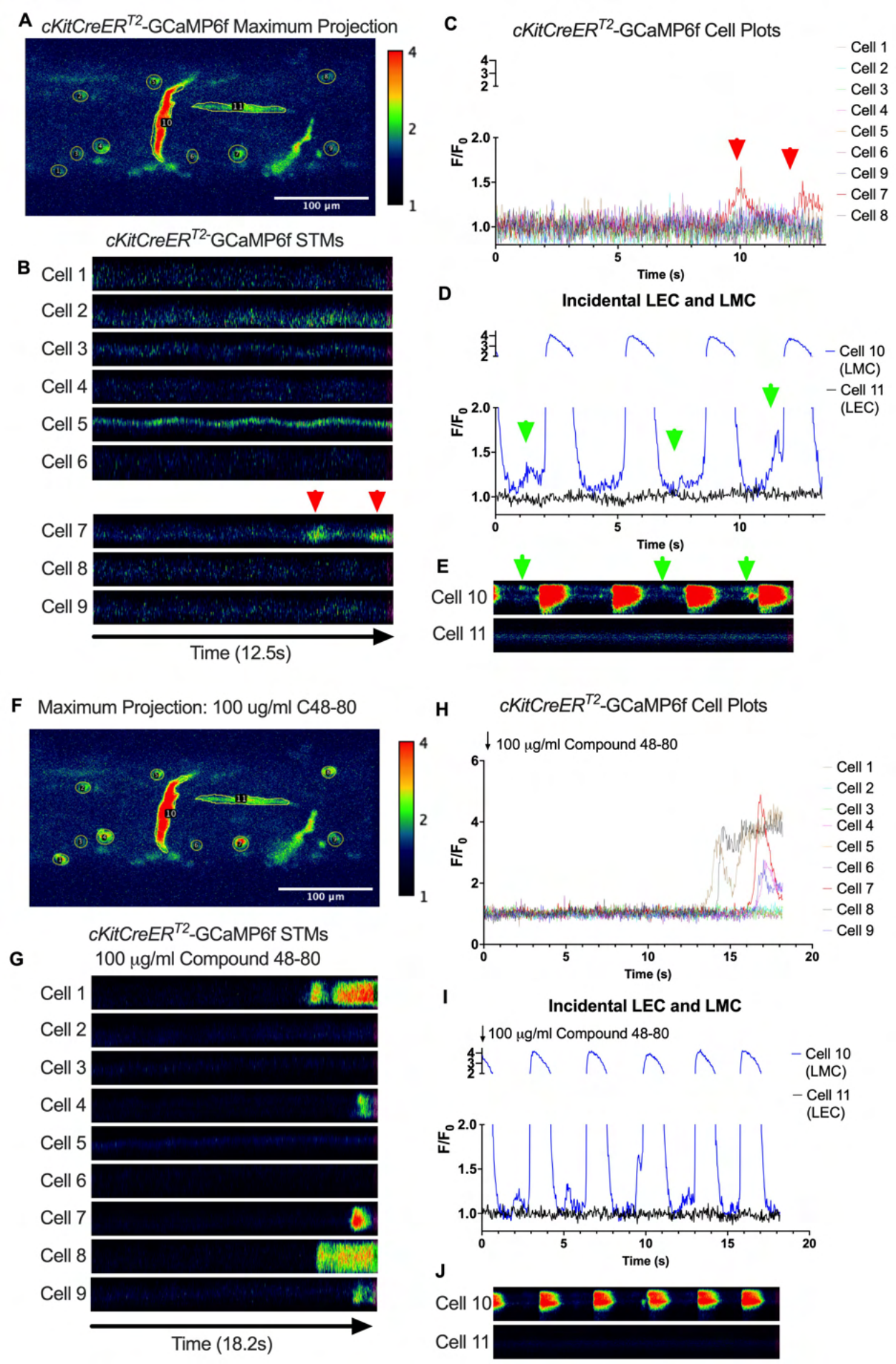
A
cKitCreER^{T2}-GCaMP6f Maximum Projection
100 µm
B
cKitCreER^{T2}-GCaMP6f STMs
Cell 1
Cell 2
Cell 3
Cell 4
Cell 5
Cell 6
Cell 7
Cell 8
Cell 9
Time (12.5s)
C
cKitCreER^{T2}-GCaMP6f Cell Plots
F/F$_0$
Time (s)
D
Incidental LEC and LMC
Cell 10 (LMC)
Cell 11 (LEC)
E
Cell 10
Cell 11
F
Maximum Projection: 100 ug/ml C48-80
100 µm
G
cKitCreER^{T2}-GCaMP6f STMs
100 µg/ml Compound 48-80
Time (18.2s)
H
cKitCreER^{T2}-GCaMP6f Cell Plots
100 µg/ml Compound 48-80
I
Incidental LEC and LMC
J

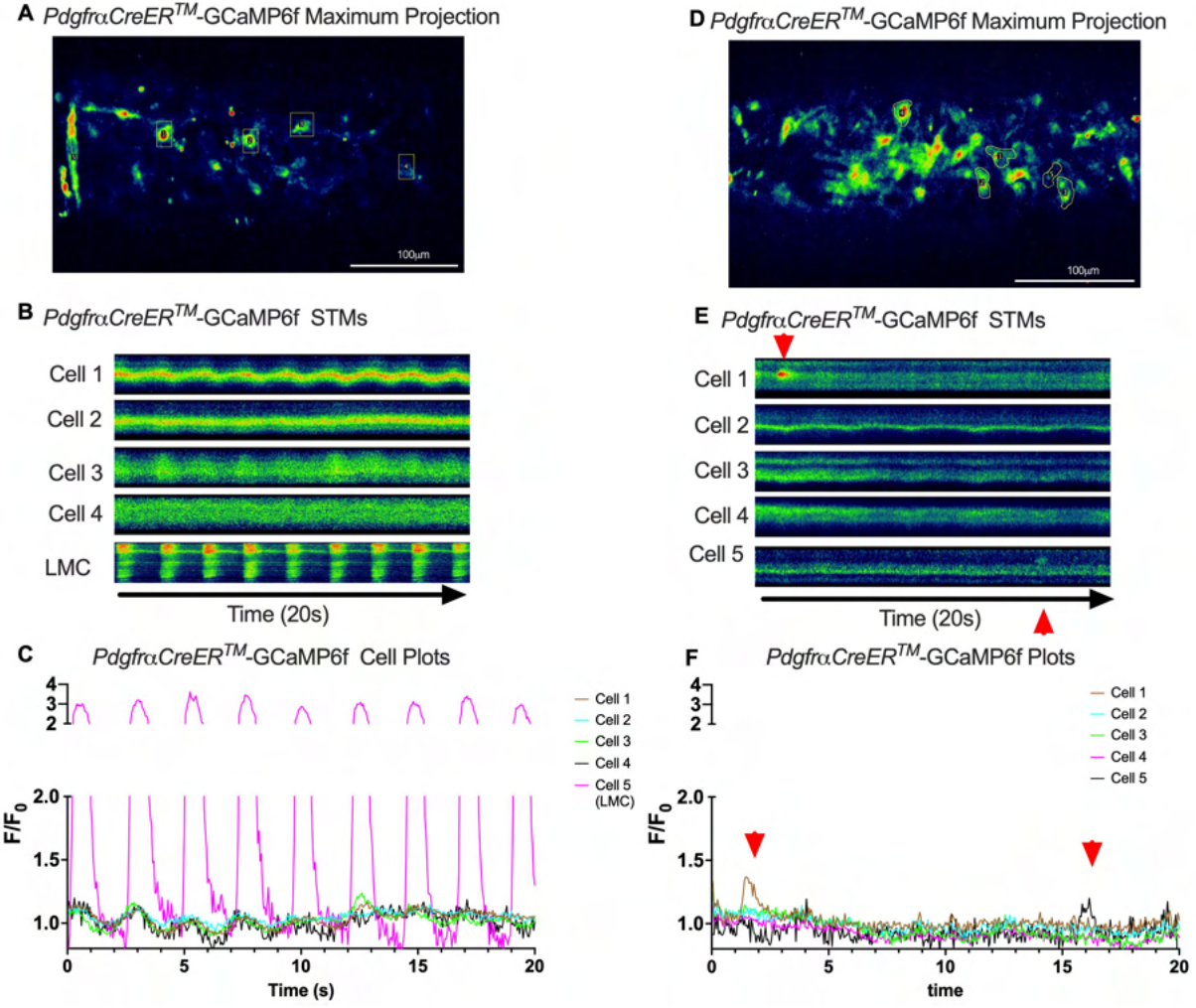
A PdgfrαCreER^{TM}-GCaMP6f Maximum Projection
100μm
B PdgfrαCreER^{TM}-GCaMP6f STMs
Cell 1
Cell 2
Cell 3
Cell 4
LMC
Time (20s)
C PdgfrαCreER^{TM}-GCaMP6f Cell Plots
Cell 1
Cell 2
Cell 3
Cell 4
Cell 5 (LMC)
F/F0
Time (s)
D PdgfrαCreER^{TM}-GCaMP6f Maximum Projection
100μm
E PdgfrαCreER^{TM}-GCaMP6f STMs
Cell 1
Cell 2
Cell 3
Cell 4
Cell 5
Time (20s)
F PdgfrαCreER^{TM}-GCaMP6f Plots
Cell 1
Cell 2
Cell 3
Cell 4
Cell 5
F/F0
time

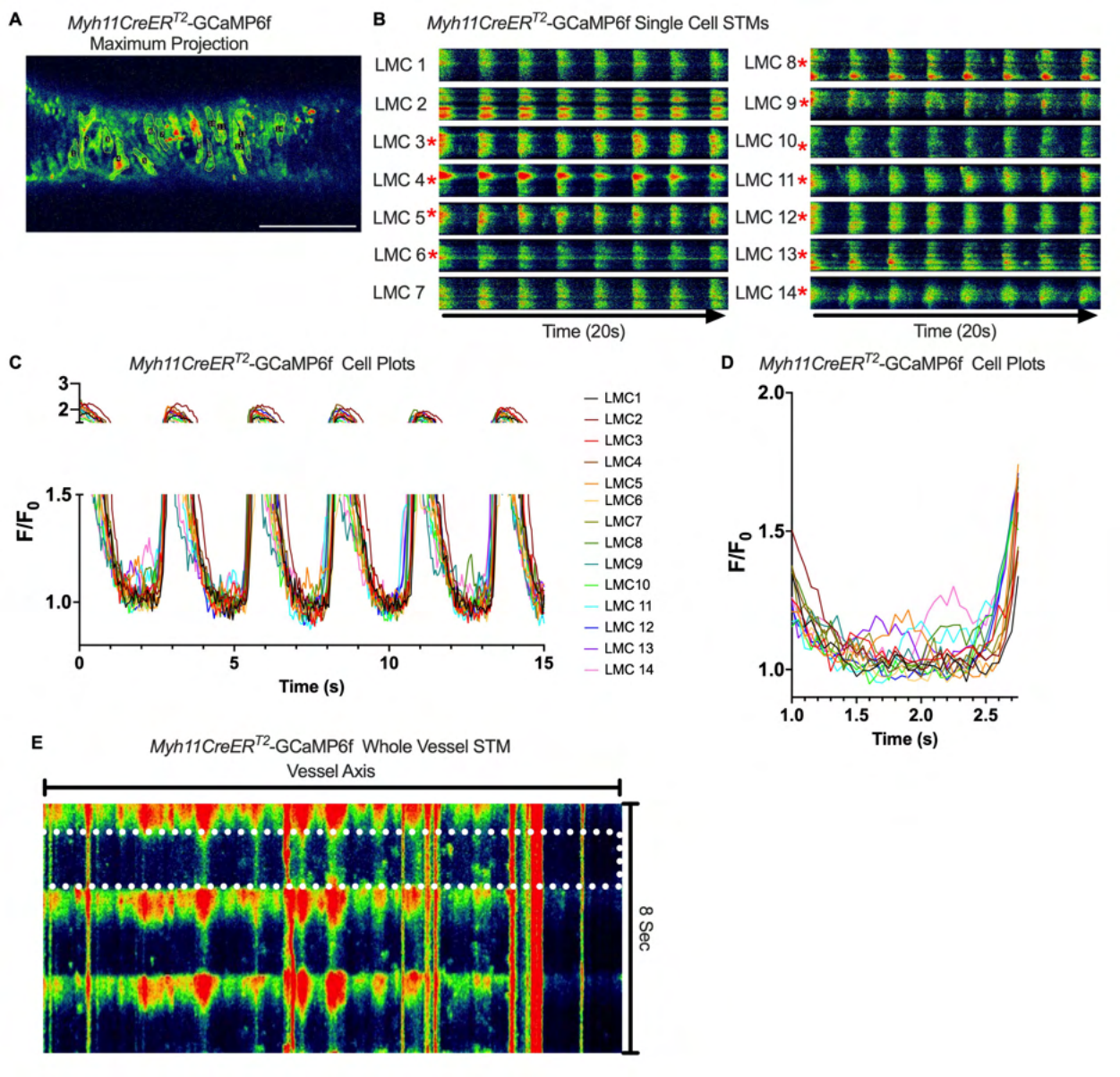
A
Myh11CreERT2-GCaMP6f
Maximum Projection
B
Myh11CreERT2-GCaMP6f Single Cell STMs
LMC 1
LMC 2
LMC 3*
LMC 4*
LMC 5*
LMC 6*
LMC 7
LMC 8*
LMC 9*
LMC 10*
LMC 11*
LMC 12*
LMC 13*
LMC 14*
Time (20s)
Time (20s)
C
Myh11CreERT2-GCaMP6f Cell Plots
F/F0
Time (s)
LMC1
LMC2
LMC3
LMC4
LMC5
LMC6
LMC7
LMC8
LMC9
LMC10
LMC 11
LMC 12
LMC 13
LMC 14
D
Myh11CreERT2-GCaMP6f Cell Plots
F/F0
Time (s)
E
Myh11CreERT2-GCaMP6f Whole Vessel STM
Vessel Axis
8 Sec

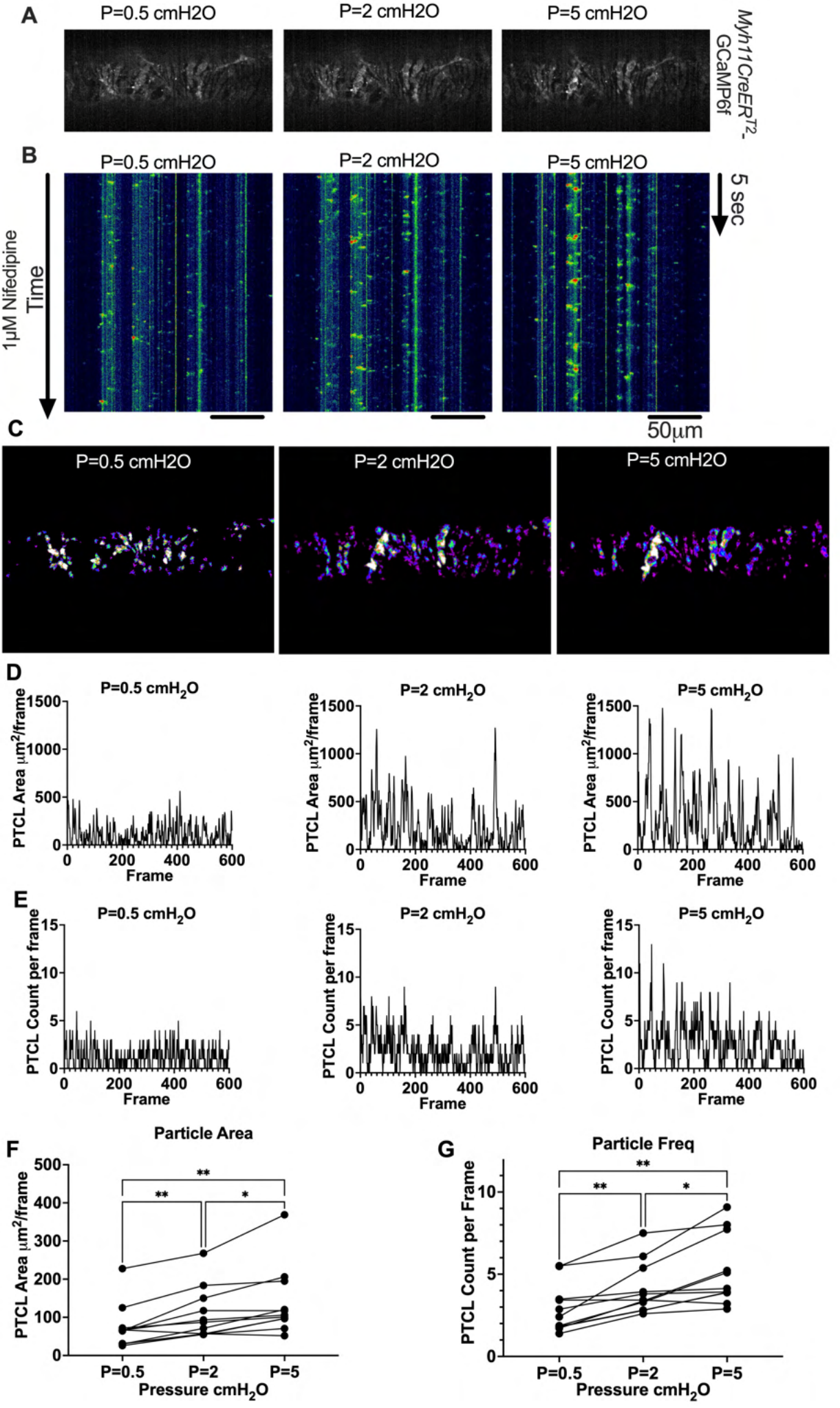
A
P=0.5 cmH2O
P=2 cmH2O
P=5 cmH2O
Myh11CreERT2-GCaMP6f
B
P=0.5 cmH2O
P=2 cmH2O
P=5 cmH2O
5 sec
1μM Nifedipine
Time
50μm
C
P=0.5 cmH2O
P=2 cmH2O
P=5 cmH2O
D
P=0.5 cmH2O
P=2 cmH2O
P=5 cmH2O
PTCL Area μm2/frame
Frame
E
P=0.5 cmH2O
P=2 cmH2O
P=5 cmH2O
PTCL Count per frame
Frame
F
Particle Area
PTCL Area μm2/frame
Pressure cmH2O
P=0.5
P=2
P=5
G
Particle Freq
PTCL Count per Frame
Pressure cmH2O
P=0.5
P=2
P=5